Università degli Studi di Firenze
Scuola di Ingegneria
DIEF - Department of Industrial Engineering of Florence

PhD School: *Energetica e Tecnologie Industriali ed Ambientali Innovative*
Scientific Area: ING-IND/08 - *Macchine a Fluido*

LES MODELING OF HYDROGEN COMBUSTION IN GAS TURBINES: FROM IGNITION TO FLAME STABILIZATION

PhD Candidate: Ing. Matteo Amerighi

Tutor: Prof. Ing. Antonio Andreini

Co-Tutor: Prof. Ing. Bruno Facchini

PhD School Coordinator: Prof. Ing. Giovanni Ferrara

XXXVI PhD School Cycle - 2020-2023

Per la mia famiglia,
Daniele e Roberta,
Alessio, Sara e Bianca,
Aldo ed Alda,
Mario ed Anna,
E soprattutto a Caterina.

Si fa con calma...

Amsterdam, 17 Giugno 2022
Alberto, Matteo, Sofia

Acknowledgements

Eccoci qua, alla fine della scrittura di questa tesi, nella parte più tranquilla e spensierata in cui poter ringraziare tutte le persone che mi hanno accompagnato nel corso di quest'avventura.

Un sincero ringraziamento va al Prof. Bruno Facchini che, fin dalla lontana laurea triennale, mi ha seguito nel corso dei miei studi facendomi scoprire il mondo delle turbine a gas per poi accogliermi nell'HTC-Group.

Il ringraziamento più doveroso va al Prof. Antonio Andreini che mi ha sempre dato fiducia e supportato nelle attività di ricerca. Dal temuto professore di combustione, nel corso di questi tre anni ho avuto l'opportunità di scoprire una persona con un'infinita passione e conoscenza per il mondo dell'ingegneria, informatica, elettronica, pesca e chi più ne ha più ne metta, con il quale ho condiviso eventi e missioni indimenticabili, primo fra tutti la "birra a metà" a Rotterdam.

Successivamente, un ringraziamento va al mio caro supervisore della tesi magistrale, Lorenzo Palanti (il Palo). I tuoi insegnamenti e la tua pazienza con "In Fig.3 is shown the ..." sono stati di fondamentale importanza per la mia crescita accademica e non solo. Unica pecca, ahimè, è stata la poca determinazione che hai messo nel dissuadermi da fare il dottorato...
P.S. Ti aspetto al prossimo giro in bici, preparati che ti farò ripagare tutte le camicie sudate in questi tre anni.

A questo punto c'è da ringranziare i compagni di ufficio storici, Langò ed Albertone (il King). Grazie a voi ho imparato: (i) i luoghi più improbabili dove nascondere caramelle Sperlari alla menta, (ii) l'importanza di

un clown in ufficio, (iii) Santa Marta chiude oltre le 19.30.

Cumpaaaa, come potrei non ringraziarti. Nata così, un po' per caso, si è creata questa amicizia fatta di solide (ma anche solite) lamentele e sproloqui post lavoro... ma come direbbe un saggio: Why not?

Un ringraziamento speciale va alla mia ex-tesista nonché attuale collega Giada, senza la quale gli ultimi mesi e la scrittura dei vari articoli non sarebbero stati gli stessi. Il tuo aiuto è stato fondamentale, in tutto. Purtroppo, anche io non sono riusciuto a dissuaderti dal fare il dottorato, quindi, un grosso in bocca al lupo per il futuro, cara amica!

Infine, un sentito grazie va a tutti i ragazzi e le ragazze dell'HTC-Group. Grazie a voi, questi tre anni densi di rinfreschini, apertivi, scherzi, missioni e momenti di pazzia sono letteralmente volati. Grazie davvero!

Abstract

Hydrogen combustion technologies are nowadays studied and developed by many companies and universities since their employment as carbon-free systems is considered a valid alternative to reach net-zero CO_2 emission by 2050. However, despite its advantages, the use of hydrogen presents numerous technical challenges that must be considered and solved, especially if it is used for aeronautical purposes.

First, hydrogen does not exist in nature, and its large-scale production is a critical issue, as current generation methods involve the emission of CO_2, which could nullify its benefits. Similarly, storage both on board aircraft and at airports is a problem given the hazardous nature of hydrogen. Finally, hydrogen has peculiar characteristics from a combustion point of view compared to the usual liquid fuels currently used.

Focusing on the latter, an indispensable step that every aircraft combustor performs several times a day is the ignition phase. In fact, before entering service, each combustor must pass rigorous certification of the ignition phase, both on the ground and at high altitude. Therefore, the design of a new combustor requires a thorough and dedicated study due to the different characteristics of hydrogen. In this sense, modern high-fidelity Computational Fluid Dynamics (CFD) simulations are a key tool for understanding the physical phenomena and dynamics occurring inside a combustor, where experiments are very often limited due to operational problems.

The present work aims to investigate the current standard models used in industry to study turbulent combustion with particular interest

in the ignition phase up to the flame stabilization, simulating different conditions under which it can occur and analyzing the dynamics observed inside the injector that govern its success or failure.

In the first part of the work, after introducing the models used in the course of this thesis, the impact of the diffusive transport model used is analyzed through laminar Direct Numerical Simulations (DNS), highlighting its effect in the first instants after kernel formation. This analysis, together with other preliminary studies carried out using the Cantera tool, allowed to identify the main objectives that need to be studied and deepened during the investigation of the two test cases examined.

The numerical analyses carried out on the test rig at the Technische Universität Berlin (TUB) aim to test different approaches for modeling the turbulence-chemistry interaction on a technically premixed hydrogen flame. After an initial validation of the cold velocity field by means of a mesh sensitivity analysis, the impact on the prediction of the mixing field is assessed against the assumptions underlying the models used. Although small differences appear in areas where combustion does not take place, the correct flame prediction of the Thickened Flame Model (TFM) approach, due to the inclusion of local effects on the flame front, permits the selection of the most accurate model among those tested for the study of lean hydrogen flames.

Following the analysis of the first burner, the investigation of the ignition transient of an academic test rig experimentally tested at the Norwegian University of Science and Technology (NTNU) is presented in which detailed measurements throughout the full process for different operating conditions are available. In the first part of the work, the simulation of a case that provides a successful ignition scenario is presented. It is demonstrated that the TFM coupled with an Energy Deposition (ED) strategy allows an accurate prediction of the most significant phases and mechanisms involved in the ignition dynamics, validating the employed numerical strategy. Subsequently, to mimic the effect of the back pressure at the outlet (e.g. a gas turbine nozzle), a perforated plate is introduced

at the combustion chamber exit to slightly increase the blockage ratio. Despite the negligible additional back pressure, the dynamics of the system is drastically altered, promoting the flashback occurrence. The driving mechanisms that trigger the flashback and the flame-holding process inside the injector are identified and explained.

Contents

Nomenclature

Acronyms

$AHEAD$	Advanced Hybrid Engines for Aircraft Development
AJ	Annular Jet
BLF	Boundary Layer Flashback
CFD	Computational Fluid Dynamics
CHT	Conjugate Heat Transfer
DNS	Direct Numerical Simulation
ED	Energy Deposition
$FFLECS$	novel Fuel-Flexible ultra-Low Emissions Combustion systems for Sustainable aviation
FGM	Flamelet Generated Manifold
$HESTIA$	HydrogEn combuSTion In Aero engines
HRR	Heat Release Rate
$HYDEA$	HYdrogen DEmonstrator for Aviation
HW	Hot Wire
IDT	Ignition Delay Time
IRZ	Inner Recirculation Zone
LES	Large Eddy Simulation
LFS	Laminar Flame Speed
LHV	Lower Heating Value
LOS	Line-Of-Sight

MIE	Minimum Ignition Energy
NSE	Navier-Stokes Equations
$NTNU$	Norwegian University of Science and Technology
ORZ	Outer Recirculation Zone
PDF	Probability Density Function
$PLIF$	Planar Laser-Induced Fluorescence
PM	Particulate Matter
PIV	Particle Image Velocimetry
PV	Progress Variable
PVC	Processing Vortex Core
$RANS$	Reynolds Averaged Navier Stokes
RMS	Root Mean Square
RQL	Rich-Quench-Lean
SAF	Sustainable Aviation Fuel
SGS	Sub-Grid Scale
SL	Shear Layer
TFI	Turbulence Facilitation Ignition
TI	Takeno Index
TFM	Thickened Flame Model
TRL	Technology Readiness Level
TUB	Technische Universität Berlin
$URANS$	Unsteady Reynolds Averaged Navier Stokes

Greeks

χ	Flow split parameter	$[-]$
δ	Thickness	$[m]$
Δ	Grid size	$[m]$
Δ_s	Characteristic spark size	$[m]$
Δ_t	Characteristic spark size	$[s]$
Γ	Gamma table	$[-]$

λ	Thermal conductivity	$[W.m^{-1}.K^{-1}]$
μ	Dynamic viscosity	$[kg.m^{-1}.s^{-1}]$
ρ	Density	$[kg.m^{-3}]$
ϕ	Equivalence Ratio	$[-]$
ψ	Heat loss coefficient	$[-]$
τ	Viscous Stress Tensor	$[Pa]$
$\dot{\omega}$	Production rate	$[kg.m^{-3}.s^{-1}]$

Letters

A	Area	$[m^2]$
c	Progress Variable	$[-]$
c_p	Spec. heat capacity at const. P	$[J.kg^{-1}.K^{-1}]$
Da	Damköhler Number	$[-]$
D_{ij}	Mass diffusion coefficient of species i into species j	$[m^2.s^{-1}]$
$D_{i,m}$	Mass diffusion coefficient of species i into the mixture	$[m^2.s^{-1}]$
$D_{T,i}$	Thermal diffusion coefficient of species i	$[m^2.s^{-1}]$
D_{lam}	Laminar diffusivity	$[m^2.s^{-1}]$
D_{th}	Thermal diffusivity	$[m^2.s^{-1}]$
D_{turb}	Turbulent diffusivity	$[m^2.s^{-1}]$
d	Quenching distance	$[m]$
E	Efficiency function	$[-]$
E_i	Energy deposited	$[J]$
$\mathcal{F}$	Thickening factor	$[-]$
K	Stretch rate	$[s^{-1}]$
k	Strain rate	$[s^{-1}]$
Ka	Karlovitz number	$[-]$
Le	Lewis number	$[-]$
Le_F	Lewis number of the fuel	$[-]$
l_t	Integral length scale	$[m]$
Pr	Prandtl number	$[-]$
P	Pressure	$[Pa]$

R	Curvature radius	$[m]$
Re	Reynolds number	$[-]$
S_c	Schmidt number	$[-]$
s_c	Consumption speed	$[m.s^{-1}]$
s_d	Displacement speed	$[m.s^{-1}]$
s_l	Laminar flame speed	$[m.s^{-1}]$
T	Temperature	$[K]$
t	Time	$[s]$
U	Velocity	$[m.s^{-1}]$
$\dot{V}$	Volumetric mass flow	$[m^3.s^{-1}]$
V_i	Diffusion velocity	$[m.s^{-1}]$
Y	Species mass fraction	$[-]$
Y_c	Un-normalized progress variable	$[-]$
Z	Mixture Fraction	$[-]$

Subscripts

0	Unstretched
ad	Adiabatic
b	Burnt
eq	Equilibrium
u	Unburnt

Publications

National conferences

- Amerighi M., High-fidelity investigation of FGM and TFM approach on a lean hydrogen flame. 45th Meeting of the Italian Section of The Combustion Institute, Florence, 2023.

International conferences

- Langone, L., Amerighi, M., Andreini, A. (2022, June). Numerical modeling of lean spray lifted flames in inclined multi-burner arrangements. In Turbo Expo: Power for Land, Sea, and Air. American Society of Mechanical Engineers.

- Langone, L., Amerighi, M., Andreini, A. (2022, June). Assessment of Thickened Flame model coupled with Flamelet Generated Manifold on a low-swirl partially premixed gaseous lifted flame. In Turbo Expo: Power for Land, Sea, and Air. American Society of Mechanical Engineers.

- Amerighi, M., Nassini, P. C., Andreini, A., Orsino, S., Verma, I., Yadav, R., Patil, S.. (2023 June). Assessment of flamelet generated manifold approach with inclusion of stretch effects of pure hydrogen flames. In Turbo Expo: Power for Land, Sea, and Air. American Society of Mechanical Engineers.

International journals

- Andreini, A., Amerighi, M., Palanti, L., & Facchini, B. (2022). Large Eddy Simulation Based Computational Fluid Dynamics Investigation of the Ignition Process in Lean Spray Burner. Journal of Engineering for Gas Turbines and Power, 144(6), 061016.

- Langone, L., Amerighi, M., Andreini, A.. Large Eddy Simulations of a Low-Swirl Gaseous Partially Premixed Lifted Flame in Presence of Wall Heat Losses. Energies, 2022, 15.3: 788.

- Amerighi, M., Andreini, A., Reichel, T., Tanneberger, T., Paschereit, C.O.. LES investigation of a swirl stabilized technically premixed hydrogen flame with FGM and TFM models, Applied Thermal Engineering, Volume 247, 2024.

- Amerighi, M., Andreini, A., Orsino, S., Verma, I., Yadav, R., Reichel, T.,Tanneberger, T., Paschereit, C. O.. (2024). Predicting NOx emissions of a lean hydrogen flame using high and low order cfd models. Journal of Engineering for Gas Turbines and Power.

- Amerighi, M., Senatori, G., Yahou, T., Schuller, T., Dawson, J. R., Andreini, A. (2024). Complete dynamics from ignition to stabilization of a lean hydrogen flame with thickened flame model. Journal of Engineering for Gas Turbines and Power.

Introduction

The current global scenario reflects a growing awareness and concern about climate change, a phenomenon linked to, among other things, power generation, public transportation and industrial sector. In all of them, as a consequence of the hydrocarbon combustion process, both the unavoidable products (water vapor H_2O and carbon dioxide CO_2) and the secondary combustion products (oxides of nitrogen NO_x, unburnt hydrocarbons UHC, carbon monoxide CO and particulate matter PM) are obtained. A large contribution to climate change comes from CO_2 emissions, which is one of the well-known causes of the global warming observed in recent years. The critical need to reduce it has been highlighted by its implications on weather and air quality. All of these factors led to the signing of the Paris Agreement in 2015 which aims to limit the global average temperature increase to below 2 °C compared to pre-industrial levels, with efforts to limit the increase to 1.5 °C. Notably, although during the COVID-19 pandemic marked enhancements in air quality were observed due to the reduction of transportation [1], the current growth rate has returned to pre-pandemic values with a monotonous upward trend [2].

As far as concern the aviation sector, it is shown that it contributed approximately 4% to observed human-induced global warming with a projection to cause a total of about 0.1 °C of warming by 2050 (Fig. 1) [3].

In this context, the Flightpath 2050 initiative, which seeks to achieve a 75% and 90% reduction in CO_2 and NO_x emissions per passenger kilometer in civil aviation [4], underscores the imperative to define different

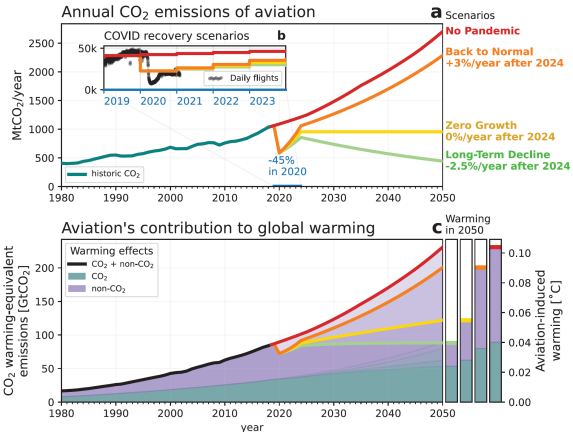

Figure 1: Impact of aviation on global warming to 2050. Four different scenarios are reported [3].

solutions to attain this ambitious objective. Prominent among these solutions are hydrogen-based technologies [5, 6], Sustainable Aviation Fuels (SAF) [7], and hybrid electric-thermal propulsion systems [8], all of which are considered viable alternatives to address the environmental impact associated with aviation emissions due to its carbon-free nature. These technological advancements align with the broader goal of mitigating the ecological footprint of civil aviation and are integral to the pursuit of sustainable and environmentally responsible air transportation systems.

Focusing on the hydrogen solution, a complete transition at a large scale requires major improvements in production technologies, storage and combustion control. In fact, from a combustion point of view, hydrogen differs from conventional fuels (Jet-A) in several aspects. First, hydrogen is characterized by a three times higher Lower Heating Value (LHV) which allows drastic reductions in the amount needed to obtain a certain output power. At the same time, hydrogen has a higher adiabatic flame temperature which needs special attention to avoid an overproduction of NO_x emission. Although the state-of-art architecture is represented

by the Rich-Quench-Lean (RQL) [9] concept, the high flammability limits of hydrogen allow for the exploration also lean burning conditions. Specifically, lean technically premixed configurations [10, 11] are of great interest because they allow direct control of the temperature in the primary zone aiming to limit the NO_x emissions [12]. Nevertheless, the use of hydrogen brings with it new design challenges, first and foremost the ignition phase, even though this may seem contradictory. In fact, in the current liquid kerosene aircraft engines, the critical issue lies in the atomization process that can cause an ignition failure, especially in high altitude conditions. However, with hydrogen, the problem is the high overpressure that is generated, potentially leading to flashbacks or flame stabilization in undesignated locations, as detailed in the next chapter.

Several European projects, focused on the investigation of the technical aspects of using hydrogen as aviation fuel with the objective of demonstrating its feasibility were recently started with different Technology Readiness Level (TRL).

The HYdrogen DEmonstrator for Aviation (HYDEA) project involves ten different countries and several partners with the common goal of developing a hydrogen propulsion system to secure an entry into service of a zero-CO_2 low-emission aircraft by 2035 [13]. This project is therefore characterized by a very high TRL.

The HydrogEn combuSTion In Aero engines (HESTIA) project, coordinated by Safran, involves six aero-engine manufacturers and 18 universities and research centers. The main objectives are to enhance the comprehension of hydrogen combustion through both experimental and numerical campaigns [14].

The novel Fuel-Flexible ultra-Low Emissions Combustion systems for Sustainable aviation (FFLECS) project, coordinated by the University of Florence, is a pioneering project aimed to explore the simultaneous use of H_2 and SAF on a burner which combines different designed concepts [15].

Aim of the work

The main purpose of this thesis work is to study the combustion dynamics, from kernel formation to complete flame stabilization, on burners operating with 100% hydrogen mixture through high-fidelity CFD simulations. Due to the peculiar characteristics of hydrogen, a preliminary investigation of the main turbulent combustion models used in industry is carried out to identify a suitable and reliable approach. Hence, the stable flame of the academic burner developed by TU Berlin is investigated by proposing an improvement to the standard FGM model. The research subsequently addresses the main topic of the work, highlighting and proposing CFD numerical methodologies capable of capturing both local and global effects on hydrogen ignition dynamics.

At the present day, to the best of the author's knowledge, the proposed work represents a pioneering numerical exploration of the entire ignition transient process of a premixed hydrogen flame, including both regular ignition and flashback conditions. The investigated aspects are of paramount importance in comprehending the driving mechanisms that govern and regulate the flame dynamics within the injector after the ignition, where experimental measurements are typically unaffordable, providing important design input.

Thesis outline

This thesis is divided into three sections. The first section frames the problem of hydrogen flame ignition and recalls the main numerical approaches used for modeling turbulent flames in the LES framework. The main characteristics of hydrogen, using both low-order (e.g. Cantera) and high-order tools such as DNS simulations are employed, highlighting their impact during the stabilization transient.

The second section applies various numerical methodologies to a representative test case developed by TUB.

The last section proposes a numerical methodology for studying the ignition transient of a hydrogen flame based on the results obtained in

the previous sections.

- **Chapter 1**: deals with the ignition transient for gas turbines. The three main phases into which the process can be divided are presented, highlighting their main aspects and the new challenges associated with the use of hydrogen.

- **Chapter 2**: summarises the governing equations and numerical models for turbulent combustion in LES framework used in this thesis work. The ignition model used to simulate the spark is also reported, emphasizing the assumptions and constraints involved. Afterward, the characteristics of hydrogen in terms of combustion speed, stretch effects and preferential diffusion that distinguish it from conventional fuels such as kerosene and methane are analyzed using low- and high-order approaches. These analyses aim to assess the impact of these effects on the early stages of ignition.

- **Chapter 3**: reports the analyses conducted on the atmospheric, swirl-stabilized, lean technically-premixed hydrogen-air flame combustor studied experimentally at TUB. Starting with an evaluation of the spatial resolution under non-reactive conditions, the various models presented in the previous chapter are tested under stable flame conditions. This is followed by an analysis of the mixing process occurring inside the mixing tube and then comparing the flame morphology with the available experimental data. Finally, the impact of the combustion model used and the effect of thermal boundary conditions on local flame characteristics are compared.

- **Chapter 4**: presents the study of the complete ignition process of a lean, perfectly premixed hydrogen-air flame stabilized on a bluff body. The study initially focused on the cold flow field due to the impact on ignition dynamics. The model selected from the analysis on the previous combustor is used first to simulate the ignition process under soft ignition conditions. Then, through the introduction of a perforated plate at the outlet, the effect of back

pressure at the chamber exhaust is recreated by promoting the initiation of a flashback.

In the last chapter, some conclusions about this research are drawn along with some recommendations for future works.

Chapter 1

From ignition to flame stabilization

This chapter presents the challenges of using hydrogen to achieve proper flame stabilization while avoiding the risk of flashback. The first part introduces the ignition process on gas turbine combustors from a phenomenological point of view, divided into various stages. For each stage, the main studies in the literature are reported from both numerical and experimental perspectives. In the final section of the chapter, the flashback problem and the various mechanisms by which it can occur are briefly introduced. Then, supporting studies that highlight the need for further numerical investigation to treat these phenomena following the ignition process are reported.

1.1 Ignition phenomenology

The term *ignition* refers to the initiation and the complete establishment of the combustion process [16] followed by either an external energy source or the spontaneous activation of the reactions. The first case is referred in the literature as *forced ignition* in which the initial conditions of the mixture in terms of a chemical point of view are frozen and only after the deposition of energy and/or radical species that raise the temperature

high enough a self-sustaining flame is generated [17]. The second case instead is referred as *autoignition* [18, 19, 20] of the mixture as a result of the initial high-temperature condition of one or both of the reactants (but usually the oxidizer) which allow for chemical reactions to proceed [21] without any external source of energy and/or radical. Particular attention must be paid to the difference between the two mechanisms mentioned in order to avoid misunderstanding since they provide the same results but are based on completely different physical processes. Throughout this work, since of interest in the test case under investigation, only the forced ignition case is presented in the subsequent analysis. Nevertheless, some works dealing with the autoignition of hydrogen mixtures in turbulent conditions through LES approaches are present in the literature as the one in [22].

The forced ignition must develop according to a specific timeline, which involves different time and spatial scales as well as physical processes [16, 17, 21, 23], that can be divided into three main phases (or four depending on the reference text):

- Kernel generation
- Flame growth and burner-scale establishment
- Light-round

in which the last one is present only for multi-injector systems. A failure of any of these steps provides an unsuccessful ignition event.

1.1.1 Kernel generation

Different devices can be used to ignite a mixture including laser [24] and spark plug [25]. Laser technology has innumerable advantages such as non-intrusiveness and the possibility to focus the laser in any position within the chamber, which justifies its wide use in an academic context for liquid fuels [26, 27] and hydrogen [28]. However, in practical applications optical access to the combustion chamber is not accessible, so the classic spark plug device is commonly used. Applications for

academic studies with this device are present for both methane [29] and hydrogen [30] gas mixtures. The purpose of these devices, as mentioned earlier, is to provide enough energy to raise the temperature of a designed and favorable region, with a dimension equal to the so-called *quenching distance* which is proportional to the size of the laminar flame thickness, above the adiabatic flame temperature to trigger the reactions and start the combustion [16, 21]. Therefore, the concept of the Minimum Ignition Energy (MIE) i.e. the minimum energy required to guarantee the kernel generation [21] is introduced. It is essential to underline that due to the stochastic nature of the turbulence and the discharge formation, ignition is a statistical process and as a consequence, the MIE is usually defined as the energy level that guarantees a 50% *ignition probability*. Particular attention must be paid to the difference between the terms ignition and ignition probability. Indeed, the latter represents the probability of having a successful ignition by describing the variability of the process as a result of its stochastic nature. Since it is evaluation is not the topic of this thesis, interested readers may refer to [17, 31] for further details.

It should also be considered that as a result of the deposition of energy by either spark plug or laser ignition, part of the energy provided by the device is not transmitted to fluid due to heat losses [23]. From a numerical point of view, the inclusion of such effects is of paramount importance and the numerical models must account for that. However, the greatest challenge in CFD simulations lies in modeling the plasma phase that is formed in the first instants as a result of the complex chemistry involved [32], reduced time and length scales [25]. Although some work can be found in the literature that simulates the entire process [33, 34], it has been shown that this first stage has a minor impact on the entire ignition process [35]. Therefore, models are developed to simulate mixture ignition by neglecting the first phase while maintaining low computation costs without losing accuracy. The idea behind these models is the addition of an explicit source term to the energy (or enthalpy) equation that is smoothed in both time and space and provides an amount of energy in a given time period at the predetermined location [36]. Numerous

studies can be found in the literature using these approaches coupled with primitive variable models. Falkenstein et al.[37] through DNS conducted at elevated pressure study the cycle-to-cycle variability in kernel formation on internal combustion engines while Pouech et al. [38] investigates the ignition of a premixed methane/air mixture over a backward-facing step in a high-speed flow configuration. Studies on the ignition of spray flames are also present, as reported in [23, 39]. Recently, Garzon et al. [40] applied the energy deposition approach coupled with an automatic mesh refinement strategy and the thickened flame model. However, the energy deposition modeling is also applied to hydrogen flames through tabulated chemistry models [41].

1.1.2 Flame growth and burner-scale establishment

Once the kernel is properly formed, as a result of the first phase, successful ignition up to proper flame stabilization is still not guaranteed due to the influence of several parameters. In fact, as mentioned earlier, the ignition process is a stochastic event whose level increases as the complexity of the test case under consideration increases in terms of fluid dynamic conditions in the kernel's surroundings. Mastorakos reports in [17] that complete ignition of the chamber occurs if the flame is moving in the right direction and if the entire flame is stable after ignition.

Due to the conditions under which this phase takes place in terms of characteristic times and length scales more accessible both numerically and experimentally than the previous one, many papers in the literature that investigate this aspect are available. Analyses are conducted for both premixed [29] and non-premixed conditions operating with gaseous [42] and liquid [43, 44] fuel including the experimental one conducted by Marrero et al. [27] in which all the various underlying mechanisms that lead to extinction or ignition by varying the position of the spark are identified.

Regarding flames operating with gaseous fuel (spray flames are not discussed further since are beyond the scope of this work, more details are available in [16, 23]), one of the main parameters that influences this

phase while also explaining the stochasticity of the process is the effect of turbulence [45]. In 2014, Wu et al. [46] introduced the concept of *turbulence-facilitation ignition* (TFI). They found that after kernel formation between the spark plug electrodes (in the first instants during the flame growth phase), turbulence causes kernel fragmentation into multiple wrinkled flame elements with both positive and negative curvatures. In the investigated case of a hydrogen-air flame with an equivalence ratio of 5.1 characterized by a Lewis number greater than 1, the stretch response promoted ignition in the case of negative curvature. This concept of TFI has been confirmed both experimentally [47, 48] and numerically [49] studies. Additionally, the numerical analysis in [49] that studied high Lewis number mixtures explained how ignition under turbulent conditions (rather than in a quiescent atmosphere) promoted kernel transport away from the 'cold' electrodes, reducing previously introduced heat loss and facilitating successful ignition. The authors later extended their analysis to hydrogen-air mixtures under lean conditions, characterized by a Lewis number less than 1 [50]. They found that TFI effects can exist even under these conditions for specific ranges of pressure, velocity, and electrode gaps by proposing a regime diagram. The effects of preferential diffusion and thus Lewis number on the development of a hydrogen kernel under engine conditions are also studied in [51] through DNS. This work, contrary to the previous one, investigates the role of thermodiffusion effects on the first instants after kernel formation under both laminar and turbulent conditions.

Finally, the last parameter that must be taken into account and that plays a major role during flame growth and propagation for hydrogen mixtures is the overpressure that is generated as a result of the thermal expansion of the burnt gases [30, 52]. The trend of overpressure for methane-air mixtures with hydrogen addition for different blend values is shown in Fig. 1.1. This behavior reduces the pressure drop across the injector with a consequent reduction of the flow rate through it. The phenomenon can lead to a local imbalance between the fresh mixture velocity and the flame speed [53], resulting in a flashback condition that,

depending on the burner geometry and mixture preparation strategy, can lead to flame stabilization in regions not designed for flame holding [54].

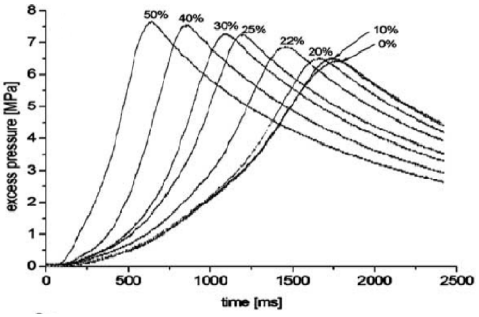

Figure 1.1: Effect of hydrogen enrichment on the overpressure generated during ignition for a CH_4-air mixture at 437 K, $3{\cdot}10^6$ Pa and ϕ=1.8 [55].

1.1.2.1 Flashback dynamics

This subsection reports from a phenomenological point of view the main mechanisms leading to the flashback condition. The analysis is not intended to be exhaustive but is aimed to provide the basic concepts about these mechanisms since they are partially covered in the course of this thesis. The reader is referred to [56, 57] for further study of this aspect.

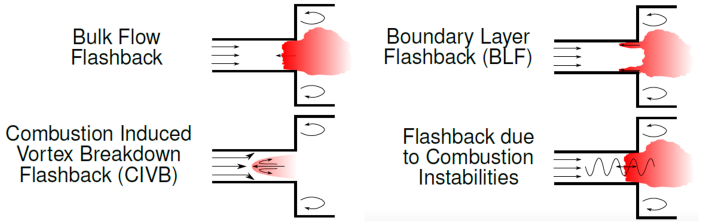

Figure 1.2: Schematic representation of different flashback mechanisms occurring in gas turbine combustors (adapted from [58]).

Fig. 1.2 shows a schematic of the four main flashback mechanisms, which are:

- Bulk Flow Flashback: The first mechanism is bulk flow flashback, which occurs if the turbulent flame speed is greater than the local flow velocity in the burner core. Therefore, the main factor influencing this mechanism is the aerodynamics of the burner and the resulting levels of turbulence in the anchor zone that determine the effective turbulent flame front reactivity. One method of avoiding the occurrence of this phenomenon, for extremely reactive fuels such as hydrogen, may be to take advantage of a purely axial jet of oxidizer, which due to its momentum prevents triggering. This strategy is used in the first test case analyzed in this thesis work by TUB [59].

- Boundary Layer Flashback (BLF): this flashback mechanism occurs in the low wall velocity zones inside the boundary layer where the flame front can find favorable conditions for its upstream propagation. In the same TUB test case [11] an injection of air is used in such a way as to locally lean the wall mixture and thus reset the wall reactivity to zero.

- Combustion Induced Vortex Breakdown Flashback (CIVB): the main method of stabilizing a flame in a combustor chamber is the formation of a recirculation zone through a swirler that allows radicals to be delivered to the flame front. However, although the aerodynamics of the swirler is properly designed under non-reactive conditions, chemical reactions can create a pressure imbalance in the vortex core that leads to flame propagation in the burner [56].

- Flashback due to Combustion Instabilities: combustion instabilities can also trigger two of the preceding mechanisms described, which are bulk flow flashback and BLF. The main instabilities are turbulence noise, coherent structures such as processing vortex cores (PVC) due to swirled flows, forced coherent flow structure and self-exciting instabilities.

1.1.2.2 Flashback studies on hydrogen enriched flames

The study of the initiation of flashback mechanisms for hydrogen-enriched flames is investigated in the literature both experimentally and numerically.

Duan et al. [60] studied experimentally the influence of the burner material and the tip temperature of jet flames with different geometrical configurations for atmospheric premixed hydrogen-air mixtures. In order to trigger the flashback, two protocols are used: (i) Constant adiabatic flame temperature in which the air mass flow rate is gradually decreased once thermal equilibrium has been achieved, (ii) Constant air flow rate in which the equivalence ratio is varied by increasing fuel flow rate through small steps. The results of this study indicate that low-conductivity injectors as well as cooling down burner rims increase the resistance to the flashback.

Ebi et al. [61] deals from an experimental point of view a more representative configuration by investigating a swirl flame at high pressure and pre-heated conditions for different hydrogen content. The work addressed to study perfectly premixed conditions in which the flashback is triggered once a stable flame is established by increasing the equivalence ratio. The optical access to the injector coupled with detailed measurements permits to identify that a flashback occurs when the flame can sustain the high shear stress in the turbulent boundary layer.

Recently, Zhang et al. [62] investigated numerically through high-fidelity Large Eddy Simulation with the flame-surface-density method the flashback dynamics observed in [61]. After the identification of the modes of flame stabilization and BLF in the mixing tube, an algebraic model is developed to predict the BLF limit.

Further steps on the same burner are carried out by Ranjan et al. in [63] by exploring stratified flames configuration. Starting from a stable flame configuration, a step increase in the equivalence ratio is provided to trigger the flashback and four distinct stages are identified. It is also found that the interaction between the flame and the fuel-rich pockets assists its propagation and consequent flashback-to-flameholding process.

However, although the previously mentioned works investigate the flashback mechanism in hydrogen flames, each of them induces the flashback by starting from a stable flame configuration and then varying a boundary condition. Therefore, to the best of the author's knowledge, no one has yet systematically investigated flashback problems after the ignition process, except for the experimental work reported in [30, 64]. The study evaluates the impact of hydrogen content on the ignition process for three different values of exhaust backpressure. Both of these parameters play a key role in the overpressure that is generated during the ignition phase, as previously highlighted, drastically varying the system response and facilitating the triggering of flashback mechanisms. Nevertheless, no work has studied these mechanisms from a numerical point of view, and therefore, this thesis work aims to address this lack.

1.1.3 Light-round

The last step in the ignition process is the light-round phase, which, once the flame is stabilized on the first burner, involves its propagation to the next burner until the entire chamber is ignited. This step only occurs if a multi-burner configuration is considered. The detailed study of this phase has only occurred in the last years for two main reasons. The first reason is that any ignition failure is most likely to occur in the first two phases, despite the fact that this phase also has a stochastic nature that strongly depends on the position of the igniter [43, 65]. The second reason is due to the complexity of making a test rig from an experimental point of view and the computational cost required from a numerical perspective. Indeed, the first numerical study of the light-round phase was conducted in 2008 by Boileau et al. [66] in a combustion chamber with 18 burners. Since then, research on this phase has progressed both experimentally, for spray [67, 68, 69, 70] and gaseous [69] flames, and numerically with both URANS [71] and LES [23, 67, 71, 72, 73, 74] approaches.

More details about this stage are not given in this thesis for the sake of brevity, the interested reader is referred to [23].

1.2 Final considerations

This chapter describes the main phases of the ignition process of a combustor, focusing on the different characteristic times and scale lengths involved in each of them. Particular attention is given to the second phase as it is of great interest in the development of a new combustor and is the one investigated in this thesis. The use of hydrogen presents new design challenges compared to classical liquid fuels. Previously, the main challenge was achieving proper atomization and reignition of the combustor at high altitudes.

Hydrogen, with its high reactivity, eliminates this issue. However, the primary risk now is properly stabilizing the flame in the burner to prevent flashback phenomena caused by the high overpressure that occurs during this process. In this optics, the study of these phenomena although given that URANS simulations provide interesting insights, high-fidelity methodologies such as LES remain an indispensable tool for the treatment of this unsteady process.

Chapter 2

Turbulent hydrogen flames modeling

The present chapter is divided into two sections. In the first one, the main methodologies for the numerical modeling of a turbulent reactive hydrogen flame are presented, paying attention also to the ignition part. The set of *Navier-Stokes Equations* (NSE) is first introduced for a multi-species reacting flow in the LES framework.

Then, two methods to handle the turbulence-chemistry interaction in the LES approach are introduced, highlighting their main characteristics and assumptions. An extension of the pure FGM approach to take into account the stretch and heat loss effects is described and verified through the comparison with premixed twin counterflow flames in terms of consumption speed taking as a reference the solution retrieved by Cantera. Finally, the model to account for the initiation of the reactions in the ignition simulation is addressed by paying attention to the coupling with the selected turbulent combustion model.

In the second part, an assessment of the numerical models employed is performed analyzing the reaction mechanisms, the effect of stretch and the thermal diffusion through low and high-order methods.

2.1 Numerical models

The set of NSE equations for a reacting flow field describes the conservation of mass, momentum and energy. Since a multi-species is considered, further $N-1$ transport equations are required to describe the N species composing the mixture. A brief recall is here reported.

The mass conservation equation can be expressed as:

$$\frac{\partial \rho}{\partial t} + \boldsymbol{\nabla} \cdot (\rho \boldsymbol{u}) = 0 \tag{2.1}$$

in which ρ and u represent the mixture density and velocity, respectively.

The momentum equation reads:

$$\frac{\partial \rho \boldsymbol{u}}{\partial t} + \boldsymbol{\nabla} \cdot (\rho \boldsymbol{u}\boldsymbol{u}) = -\boldsymbol{\nabla} P + \boldsymbol{\nabla} \cdot \boldsymbol{\tau} + \rho \boldsymbol{g} + \boldsymbol{F} \tag{2.2}$$

where P is the pressure, $\rho \boldsymbol{g}$ the gravitational body force and $\boldsymbol{F}$ the external body force. τ represents the viscous stress tensor.

The energy conservation equation reads:

$$\frac{\partial \rho E}{\partial t} + \boldsymbol{\nabla} \cdot [\boldsymbol{u}\,(\rho E + P)] = -\boldsymbol{\nabla} \cdot \boldsymbol{q} + \boldsymbol{\nabla} \cdot (\boldsymbol{\tau} \cdot \boldsymbol{u}) + \dot{\omega}_t \tag{2.3}$$

in which E stands for the specific total non-chemical energy (Eq. 2.4), $\dot{\omega}_t$ is the heat of reaction and $\boldsymbol{q}$ is the energy flux term.

$$E = h - \frac{P}{\rho} + \frac{\boldsymbol{u}^2}{2} \qquad , \qquad h = \sum_{k=1}^{n_{spec}} h_k Y_k \tag{2.4}$$

In Eq. 2.4, h represents the sensible enthalpy that does not include the enthalpy formation part.

Lastly, the transport equation for the k^{th} species mass fraction Y_k reads:

$$\frac{\partial \rho Y_k}{\partial t} + \boldsymbol{\nabla} \cdot (\rho \boldsymbol{u} Y_k) = -\boldsymbol{\nabla} \cdot \boldsymbol{J}_k + \dot{\omega}_k \quad \text{for } k = 1, N-1 \tag{2.5}$$

where $\dot{\omega}_k$ is the reaction rate of the k^{th} species related to the production/-consumption of the species due to the reactions. $\boldsymbol{J}_k$ represent the diffusive

mass flux of the k^{th} species and in ANSYS Fluent [75] it is expressed as:

$$\boldsymbol{J}_k = \rho Y_k \boldsymbol{V}_k \tag{2.6}$$

in which $\boldsymbol{V}_k$ is the diffusion velocity of species k. The direct computation of the diffusive mass fluxes based on Maxwell Stefan's equation is a challenging task, therefore approximations are typically obtained by using the so-called transport models. In the literature [76], three approaches are presented: the full Multicomponent, the Mixture-average and the unity-Lewis number assumption.

In the multicomponent approach, the diffusive mass flux can be expressed as:

$$\boldsymbol{J}_k = -\sum_{j=1}^{N-1} \rho D_{ij} \nabla Y_j - D_{T,i} \frac{\nabla T}{T} \tag{2.7}$$

D_{ij} and $D_{T,i}$ represent respectively the mass diffusion of species i into species j and the thermal diffusion of species i. When mass diffusion is considered a binary process, D_{ij} results in a symmetric matrix. The second term on the right-hand side of Eq. 2.7 represents thermal diffusion, also known in the literature as the Soret effect. This effect leads to changes in species concentration due to temperature gradients, which results in the diffusion of light species towards regions with higher temperatures [77].

In the mixture-average approximation, the mass diffusion coefficient $D_{i,m}$ for the species i into the mixture m is used and this allows to reduce the numerical efforts while preserving a high level of accuracy. As reported in Eq. 2.8, the first term depends exclusively on the gradient of species k and no longer on that of all N species in the mixture.

$$\boldsymbol{J}_k = -\rho D_{i,m} \nabla Y_k - D_{T,i} \frac{\nabla T}{T} \tag{2.8}$$

It is important to emphasize that this approximation violates the mass conservation principle [78], therefore, to overcome this problem, a corrective term $\boldsymbol{V}_c$ is added to the diffusion velocity $\boldsymbol{V}_k$ in the species transport equation in order to ensure the global mass conservation [76].

These two methods allow to include the effect of the different diffusion velocities of species, leading to the phenomenon known as preferential diffusion [79]. This effect causes variations in the local stoichiometry affecting temperature, fuel mass burning rate and the flame structure [80].

The unity-Lewis number assumption is the last and easiest method to implement among the previously mentioned models. The Lewis number of the generic species k compares the heat diffusivity of the mixture with the mass diffusivity of the species:

$$Le_k = \frac{\lambda}{\rho c_p D_k} \tag{2.9}$$

λ, ρ and c_p are respectively the thermal conductivity, the density and the specific heat at constant pressure. When Le_k is constant and equal to one for all species, the effects of preferential diffusion are not considered and the mass diffusion coefficient can be derived from the thermal diffusion coefficient as reported in Eq. 2.10.

$$D_k = \frac{\lambda}{\rho c_p} \tag{2.10}$$

This approximation is commonly used for hydrocarbons [79, 81], however, as highlighted in Sec. 2.2.3, it is inadequate for hydrogen resulting in significant discrepancies in the evolution and structure of the flame. However, a strategy is also present that builds on the latter assumption by assuming a constant Lewis number for each species but different from 1 that permits preferential diffusion effects to be included. Various studies can be found in the literature that use this model like the on of [82].

Finally, to close the set of NSE, the perfect gases state equation is added:

$$P = \rho \mathcal{R} T \tag{2.11}$$

with $\mathcal{R} = 8.314$ J.mol^{-1}.K^{-1} the universal gas constant.

2.1.1 Filtered NSE in the LES framework

Different strategies are possible to numerically solve the NSE equations. In this context, only the Large Eddy Simulation (LES) procedure is briefly introduced since it represents the approach used in this thesis. In the LES framework, the set of NSE is subjected to a filtering operation in which the filter size, represented by the grid dimension, discriminates between the resolved and modeled parts of the turbulent spectrum. In particular, the larger scales are resolved (at least 80% of the turbulence), whereas the scales below the filter dimension, referred to as SubGrid Scales (SGS) in the following, are modeled by exploiting the hypothesis of isotropy and self-similarity behavior.

The other two approaches are represented by the Direct Numerical Simulation (DNS) and Reynolds-Averaged Navier Stokes (RANS) in which the turbulent spectrum is completely resolved and modeled, respectively. In a reactive flow, since the combustion process occurs at the smaller scales, apparently there are no advantages over a RANS approach. Nevertheless, the largest modeled scales exhibit similar behavior to the smallest resolved ones and it is possible to use the information obtained from their resolution to develop models more reliable than those implemented in a RANS approach. This leads to a more accurate prediction of the flow field and, consequently, of the conditions under which chemical reactions occur. Furthermore, the subgrid scales are the most expensive to solve and their modeling leads to a substantial reduction in the computational efforts required compared to a DNS approach. In conclusion, the LES approach represents a good compromise allowing the key information to be accounted for with respect to RANS with a reasonable computational effort.

Taking a generic variable $\theta(x)$, applying the filter operation $\bar{\theta}(x)$ [78] consists in:

$$\bar{\theta}(\mathbf{x}) = \int \theta\left(\mathbf{x}'\right) F_{\Delta}\left(\mathbf{x} - \mathbf{x}'\right) d\mathbf{x}' \tag{2.12}$$

where $\bar{\theta}(\mathbf{x})$ denotes the resolved part of $\theta(\mathbf{x})$ and F_{Δ} the LES filter. In ANSYS Fluent [75], a box filter [78] is used based on the filter width Δ

that corresponds to the grid size, as previously pointed out. As variable density flows are considered, the Favre-filtering operation (weighted by the density) is preferred in this case ($\tilde{\cdot}$):

$$\bar{\rho}\tilde{\theta}(\mathbf{x}) = \int \rho\theta\left(\mathbf{x}'\right) F_{\Delta}\left(\mathbf{x}-\mathbf{x}'\right) d\mathbf{x}' \tag{2.13}$$

Applying the filter procedure to the NSE equation results in Eq. 2.14 for the continuity equation.

$$\frac{\partial\bar{\rho}}{\partial t} + \boldsymbol{\nabla}\cdot(\bar{\rho}\tilde{\boldsymbol{u}}) = 0 \tag{2.14}$$

The filtered momentum equation reads:

$$\begin{aligned} \frac{\partial\bar{\rho}\tilde{\boldsymbol{u}}}{\partial t} + \boldsymbol{\nabla}\cdot(\bar{\rho}\tilde{\boldsymbol{u}}\tilde{\boldsymbol{u}}) = \\ -\boldsymbol{\nabla}\overline{P} + \boldsymbol{\nabla}\cdot\overline{\boldsymbol{\tau}} + \bar{\rho}\boldsymbol{g} - \boldsymbol{\nabla}\cdot(\bar{\rho}\widetilde{\boldsymbol{u}\boldsymbol{u}} - \bar{\rho}\tilde{\boldsymbol{u}}\tilde{\boldsymbol{u}}) + \overline{\boldsymbol{F}} \end{aligned} \tag{2.15}$$

where the term related to the SGS stress $\bar{\boldsymbol{\tau}}_{sgs} = \bar{\rho}\widetilde{\boldsymbol{u}\boldsymbol{u}} - \bar{\rho}\tilde{\boldsymbol{u}}\tilde{\boldsymbol{u}}$ needs to be modeled with a specific closure, as discussed in the next section (Sec. 2.1.2).

The filtered energy equation reads:

$$\begin{aligned} \frac{\partial\bar{\rho}\tilde{E}}{\partial t} + \boldsymbol{\nabla}\cdot\left(\bar{\rho}\tilde{\boldsymbol{u}}\tilde{E} + \overline{P\boldsymbol{u}}\right) = \\ -\boldsymbol{\nabla}\cdot\bar{\boldsymbol{q}} + \boldsymbol{\nabla}\cdot(\overline{\boldsymbol{\tau}\cdot\boldsymbol{u}}) - \boldsymbol{\nabla}\cdot\left(\bar{\rho}\widetilde{\boldsymbol{u}E} - \bar{\rho}\tilde{\boldsymbol{u}}\tilde{E}\right) + \overline{\dot{\omega}}_t + \overline{\dot{Q}} \end{aligned} \tag{2.16}$$

in which $\overline{\dot{Q}}$ represents a custom source term explained in the next section (Sec. 2.1.4) to model the ignition. The SGS heat flux $\bar{\rho}\widetilde{\boldsymbol{u}E} - \bar{\rho}\tilde{\boldsymbol{u}}\tilde{E}$ is addressed in Sec. 2.1.2.

Lastly, the filtered equation for the Y_k reads:

$$\frac{\partial\bar{\rho}\widetilde{Y}_k}{\partial t} + \boldsymbol{\nabla}\cdot(\bar{\rho}\tilde{\boldsymbol{u}}\widetilde{Y}_k) = -\boldsymbol{\nabla}\cdot\overline{\boldsymbol{J}}_k - \boldsymbol{\nabla}\cdot(\bar{\rho}\widetilde{\boldsymbol{u}Y}_k - \bar{\rho}\tilde{\boldsymbol{u}}\widetilde{Y}_k) + \overline{\dot{\omega}}_k \tag{2.17}$$

The filtered diffusion flux $\overline{\boldsymbol{J}}_k$ is not here reported for the sake of brevity while the SGS unresolved species flux $(\bar{\rho}\widetilde{\boldsymbol{u}Y}_k - \bar{\rho}\tilde{\boldsymbol{u}}\widetilde{Y}_k)$ is addressed in Sec. 2.1.2.

2.1.2 Turbulence modeling

In this part, the closure of the SGS terms arises after the filtering procedure is provided. In ANSYS Fluent the Boussinesq hypothesis is employed, so the stress tensor $\overline{\tau}_{sgs}$ that appears in Eq. 2.15 can be written as:

$$\bar{\boldsymbol{\tau}}_{sgs} - \frac{\boldsymbol{I}}{3}\bar{\boldsymbol{\tau}}_{sgs} = \mu_{sgs}\left(\boldsymbol{\nabla}\tilde{\boldsymbol{u}} + \boldsymbol{\nabla}\tilde{\boldsymbol{u}}^T\right) \tag{2.18}$$

where the μ_{sgs} is the subgrid-scale turbulent viscosity. Several turbulent viscosity models are available in the literature to estimate μ_{sgs} including the Smagorinsky [83], the WALE [84] and SIGMA [85] model.

In the present work, the dynamic version of the Smagorinsky formulation is used. In fact, in the base version, the subgrid-scale turbulent viscosity is evaluated as:

$$\mu_{sgs} = (C_s\Delta)^2|\overline{S}| \tag{2.19}$$

where C_s and Δ are respectively the Smogorinsky constant and the grid size. This closure is based on the assumption of local equilibrium between the kinetic energy transferred to the sub-grid scale and the viscous dissipation [86]. This hypothesis is susceptible to failure whenever sources of anisotropy are present. Therefore, several modifications are proposed to ensure the correct asymptotic near-wall behavior of the SGS stresses [87]. Since the Smagorinsky constant C_s is a case-dependent input parameter, a possible issue could appear due to the fact that it is not possible to define a universal value. The enhancements proposed by Germano [88] and subsequently by Lilly [89], are essential to overcome these limitations. In his work, C_s is computed dynamically as the calculation progresses, using the information provided by the smallest resolved scales to model the sub-grid scales. For the sake of brevity, the mathematical formulation of the Dynamic Smagorinsky-Lilly model described in [88] and [89] is not here reported.

The last two terms that need to be modeled are the SGS fluxes in

Eq. 2.16 and Eq. 2.17. In ANSYS Fluent these terms are treated as:

$$\left(\bar{\rho}\widetilde{\boldsymbol{u}E} - \bar{\rho}\tilde{\boldsymbol{u}}\tilde{E}\right) = -\frac{\mu_{sgs}C_p}{\mathrm{Pr}_{sgs}}\boldsymbol{\nabla}\tilde{T} \tag{2.20}$$

and:

$$\left(\bar{\rho}\widetilde{\boldsymbol{u}Y_k} - \bar{\rho}\tilde{\boldsymbol{u}}\tilde{Y}_k\right) = -\frac{\mu_{sgs}}{\mathrm{Sc}_{sgs}}\boldsymbol{\nabla}\tilde{Y}_k \tag{2.21}$$

in which Pr_{sgs} and Sc_{sgs} are the sub-grid Prandtl and Schmidt number respectively.

2.1.3 Combustion modeling

As a result of the filtering process, two further terms need to be closed: filtered reaction rate $\overline{\dot{\omega}}_k$ in the generic species transport equation and the filtered heat release $\overline{\dot{\omega}}_t$ in the energy equation. Turbulent combustion models are derived for this purpose but a detailed explanation of these two terms (named for brevity $\dot{\omega}$ in the following) is not reported here and the readers interested in more details are referred to [78]. Furthermore, the necessity to employ a turbulent combustion model also arises from the fact that the thickness of the flame front, for typical industrial applications, is one or two orders of magnitude less than the LES calculation grids.

Before introducing the two turbulent combustion models, it is necessary to recall the basic concepts of the interaction between turbulence and the flame front to identify the different regimes in which combustion can occur. Since diffusive flames are not addressed in this thesis, only the analysis for premixed flames is reported. The readers interested in diffusive flames are referred to [78].

As well known, turbulence is characterized by length scales ranging from the smallest, with the limit the Kolmogorov scales, to the largest characterized by an integral scale length. Since all of them can interact with the flame, it is convenient to introduce two fundamental dimensionless parameters, the Damköhler (Da) and the Karlovitz (Ka) numbers. The Da number compares the time scales associated to the integral length with the chemical time scale while the Ka number analyzes the interaction

between the chemistry and the smallest turbulent scales.

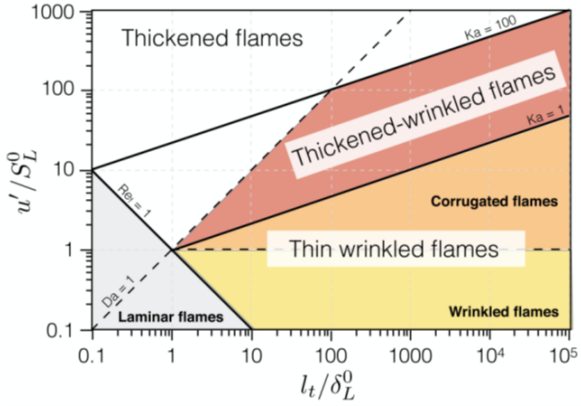

Figure 2.1: Peters diagram for premixed turbulent combustion [90].

As a function of these two parameters, three main combustion zones can be identified as reported in Peters diagram [90] shown in Fig. 2.1:

- Thin wrinkled flames: for $Ka < 1$ and $Da >> 1$ all the turbulent time scales are larger than the flame time scale so the flame front is corrugated by the large eddies while the inner flame structure is preserved. This regime is supported by the fast chemistry conditions so the flame front can be described as an ensemble of thin, laminar, locally one-dimensional flamelets.

- Thickened-wrinkled flames: for $Ka >> 1$ and $Da < 1$ the opposite regime is retrieved. The chemical reactions are slower than turbulent mixing so that turbulent structures can penetrate the reaction zone enhancing the turbulent diffusion.

- Thickened flames: for $Ka > 1$ and $Da > 1$ only the Kolmogorov scales can penetrate the reaction zone so the flame keeps its laminar structure.

2.1.3.1 Thickened Flame Model

The first model is the so-called Thickened Flame Model (TFM) [91]. Despite this method is theoretically developed for perfectly premixed flames, it is also extended for partially premixed and non-premixed ones [92] showing quite good results [23]. In this model, all the filtered equations from Eq. 2.14 to Eq. 2.17 are transported during the calculation.

The main idea of the TFM is to artificially thicken the flame front in order to be able to resolve it with the LES grid. From the dimensional analysis conducted by Williams [93], the laminar flame speed (s_l) and the laminar flame thickness (δ_l) are proportional to:

$$s_l \propto \sqrt{D_{th}\dot{\omega}} \qquad \delta_l \propto \sqrt{\frac{D_{th}}{\dot{\omega}}} \tag{2.22}$$

It is possible to obtain a thickened flame preserving the laminar flame speed by increasing the thermal diffusivity D_{th} and reducing the reaction rate by a factor $\mathcal{F}$:

$$\begin{aligned} s_l \propto \sqrt{\mathcal{F}D_{th}\frac{\dot{\omega}}{\mathcal{F}}} \quad &\rightharpoonup \quad s_l^{TFM} \propto \sqrt{D_{th}\dot{\omega}} = s_l \\ \delta_l \propto \sqrt{\frac{\mathcal{F}D_{th}}{\frac{\dot{\omega}}{\mathcal{F}}}} \quad &\rightharpoonup \quad \delta_l^{TFM} \propto \mathcal{F}\sqrt{\frac{D_{th}}{\dot{\omega}}} = \mathcal{F}\delta_l \end{aligned} \tag{2.23}$$

The thickening factor $\mathcal{F}$ is expressed as:

$$\mathcal{F} = N\Delta/\delta_l \tag{2.24}$$

where N is the number of points used to discretize the flame front and Δ is the grid size. For a sufficiently large value of the thickening factor $\mathcal{F}$, the flame front is resolved on the LES grid.

The thickening of the flame front modifies the interaction between combustion and turbulence. As evidenced by the decrease in the Damköhler number Eq. 2.25, the flame becomes less sensitive to the effects of turbulence.

$$Da = \frac{\tau_t}{\tau_c} = \frac{l_t}{u'}\frac{s_l}{\delta_l} \rightarrow Da^{TFM} = \frac{Da}{\mathcal{F}} \tag{2.25}$$

l_t is the turbulence integral length scale and u' represents the velocity fluctuations. The turbulent eddies smaller than δ_l^{TFM} cannot properly wrinkle the flame [94], leading to a decrease in the flame surface and consequently in the reaction rate. In order to compensate for this effect, an efficiency function E is used to increase D_{th} and $\dot{\omega}$. Therefore, the underestimation of the flame surface is balanced by an increase in the laminar flame speed:

$$\begin{aligned} \delta_l^{TFM} &\propto \mathcal{F}\sqrt{\frac{ED_{th}}{E\dot{\omega}}} = \mathcal{F}\delta_l \\ s_l^{TFM} &\propto \sqrt{ED_{th}\,E\dot{\omega}} = Es_l \end{aligned} \tag{2.26}$$

The efficiency function is defined as the ratio between the unthickened and thickened wrinkling factor Ξ:

$$E = \frac{\Xi|_{\delta=\delta_l}}{\Xi|_{\delta=\delta_l^{TFM}}} \tag{2.27}$$

Several formulations are present in the literature for the evaluation of the wrinkling factor. Here, for the sake of brevity, only the employed Colin [91] formulation is reported:

$$\Xi = 1 + \alpha\Gamma\left(\frac{\Delta}{\delta_l}, \frac{u'_\Delta}{s_l}\right)\frac{u'_\Delta}{s_l} \tag{2.28}$$

α is a function of the turbulent Reynolds number and u'_Δ is the sub-grid scale turbulent velocity. The Γ formulation and a detailed description of the model are discussed in [91]. A summary of the quantities involved in the TFM approach is reported in Table 2.1.

	Diff.	**React. rate**	**Flame speed**	**Thickness**
Laminar flame	D_{th}	$\dot{\omega}$	s_l	δ_l
Thickened lam. flame	$\mathcal{F}D_{th}$	$\dot{\omega}/\mathcal{F}$	s_l	$\mathcal{F}\delta_l$
Thickened turb. flame	$\mathrm{E}\mathcal{F}D_{th}$	$\mathrm{E}\,\dot{\omega}/\mathcal{F}$	Es_l	$\mathcal{F}\delta_l$

Table 2.1: Summary of the quantities involved in the TFM.

It is important to emphasize that the increase in thermal diffusivity in regions located far from the flame affects the mixing process leading

to incorrect behavior. Therefore, thickening is locally applied only in a narrow band near the flame front, defined by a sensor factor Ω:

$$\Omega = \tanh\left(\beta \frac{|\overline{R_i}|}{\max|\overline{R_i}|}\right) \tag{2.29}$$

$|\overline{R_i}|$ is the spatially filtered absolute value of the reaction rate i, defined by the user, and β is a constant with a default value of 10 [75].

According to Eq. 2.30, in the proximity of the flame, Ω is equal to one and the molecular diffusivity is enhanced by a factor EF, while outside of the band, where Ω is equal to zero, it is reduced to the non-thickened value.

$$D_{th,eff} = D_{lam}[1 + (EF - 1)\Omega] + D_{turb}(1 - \Omega) \tag{2.30}$$

D_{eff} indicates the effective thermal diffusivity, while D_{lam} and D_{turb} are respectively the laminar and turbulent diffusivity.

It is of paramount importance to underline that in this model, since a transport equation is transported for each species in the reaction mechanism used, it is possible to characterize the different diffusion velocities and thus include preferential diffusion effects.

2.1.3.2 Flamelet Generated Manifold

To avoid the solution of all the transport equations for every species included in the reaction mechanism, a common approach is to define appositely quantities that allow the description of the turbulent combustion. In this contest, the Flamelet Generated Manifold (FGM) [95] is a very appreciated solution for engineering applications for its good accuracy in a wide range of conditions, including perfectly and partially premixed flame [81, 96, 97], with a reduced computational cost.

The main idea of the FGM is that the thermochemical states of a turbulent flame can be assumed similar to the ones in a laminar flamelet. This assumption is true only in the flamelet regions (referred to Fig. 2.1) in which the turbulence does not destroy the inner laminar structure of the flame. The typical operating conditions of the gas turbines satisfy the

aforementioned requirement justifying the wide use of this combustion model.

As previously mentioned, one of the main advantages of the FGM method is the reduced number of transport equations. As far as concerns the FGM implemented in ANSYS Fluent® [75], in addition to the Eq. 2.14 and Eq. 2.15 which does not account for reaction phenomena, two independent control variables and relative equations are introduced. The first one is the mixture fraction Z which describes the mixing between the two streams by tracing the atomic mass fraction of single elements following the Bilger definitions [98], although other definitions are possible [99, 100]. The second one is the progress variable c which quantifies the progress of the reaction to chemical equilibrium conditions. It is worth remarking that ANSYS Fluent® solves a transport equation for the un-normalized progress variable Y_c typically defined as an arbitrary linear combination of species mass fraction Y_k:

$$Y_c = \sum \alpha Y_k \tag{2.31}$$

Then, in order to obtain the progress variable c, the un-normalized one is divided by its value at the chemical equilibrium:

$$c = \frac{\sum \alpha Y_k}{\sum \alpha Y_k^{eq}} \tag{2.32}$$

Both quantities, Z and c, range between 0 and 1 in which for mixture fraction 0 means usually pure oxidant while 1 is pure fuel. For the progress variable, 0 represents the unburnt state whereas 1 represents the fully burnt state at chemical equilibrium.

The two transport equations after the LES filtering procedure read:

$$\frac{\partial \overline{\rho}\widetilde{Z}}{\partial t} + \boldsymbol{\nabla} \cdot (\overline{\rho}\widetilde{\boldsymbol{u}}\widetilde{Z}) = \boldsymbol{\nabla} \cdot (\overline{\rho} D_{tot} \boldsymbol{\nabla} \widetilde{Z}) \tag{2.33}$$

$$\frac{\partial \overline{\rho}\widetilde{Y_c}}{\partial t} + \boldsymbol{\nabla} \cdot (\overline{\rho}\widetilde{\boldsymbol{u}}\widetilde{Y_c}) = \boldsymbol{\nabla} \cdot (\overline{\rho} D_{tot} \boldsymbol{\nabla} \widetilde{Y_c}) + \overline{\dot{\omega}}_c \tag{2.34}$$

in which the source term for the progress variable $\overline{\dot{\omega}}_c$ in Eq. 2.34 is

fundamental for the advancement of the reaction. On the contrary, since the mixture fraction is a passive scalar conserved across the domain, no source term appears. The total diffusivity D_{tot} is computed as the sum of the laminar diffusivity (λ/c_p), evaluated under the unity-Lewis number assumption Eq. 2.10, and the turbulent one (μ_t/Sc_t). Before addressing the closure of the source term, it is necessary to explain how the turbulence-chemistry interaction is included with this method.

At this point, a laminar look-up table $\Psi(Z, c)$ which describes species mass fraction and temperature can be constructed by solving either premixed or diffusion laminar flamelets as a function of the selected control variables (Z, c). The main advantage of this approach lies in the possibility of using a detailed reaction mechanism for the construction of the laminar look-up table.

The influence of the turbulence is accounted for by a stochastic description of the variables through a Probability Density Function (PDF). The PDF, in the following indicated as P(x), can be seen as the fraction of the time in which the fluid spends in the state x [101]. Therefore, the fluctuation of a generic quantity $\varphi(Z, c)$ extracted from the laminar manifold (e.g. species mass fraction) due to the turbulence must be attributed to the fluctuation of Z, c or both Z and c.

If the PDF of the generic variable φ is known, the Favre average of the quantity $\tilde{\varphi}$ can be expressed as:

$$\tilde{\varphi} = \int_0^1 \int_0^1 \varphi(Z, c)\tilde{P}(Z, c)dZdc \tag{2.35}$$

Since the $\tilde{P}(Z, c)$ is not known and its computation increases the computational efforts, a presumed shape PDF approach is adopted in which the $\tilde{P}(Z, c)$ distribution is assumed *a priori* to be a β-distribution. Furthermore, with the assumption of statistical independence between Z and c [75], it can be expressed as:

$$\tilde{P}(Z, c) = \tilde{P}(Z)\tilde{P}(c) \rightarrow \begin{cases} \tilde{P}(Z) = \tilde{P}(Z, \tilde{Z}, \widetilde{Z''^2}) \\ \tilde{P}(c) = \tilde{P}(c, \tilde{c}, \widetilde{c''^2}) \end{cases} \tag{2.36}$$

in which $\widetilde{Z''^2}$ and $\widetilde{c''^2}$ represent the variance of mixture fraction and progress variable respectively. By solving a transport equation for these additional two quantities, the problem is mathematically closed. For the sake of brevity, the transport equations are not reported here, more information about their implementation can be found in [75].

Nevertheless, computing the mean quantities at runtime according to Eq. 2.35 requires an additional computing time that could be avoided. In fact, the integration of the PDF could be done in the pre-processing stage as well by adopting multiple different PDFs defined on a discrete $Z - c$ grid since they range in a restricted space:

$$\begin{aligned} \widetilde{Z''^2} &\in [0, \tilde{Z}(1-\tilde{Z})] \\ \widetilde{c''^2} &\in [0, \tilde{c}(1-\tilde{c})] \end{aligned} \tag{2.37}$$

In conclusion, the generic turbulent quantity $\tilde{\varphi}$ is retrieved from the pre-integrated table as:

$$\tilde{\varphi} = \tilde{\varphi}(\tilde{Z}, \widetilde{Z''^2}, \tilde{c}, \widetilde{c''^2}, \tilde{h}) \tag{2.38}$$

Actually, since the flamelets are considered adiabatic during the solution, an enthalpy defect h may be included during the integration of the manifold. A detailed description of the enthalpy defect and its implementation in ANSYS Fluent®can be found in [75].

Finally, the last part that needs to be discussed is the closure of the progress variable source term $\overline{\dot{\omega}}_c$. In this case, as for a common variable in Eq. 2.35, the reaction progress is directly related to the pre-integrated manifold as a function of quantities reported in Eq. 2.38 [75, 101]:

$$\overline{\dot{\omega}}_c = \overline{\rho} \iint \frac{\dot{\omega}_c(Z,c)}{\rho(Z,c)} \tilde{P}(Z,c) dZ dc \tag{2.39}$$

where $\dot{\omega}_c(Z,c)$ is the reaction rate extracted from the laminar manifold. This approach does not include any hypothesis on the flame other than those made for the use of FGM.

2.1.3.3 Extended Flamelet Generated Manifold

In this section, an extension of the FGM model developed within this thesis work is presented. Indeed, it is important to underline how the basic model previously presented can not natively account for preferential diffusion effects with only two control variables (mixture fraction and progress variable).

However, several works are present in the literature that discuss and overcome these limitations by including directly the preferential diffusion effects on the governing equations. Swart et al. in [79] introduce in the transport equations of the control variables an additional diffusive term to include the low Lewis number effects. In this way, the preferential diffusion contribution can clearly be distinguished from the non-preferential one. Thus, under the assumption that the progress variable gradient is much larger than the gradient of the other control variables, the evaluation of the additional terms requires the assessment of the diffusion coefficients which can be done in the pre-processing stage as well. Donini et al. in [102] extended the work [79] applying the approach to a 3D FGM using progress variable, mixture fraction based on Bilger definition [98] and enthalpy as control variables. Recently, further improvements to the model are performed including also the cross-diffusion terms, so the preferential diffusion flux is a function of the other control variables and not only of the progress variable. This approach is validated against a reference simulation in [103] and experiments [104].

Although all previous methods allow the inclusion of preferential diffusion, stretch effects and heat losses to the flame, they require an increase in the size of the look-up table or the solution and storage of cross-diffusion terms that increase drastically the computational cost.

For that reason, other strategies to account for the non-unity Lewis number effects without modifying the governing equations are present. Kutkan et al. proposed in both RANS [105] and LES [106] framework a new approach based on Zimont's closure [107] in which the reaction progress source is a function of the mixture Lewis number. In 2016 Klarmann et al. [108] formalized an extension of the FGM to account for the

aforementioned effects with the inclusion of a pre-tabulated table, named Γ, which affects the reactivity. An application in the LES framework of the model can be found in [109].

Following the original work [108], a novel formulation for the Gamma (Γ) function is introduced and validated. The extension acts on the progress variable source term (Eq. 2.39) as:

$$\overline{\dot{\omega}}_c = \Gamma(Z,\psi,k)\overline{\rho}\iint \frac{\dot{\omega}_c(Z,c)}{\rho(Z,c)}\tilde{P}(Z,c)dZdc \tag{2.40}$$

where $\Gamma(Z,\psi,k)$ multiplies the turbulent source term. $\Gamma(Z,\psi,k)$ is tabulated as a function of stretch k and heat losses ψ.

In [108] Γ is defined as:

$$\Gamma(Z,\psi,k) = \left(\frac{s_c(k,\psi,Z)}{s_c^0(Z)}\right)^m \tag{2.41}$$

where s_c is the consumption speed in the non-adiabatic strained condition while the superscript $(...)^0$ denotes the adiabatic and unstrained ones. In Eq. 2.41, the exponent m represents the proportionality between the consumption speed s_c and the progress variable source term $\overline{\dot{\omega}_c}$ which must be determined as a function of several parameters (operating conditions, fuel, ...). The heat loss parameter ψ is calculated as:

$$\psi = \frac{T_b}{T_{eq}} \approx \frac{\tilde{T}(\tilde{Z},\widetilde{Z''^2},\tilde{c},\widetilde{c''^2},\tilde{h})}{\tilde{T}_{ad}(\tilde{Z},\widetilde{Z''^2},\tilde{c},\widetilde{c''^2},\tilde{h}_{ad})} \tag{2.42}$$

where T_b and T_{ad} are respectively the burnt and adiabatic flame temperature.

Under the assumption of a thin flame front, the stretch can be calculated as the sum of two different contributions: the fluid strain rate tangential to the flame named strain and the flame sheet curvature [78]. As it is beyond the scope of this section and no modifications are done on that part, the reader interested in the evaluation and implementation of the stretch is referred to [108, 110, 111].

Since the original model necessitates some case-dependent user input

(exponent m), a new general formulation for Γ is introduced.

This is defined as the ratio of the maximum laminar strained progress variable source term to the laminar unstrained adiabatic value in physical space:

$$\Gamma(Z,\psi,k) = \frac{\max \dot{\omega}_c(Z,\psi,k)}{\max \dot{\omega}_c^0(Z)} \tag{2.43}$$

With respect to the original formulation, no tuning parameters are required since the construction of the Γ table can be directly performed by solving different strained and unstrained laminar flames. Therefore, the model does not depend on the test case and it should provide a more suitable alternative also for 100% hydrogen flames.

In fact, to generate the Γ table, the Cantera libraries [112] can be used to solve several freely propagating flames (k=0 s^{-1}) and premixed counter-flow flames (k>0 s^{-1}) by varying both inlet velocity and composition. The strain and mixture fraction space are consequently explored. Finally, for each heat loss coefficient $\psi < 1$, the corresponding burnt temperature T_b is evaluated according to its definition and set as a boundary condition. It is worth remarking that with 1D flames the curvature is zero, so the strain level calculated as the first maximum of the velocity before the flame front is considered representative of the whole stretch. This assumption can be justified, as explained in [108], that for high turbulence flows (Ka>1), the curvature contribution to stretch is at least one order of magnitude lower than the strain one.

Furthermore, it is very important to highlight that a laminar term ($\Gamma(Z,\psi,k)$) is applied to a turbulent one ($\overline{\dot{\omega}}_c$). In fact, the assessment of the probability density function of strain and heat loss is not straightforward and strongly depends on the current test case [110]. For these reasons, it is decided to avoid the calculation of *PDF(ψ,k)* in order to keep constant the computational efforts with respect to the baseline model. In the end, the correction acts by scaling the turbulent reaction source term without changing its shape.

With these assumptions, the peak of the reactivity is reconstructed, as reported in Fig. 2.2 where two 100% H_2 laminar flames computed

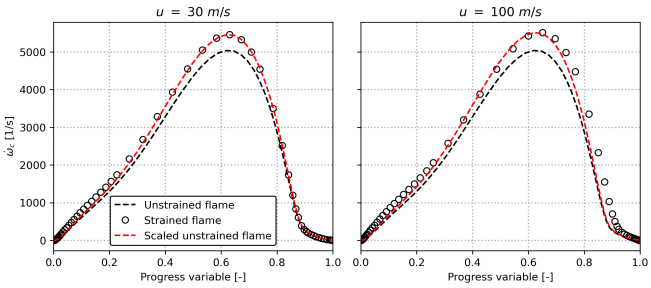

Figure 2.2: Progress variable source term in the progress variable space for two different inlet velocities. Premixed counterflow flames at p_{atm}, $T = 570K$ *and* $\phi = 0.6$.

with Cantera at different inlet velocities (strain rate levels) are shown. The dotted lines and the circles identify respectively the unstrained and strained solutions in terms of the progress variable source term in the progress variable space. The dotted red line instead represents the unstrained flame scaled by $\Gamma(Z, \psi, k)$ factor according to the proposed formulation (for the sake of clarity, the adiabatic conditions are considered). The unnormalized progress variable is defined as $Y_c = Y_{H_2O} - Y_{H_2}$ as better explained in Sec. 3.2.3. In the progress variable space, the scaled solution well reconstructs the peak of the reactivity. Nevertheless, as far as concerns the flame prediction, one of the key parameters that must be correctly captured by the numerical model is the consumption speed s_c. In a tabulated-chemistry approach as FGM, it can be evaluated by modifying its original definition [78] as:

$$s_c = \frac{1}{\rho_u (Y_{c,b} - Y_{c,un})} \int_{-\infty}^{+\infty} \dot{\omega}_c(Z, c) \rho dx \tag{2.44}$$

in which ρ_u represents the unburnt density.

Since the assessment of the consumption speed requires the integration of the flame in the physical space, a direct evaluation in Fluent must be done. A preliminary analysis of the consumption speed s_c retrieved from the PDF is performed before testing the extended model with the basic

FGM since the purpose of this part is to verify the PDF used (which remains unchanged in the subsequent analysis with the two models).

To do that, a one-dimensional freely propagating flame is directly computed in ANSYS Fluent®employing the current PDF. The domain reported in Fig. 2.3 is characterized by a predominant dimension compared to the others, allowing for the representation of a 1D flame in a 3D domain. The computational grid consists of equally-spaced hexahedral elements with a size, along the main direction of flame propagation, of Δx.

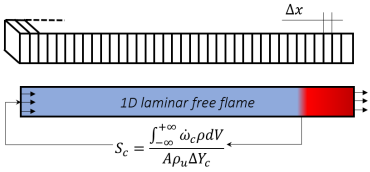

Figure 2.3: Sketch of the 1D freely-propagating flame implemented in Fluent.

The simulation is performed with the pressure-based solver and the Coupled algorithm, by imposing a constant time step equal to $1 \cdot 10^{-6}$ s. The PDF is generated with the detailed ELTE mechanism [113] through premixed flamelets. The solution is initialized with the nominal conditions in terms of composition ($\phi = 0.6$) and temperature ($T = 570\ K$). Subsequently, a part of the domain is patched with the chemical equilibrium composition of the burnt mixture (PV=1), in order to initiate the reactions. The flame starts to propagate and a time-dependent inlet boundary condition is imposed: the consumption speed is calculated at each time step and cyclically set at the velocity inlet. The simulation is run until a stationary condition is reached and the flame is stable in the domain. The final value imposed at the inlet represents the consumption speed retrieved from the PDF table. It is mandatory to highlight that the variances of both mixture fraction and progress variable are not resolved since laminar conditions are considered in this case ($\widetilde{Z''^2} = 0, \widetilde{c''^2} = 0$). Several meshes are tested by varying the element size of the grid (which corresponds to a different number of elements inside the laminar flame

thickness $\delta_{cantera}$) and the results are reported in Fig. 2.4.

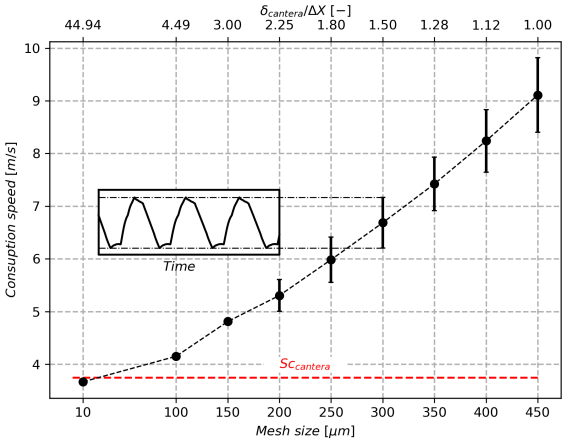

Figure 2.4: Consumption speed assessment from 1D laminar freely-propagating flames by varying the element grid size.

When a very fine mesh size is employed ($\Delta x < 150\ \mu m$), the correct consumption speed is retrieved from the PDF according to the value computed with the Cantera. Instead, when a coarser mesh is used, an overestimation of the reactivity is evident with a constant periodic fluctuation of the inlet velocity. In conclusion, when a laminar case is simulated in Fluent®with a tabulated chemistry approach, to correctly discretize the flame front and retrieve a proper consumption speed, at least 40 points are required within the flame front.

Subsequently, to assess the capability of the proposed model in strained conditions, a twin counterflow configuration is implemented in ANSYS Fluent ®with the standard (FGM) and the extended (E-FGM) models. The results are then compared to the reference solution provided by Cantera. A sketch of the computational domain with the prescribed boundary conditions and mesh grid is reported in Fig. 2.5. The domain consists of a quarter of the canonical domain in which a symmetry boundary condition

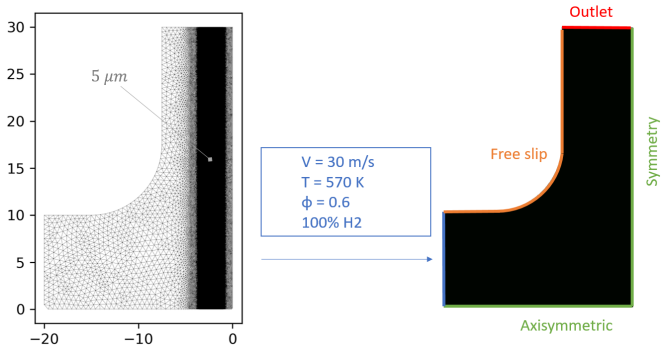

Figure 2.5: Sketch of the computational domain and grid with the prescribed boundary conditions for the twin counterflow flame implemented in Fluent.

is imposed along the vertical axis and an axisymmetric condition on the horizontal one. A free-slip condition is set to mimic the far field whereas the atmospheric pressure is prescribed at the outlet patch. A velocity inlet equal to 30 m.s^{-1} at T = 570 K of hydrogen-air perfectly premixed at ϕ = 0.6 is set at the inlet patch placed on the left of the domain. The mesh consists of 6.5 M of triangle elements with a specific refinement in the flame stabilization zone at 5 µm according to the outcomes of the previous analysis (the sizing is further reduced since strained conditions are now considered). The simulations are carried out with the pressure-based solver and the Coupled algorithm, by imposing a constant time step equal to $1 \cdot 10^{-7}$ s. The same PDF previously described is here adopted for both models.

An overview of the axial velocity, temperature and progress variable source term field is presented in Fig. 2.6. The axial velocity starts to decrease due to the domain configuration until close to the flame front there is a velocity jump due to the density jump. As this is a twin counterflow configuration, there is the formation of a flame front with the presence of burnt gas between it and the vertical symmetry of the domain. It is important to note that in this case there is a characteristic

strain rate of about 3000 s^{-1} and the flame front is completely within the refinement zone, which allows it to be correctly discretized.

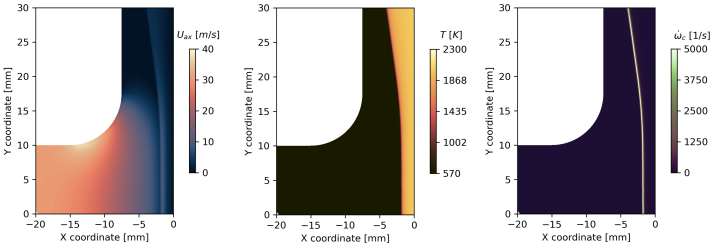

(a) Axial velocity *(b) Temperature* *(c) PV source term*

Figure 2.6: Contours of axial velocity, temperature and progress variable source term for E-FGM.

To validate the velocity and temperature fields, a comparison with the reference solution obtained with Cantera is reported in Fig. 2.7 in which the numerical results are extracted from the horizontal axis (y = 0 mm).

The black circle identifies the reference solution while the solid line represents the baseline FGM simulation. Finally, the red line represents the extended case (E-FGM) in which the correction of the source term is applied. A good agreement is shown for both simulations even if the E-FGM case better predicts the ignition of the fresh mixture. As previously reported, the reaction source term is plotted in both physical and progress variable space in Fig. 2.8. The peak of the reactivity is well reproduced for the extended simulation with respect to the baseline one. At this point, after the validation of the simulations, it is possible to integrate the solution over the physical space (along the horizontal symmetry y = 0 mm with Eq. 2.44) to calculate the consumption speed, as reported in Tab. 2.2.

For a better comparison, an additional inlet velocity equal to 100 $m.s^{-1}$ (strain rate $\approx$ 10000 s^{-1}) is tested in which all the fields are not reported here for the seak of brevity. Although the underestimation of the consumption speed provided by the baseline simulations (FGM) with

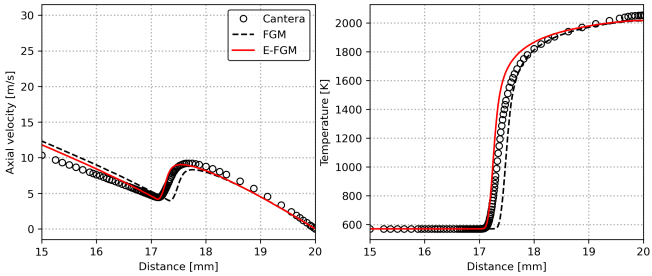

Figure 2.7: Axial velocity and temperature profile for 30 $m.s^{-1}$ case. Premixed twin counterflow flame at $p = p_{atm}$, $T = 570K$ and $\phi = 0.6$.

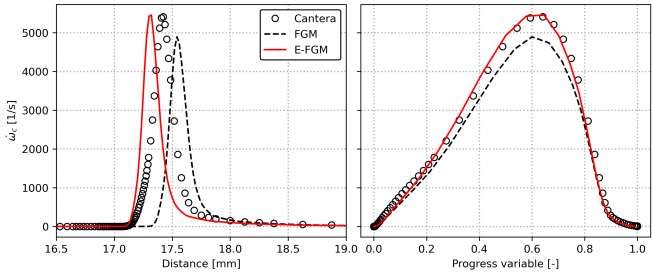

Figure 2.8: Progress variable source term in both physical (left) and progress variable space (right). Premixed twin counterflow flame at $p = p_{atm}$, $T = 570K$ and $\phi = 0.6$.

respect to the reference value is limited for these conditions, the effects of the correction to the final solution are evident and increase the accuracy. More in detail, since the flame thickness remains quite constant for the same inlet velocity, the higher reaction rate allows the reduction of the discrepancy with respect to the baseline simulation. It is mandatory to recall that this correction does not increase the computational efforts of the simulations and only a pre-processing procedure is required when the operating conditions are defined.

	Inlet velocity	
	30 m.s^{-1}	100 m.s^{-1}
s_c^{ref} [m.s^{-1}]	3.72	3.41
s_c^{FGM} [m.s^{-1}]	3.34	3.12
s_c^{E-FGM} [m.s^{-1}]	3.58	3.30

Table 2.2: Assessment of consumption speed for FGM and E-FGM for two inlet velocities.

2.1.4 Spark modeling

In this work, the Energy Deposition (ED) model proposed by Lacaze [36], is used to describe the spark ignition. As described in Ch. 1, the initial stages of kernel formation are characterized by time and length scales extremely reduced and challenging to resolve [23]. With the ED model, a simplified description of the initial stage of the ignition process is achieved using an energy profile that mimics the real spark, while the temperature is below the ionization temperature, neglecting the plasma phase (Fig. 2.9).

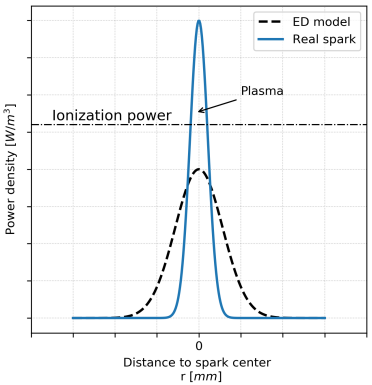

Figure 2.9: Qualitative sketch of power distributions for a real spark and for the ED model.

The spark is modeled by adding an explicit source term to the energy equation ($\overline{\dot{Q}}$ in Eq. 2.16), with a Gaussian distribution in both time and space. The volumetric source term $\dot{Q}$ is expressed as:

$$\dot{Q}(r,t) = \frac{E_i}{4\pi^2\sigma_t\sigma_s^3} e^{-\frac{1}{2}(\frac{r}{\sigma_s})^2} e^{-\frac{1}{2}(\frac{t-t_0}{\sigma_t})^2} \tag{2.45}$$

r is the distance from the spark center and t_0 identifies the time corresponding to the maximum value of the power density. The parameters σ_s and σ_t control the size and the duration of the source term and are defined as:

$$\sigma_s = \frac{\Delta_s}{a} \qquad\qquad \sigma_t = \frac{\Delta_t}{a} \tag{2.46}$$

The characteristic size Δ_s and duration Δ_t of the spark are divided by a factor $a = 4\sqrt{\ln 10}$ to obtain 98% of the deposited energy in the domain $\Delta_s^3 \times \Delta_t$ [36]. The choice of Δ_s is not to be intended as the size of the spark but instead to ensure that the maximum temperature at the kernel center, in the absence of any heat losses, does not exceed a predetermined temperature $T_{k,max}$ [114]:

$$\Delta_s = \frac{a}{\sqrt{2\pi}} \left(\frac{E_i}{\rho_0 c_p (T_{k,max} - T_0)} \right)^{1/3} \tag{2.47}$$

T_0, ρ_0 and c_p are respectively the temperature, the density and the heat capacity at constant pressure in the unburnt gas. E_i is the energy deposited which corresponds to 10-30% [115] of the total initial energy. This is related to the fact that due to the losses in the electric circuit, the energy transmitted is approximately 60% [23] of the electric energy available from the ignition device. Additionally, some of the energy transferred to the gas is not useful for ignition due to the formation and propagation of a shock wave. Furthermore, a large amount of this remaining energy can be lost by conduction between the electrodes and radiation losses, resulting in the deposition of only a small fraction of the initial energy. A schematic illustration is provided in Fig. 2.10.

Particular attention must be paid to the coupling between the ED

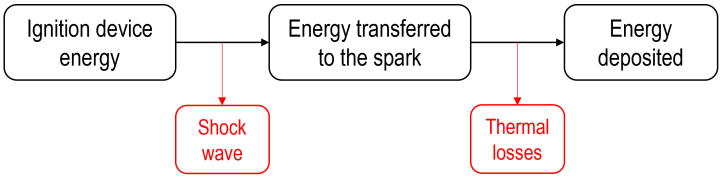

Figure 2.10: Schematic illustration of energy transfers during the spark ignition.

and the TFM model. As mentioned, the energy necessary to reach the temperature required to initiate the reactions is deposited through the ED model. If thickening is applied during the first instants, the decrease in reactivity and the increase in thermal diffusivity may result in an unphysical quenching. For this reason, thickening is only applied when the flame starts developing and the triggering occurs when the maximum value of the mass fraction of a product species equals 90% of the mass fraction at chemical equilibrium [36, 116]:

$$Y_{H_2O,max} = 90\% Y_{H_2O,eq} \tag{2.48}$$

In the present work, during the ignition simulation presented in Ch. 4 the H_2O species is selected as a control variable, as reported in Eq. 2.48. It is worth pointing out that if the condition of Eq. 2.48 is not met after a certain time, the simulation is set to start the thickening anyway to correctly simulate the flame propagation in the LES framework and to take into account the sub-grid effects on combustion.

Moreover, this approach places an additional constraint on the computational grid. In fact, during the first moments when thickening is turned off, the computational grid must be sufficient to adequately resolve the front correctly. Therefore, particular attention must be paid during the grid generation stage.

2.2 High and low order models assessment

The second part of this chapter assesses the hydrogen reaction mechanisms in terms of laminar flame speed, ignition delay time and minimum ignition energy, followed by the introduction of preferential diffusion, Soret and stretch effects. In this fashion, the Cantera Python libraries [112] are widely used to solve freely propagating and premixed counterflow laminar flames. Subsequently, in the last part, 3D laminar spherically expanding flames are simulated through DNS approach in order to test the ED model and to provide a more accurate comprehension of the influence of transport models.

2.2.1 Reaction mechanisms

Most of the reaction mechanisms discussed in this work and listed in Table 2.3, are originally developed for hydrocarbons. In the last decades, as interest in hydrogen started to increase, sub-mechanisms for hydrogen started to be developed. The reaction mechanism can be assessed at a global level, by evaluating characteristic quantities as Laminar Flame Speed (LFS) and Ignition Delay Time (IDT), or at a detailed level by considering the evolution of temperature and species. The list of tested mechanisms given in the Tab. 2.3 is not meant to be exhaustive but is intended to test the two mechanisms used within this thesis work (ELTE [113] and Boivin [117]) with two other detailed mechanisms.

	Year	**Type**	**N° species**	**N° reactions**	**Ref.**
Kéromnès	2013	Detailed	15	45	[118]
ELTE	2014	Detailed	12	28	[113]
San Diego	2016	Detailed	11	20	[119]
Boivin	2013	Skeletal	9	12	[117]

Table 2.3: Summary of the selected reaction mechanisms for hydrogen combustion.

The Kéromnès mechanism [118] is validated under typical operating conditions in gas turbines, high pressure and intermediate-high temper-

atures. As a result of an optimization, the ELTE mechanism [113] is developed and it is demonstrated that it provides an accurate description in terms of IDT and LFS, compared to other mechanisms present in the literature.

The detailed San Diego mechanism [119] is tested for both premixed and non-premixed flames. The Boivin reaction mechanism [117] is the skeletal of the San Diego and it consists of 9 species and 12 reactions.

2.2.1.1 Laminar flame speed

The laminar flame speed s_l^0 (where the index 0 indicates the unstretched condition) is defined as the velocity at which a planar, one-dimensional flame front propagates under adiabatic and stationary conditions. There are several definitions of the flame speed:

- The displacement speed s_d refers to the speed of the flame front relative to the flow. It is a local quantity that depends on the position where it is measured [78].

- The consumption speed s_c is a global quantity that refers to the rate at which reactants are consumed. It can be determined by the fuel species burning rate or by the heat release through an integration of these quantities across the flame front.

A comparison between the selected mechanisms is shown in Fig. 2.11. Results are obtained by simulating a planar, unstretched, one-dimensional, premixed, laminar flame, i.e. a freely-propagating flame, using the Cantera software. The experimental data of Egolfopoulos [120] are obtained using a twin counterflow flame. The flame speed is evaluated as a function of the stretch K and the LFS is calculated by linearly extrapolating the value when $K = 0$. The experimental data of Know [121] are achieved by employing spherical flames and considering small values for the ratio between the flame front thickness and the flame radius in order to reasonably neglect the impact of curvature. The comparison is performed at ambient temperature (T = 298 K) and pressure (p = 101325 Pa).

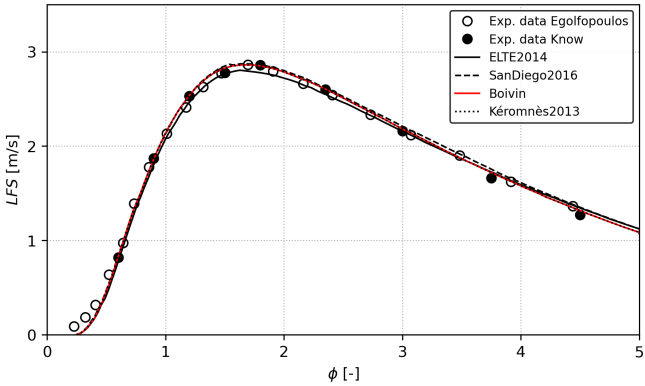

Figure 2.11: Laminar flame speed as a function of equivalence ratio for a H_2-Air mixture at 298 K and 101325 Pa.

Despite a slight underestimation on the very lean mixtures, all the selected detailed reaction mechanisms provide an excellent agreement with the experimental data as well as the Boivin mechanism which ensures an accurate prediction of the LFS across the entire range of equivalence ratios comparable to those obtained using the detailed mechanisms.

2.2.1.2 Ignition delay time

An assessment is conducted based on the ignition delay time, which refers to the time required for a mixture with a defined composition to spontaneously ignite under specified pressure and temperature conditions. The IDT is evaluated using a zero-dimensional, adiabatic, constant-volume reactor filled with a prescribed mixture. The calculation is performed with the Cantera software by monitoring the temporal evolution of the mixture. Several criteria are available in the literature to determine the IDT:

- Temperature increase [122]: the IDT is defined as the time required for the temperature of a mixture to increase by 500 K in relation to its initial temperature T_0, as shown in Fig. 2.12a.

- Maximum of temperature gradient [123]: the IDT is defined as the mean value between the two consecutive instants of time at which the maximum temperature gradient occurs. A qualitative representation is provided in Fig. 2.12a.
- Maximum of a specified species: as reported in [124], the evaluation of IDT can be performed by referring to the maximum value of the radical OH^*. Since this radical is not present in the considered mechanisms (with the exception of Kéromnès), the maximum concentration of the OH species (Fig. 2.12b) is employed for all mechanisms in order to standardize the results.

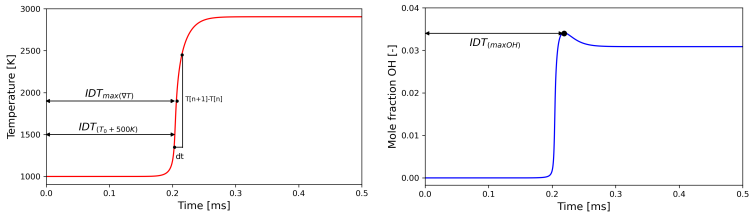

(a) Temperature criteria *(b) OH criterion*

Figure 2.12: Representation of different criteria used to estimate the IDT in terms of temperature (left) and maximum value of OH species (right).

The results obtained with the different reaction mechanisms are compared with the experimental data of Herzler [125] in Fig. 2.13 and the IDT is reported as a function of temperature for a stoichiometric hydrogen mixture at ambient pressure (91 % Ar). At lower temperatures, the three procedures provide almost the same results, while increasing the temperature evident differences appear between the maximum temperature gradient method (Fig. 2.13b) and the other two approaches based on a 500 K temperature increase (Fig. 2.13a) and maximum OH concentration (Fig. 2.13c). Indeed, only with this method, the correct prediction of IDT over the entire temperature range is retrieved in agreement with experimental data. Nevertheless, it is important to note that all investigated mechanisms provide the same trend, including the skeletal of Boivin.

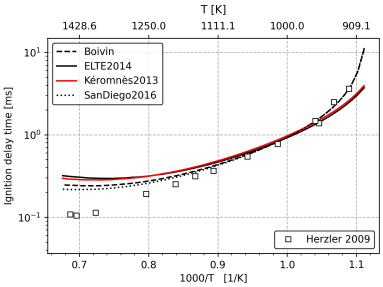

(a) Temperature increase

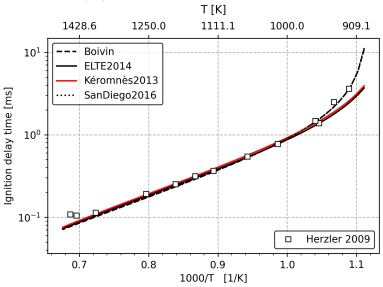

(b) Max. temperature gradient criterion

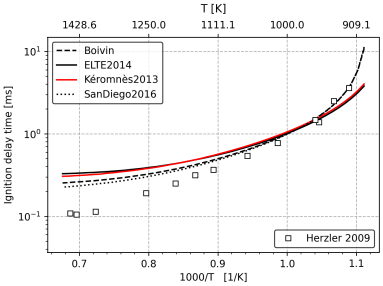

(c) Max. OH criterion

Figure 2.13: IDT as a function of temperature for a stoichiometric H_2 mixture at ambient pressure (91 % Ar).

2.2.1.3 Minimum ignition energy

As reported in Ch. 1, the minimum ignition energy is influenced by several factors, such as the mixture composition, the operating conditions and the gap between the electrodes when spark ignition is used. In [126] a model able to predict the MIE for hydrogen-air mixture in a wide range of temperatures is presented. The MIE is defined as the amount of energy required to heat up a sphere of mixture at initial temperature T_u to that of the flame T_b:

$$E_{min} = \frac{1}{6}\pi d^3 \rho_u c_{p,u}(T_b - T_u) \tag{2.49}$$

the subscript u and b are respectively referred to the unburnt and the burnt conditions. The thermophysical properties of the burnt mixture can be calculated in Cantera by imposing the chemical equilibrium at constant enthalpy and pressure in the current model. The quenching distance d is an indicator of the flame kernel diameter and in [126] it is considered to be at least twice the unstretched laminar flame thickness δ_l^0.

$$d = 2.5\delta_l^0 \tag{2.50}$$

Among the different definitions of the flame front thickness, the Blint expression [78] is used in this model (Eq. 2.51).

$$\delta_B = 2\delta \frac{\lambda_u c_{p,u}}{\lambda_b c_{p,b}} \tag{2.51}$$

where δ reads:

$$\delta = \frac{\lambda_u}{\rho_u c_{p,u} s_l^{SD}} \tag{2.52}$$

s_l^{SD} is a function of the laminar flame speed s_l^0 and a parameter X^{SD} which depends on the hydrogen concentration in order to consider the effects of preferential diffusion and stretch. Further details about its definitions are provided in [126].

The experimental data provided by Ono [127] are reported by varying the mixture composition and the gap between the electrodes in Fig. 2.14. The sudden increase of the MIE on the lean-mixtures side is attributed, as

expected, to a greater difficulty in ignition due to the limited availability of fuel.

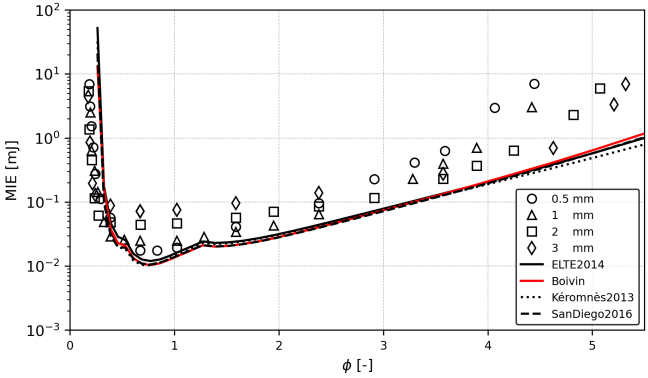

Figure 2.14: Minimum ignition energy as a function of equivalence ratio for a H_2-air mixture at 298 K and 101325 Pa for different gap distances (symbols).

The numerical results show clearly three different behaviors, depending on the equivalence ratio. These discontinuities are related to the definition of X^{SD}, which is a piecewise-defined function of equivalence ratio. Compared to the experimental data, the model provides a fairly accurate estimation of the MIE in the whole range of equivalence ratio, by recovering the correct trend observed experimentally. However, for very lean mixtures, the overestimation is probably related to the complex evaluation of the LFS near the blowout limit. Finally, there are no significant differences between the results obtained with the detailed reaction mechanisms and those obtained with the Boivin and the curves exhibit a near-identical trend.

2.2.2 Impact of transport models and stretch on 1D flames

The effect of the transport models discussed in Sec. 2.1, is now evaluated to highlight their influence on the representative quantities of the

combustion process. Fig. 2.15 provides the laminar flame speed as a function of the equivalence ratio for a hydrogen-air mixture at 298 K and 101325 Pa, by employing the three aforementioned transport models: multicomponent, mixture-average and unity-Lewis assumption. The detailed reaction mechanism ELTE is used and the Soret effect is disabled in order to evaluate only the impact of the transport model employed. The unity-Lewis assumption leads to a significant underestimation of the laminar flame speed across almost the entire range of equivalence ratios, compared to the results obtained with the mixture-average and multicomponent approach. This discrepancy is related to the fact that the effective Lewis of the mixture tends to the Lewis of the deficient species [128]. Therefore, for a lean hydrogen-air mixture where the Lewis number of the mixture tends to the one of hydrogen (approximately 0.3) the unity Lewis number assumption is not valid. The mixture-average approach instead ensures accurate and reliable results, which are perfectly comparable to those obtained using the multicomponent model.

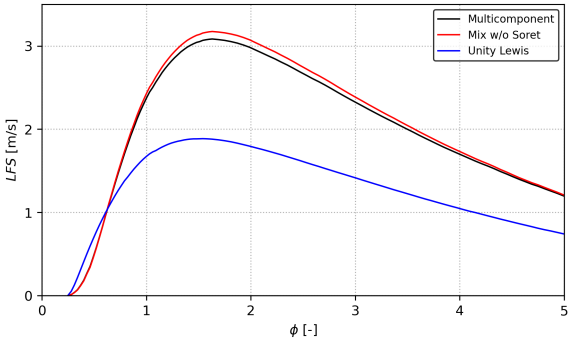

Figure 2.15: Consumption speed as a function of equivalence ratio for a H_2-air mixture at 298 K and 101325 Pa.

To better understand the influence of the transport models, the major species mole fractions, the Heat Release Rate (HRR) generated during the combustion process, the temperature and the mixture fraction Z profiles are reported in Fig. 2.16 for a selected equivalence ratio. The effect of

preferential diffusion can be appreciated from the species distribution: hydrogen diffuses with a higher velocity and consequently, the mixture upstream of the flame front becomes leaner, leading to a redistribution of oxygen. This results in lower HRR, concentration of H_2O and final temperature than those predicted with the unity-Lewis hypothesis. The effect is evident in the plot concerning the mixture fraction: it decreases at the flame front, indicating the leaning of the mixture. As reported in

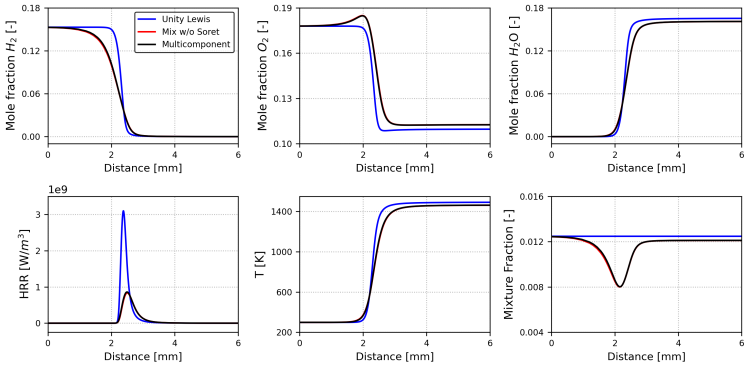

Figure 2.16: Effect of transport models on species mole fraction, heat release rate, temperature and mixture fraction for a H_2-air mixture at 298 K, 101325 Pa and ϕ=0.43.

Sec. 2.1, it is important to point out the effects of the thermal diffusion of lighter species, such as hydrogen. Fig. 2.17 shows the results obtained by resolving a freely-propagating flame at 298 K, 101325 Pa and ϕ=0.43 with a detailed reaction mechanism and the multicomponent approach. It is possible to notice that the hydrogen diffusion is enhanced by the Soret effect (dashed line). As a consequence, the unburnt mixture becomes leaner, resulting in a lower flame temperature and heat release rate, amplifying the preferential diffusion effect. However, in a simplified case as a freely-propagating flame, the global influence of thermal diffusion on the development of the flame is limited and negligible compared to that of preferential diffusion and this is related to the conservative nature of

this type of flame [77]. Conversely, as demonstrated in Sec. 2.2.3, when spherical flames are simulated, an increase in HRR and temperature is observed.

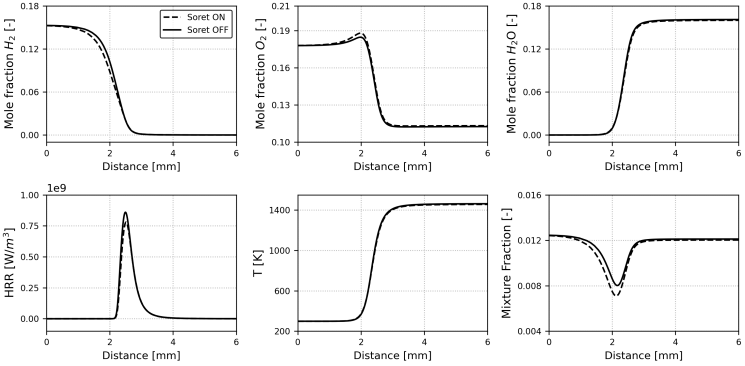

Figure 2.17: Impact of Soret effect on species mole fraction, heat release, temperature and mixture fraction for a H_2-air mixture at 298 K, 101325 Pa and ϕ=0.43.

The utilization of one-dimensional freely propagating flames is a useful tool to explain fundamental concepts, however, they are not representative of practical applications. The previous evaluations do not consider the three-dimensional nature of the flow field and the implications on the development of the flame. In fact, a non-uniform flow leads to a stretch action on the flame surface, quantified as the variation of the flame surface:

$$K = \frac{1}{A}\frac{DA}{Dt} \tag{2.53}$$

where A is the flame surface. The material derivative D/Dt determines a non-stationary contribution due to the curvature and a stationary term related to the 3D development of the flame front, referred to as strain. Therefore, the stretch can be expressed as

$$K = \kappa + s_c\left(\frac{1}{R}\right) \tag{2.54}$$

where R is the curvature radius and κ is the strain rate. The flame stretch action leads to a reduction in the flame front thickness that determines, as reported in Fig. 2.18:

- an increase in the temperature gradient, which implies a higher cooling effect caused by the tendency of the heat to diffuse towards regions characterized by lower temperatures.

- an increase in the species concentration gradient, which enhances the renewal of fresh mixture.

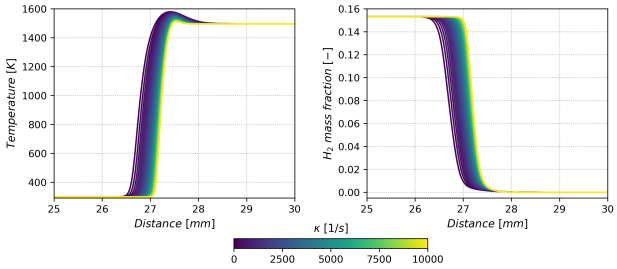

Figure 2.18: Temperature (left) and hydrogen mass fraction (right) profiles in the physical space, colored by strain rate, obtained by resolving several premixed counterflow flames at 298 K, 101325 Pa and ϕ=0.43.

The resulting effects on the consumption speed are in contrast and the overall behavior of the flame is strictly connected to the Lewis number of the fuel Le_F [78]. If $Le_F = 1$ (Fig. 2.19a), heat and species diffuse in the same way, therefore, for low stretch values, the effect on the consumption speed is compensated and it remains approximately constant.

As the stretch increases, the cooling effect causes a decrease in temperature and consumption speed until the flame blow-off. Conversely, the cooling effect dominates if $Le_F > 1$ (Fig. 2.19c) and as the stretch increases, the consumption speed decreases, reaching a critical value and causing the flame to extinguish. If $Le_F < 1$ (Fig. 2.19b), as observed in the case of hydrogen, the consumption speed initially tends to increase

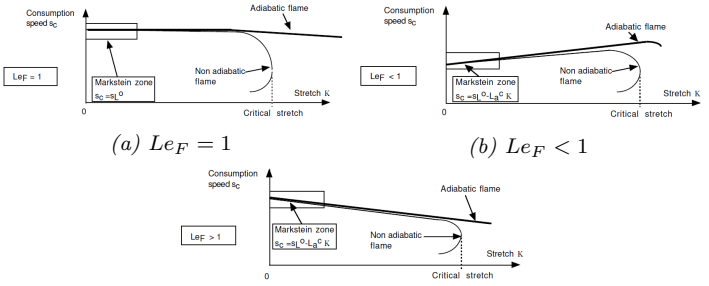

(a) $Le_F = 1$ (b) $Le_F < 1$

(c) $Le_F > 1$

Figure 2.19: Effect of stretch on the consumption speed for a mixture with a Lewis number equal (a), lower (b) and higher than one (c) [78].

due to a lower heat dispersion and a greater supply of fresh mixture at the flame front.

To evaluate the effect of the strain, the premixed counterflow flames in the fresh-to-burnt configuration available in Cantera are used. This configuration can reasonably be considered one-dimensional, given the predominant direction of flow. The strain can be modified by varying the inlet velocity or the distance between the two jets. The significant influence of the transport models and the impact of the strain is illustrated in Fig. 2.20. The multicomponent and the mixture-average approach provide the same results and, as previously mentioned, it is possible to observe the initial increasing trend of the consumption speed. Conversely, the hypothesis of unity-Lewis predicts only a decreasing trend that is not consistent with what is expected for a lean hydrogen-air mixture.

It is also essential to evaluate the impact of the curvature on the development of the flame. Numerous attempts [129, 130] are made to isolate the curvature effect from that of stretch, demonstrating that curvature has a significant impact on the consumption speed. When the surface of the flame front increases, due to the curvature, on the side of the fresh mixture (burnt mixture), it refers to positive (negative) curvature. The overall effect on the consumption speed depends again on the Lewis number. Particularly, for a lean hydrogen-air mixture ($Le_F < 1$), if the

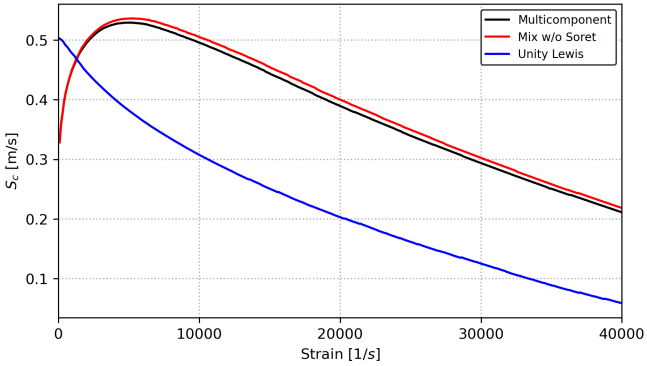

Figure 2.20: Effect of transport models and strain on the consumption speed for a H_2-air mixture at 298 K, 101325 Pa and ϕ=0.43.

curvature is positive, species diffuse towards the burnt mixture increasing temperature and leading to an increase in s_c. Conversely, if the curvature is negative, the opposite effect is obtained since the species diffuse in a large region causing a decrease in s_c. This condition is unstable as the flame front wrinkling tends to increase [78] and it can lead to the so-called thermo-diffusive instabilities [131, 132], represented in Fig. 2.21a. Under similar considerations, the situation is reversed for a rich hydrogen-air mixture ($Le_F > 1$) due to the higher heat diffusivity: the flame front wrinkling tends to decrease and the condition is stable. It can be concluded that the Lewis number, and thus the preferential diffusion, influence significantly the impact that curvature has on the consumption speed [130].

2.2.3 Influence of transport models on ignition phase

In this section, a preliminary study to evaluate the influence of preferential and thermal diffusion on the early stages of the ignition sequence is presented. A 3D laminar spherical expanding flame is simulated in ANSYS Fluent® and it is analyzed with the dual purpose of testing the Energy Deposition model and directly evaluating the influence of preferential and

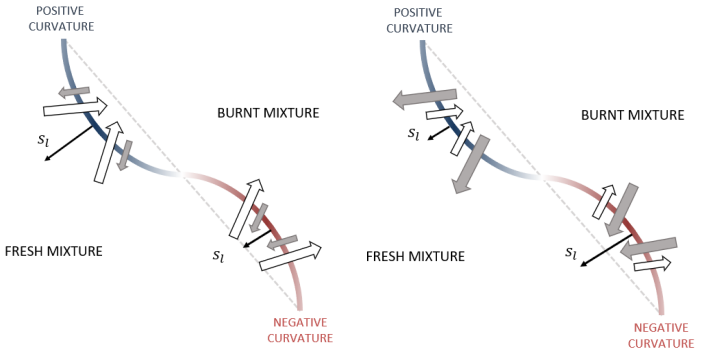

(a) Unstable regime ($Le_F < 1$) *(b) Stable regime $Le_F > 1$*

Figure 2.21: Sketch of the curvature effect on the consumption speed, adapted from [78] for $Le_F < 1$ (a) and $Le_F > 1$ (b). Species diffusion: empty arrow. Heat diffusion: filled arrow.

thermal diffusion on the early stages of the ignition sequence. The domain is a sphere with a radius R and the computational grid consists of 12.4 million of polyhedral elements with different levels of refinement, as shown in Fig. 2.22. In particular, the inner part within ten times the spark radius R_{spark}, has a sizing of 20 µm that allows to discretize the flame front with at least 15 points (for the operating conditions considered). The intermediate refinement is required to ensure a smooth transition between the fine and the external coarse grid. In fact, this last part placed sufficiently far from the region of interest, is characterized by a dimension of 5 mm which allows to reduce the computational cost and dump the pressure waves generated during ignition. A summary of the refinement zones with their relative sizing is reported in Tab. 2.4.

	Sizing
$R < 10\,R_{spark}$	20 µm
$10\,R_{spark} < R < 20\,R_{spark}$	50 µm
$20\,R_{spark} < R < 200\,R_{spark}$	5 mm

Table 2.4: Element sizing in the refinement zones.

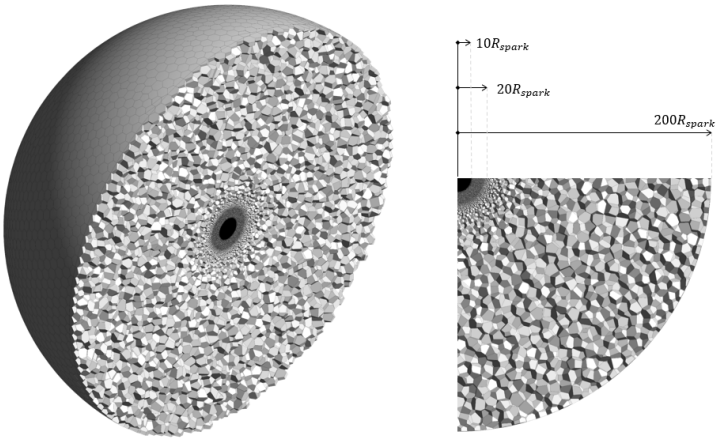

Figure 2.22: Section views of the computation grid employed for the spherical ignition simulations with a schematic representation of the refinement zones extension.

DNS are performed with the pressure-base solver, the Coupled algorithm for the pressure-velocity coupling and a constant time step of $1 \cdot 10^{-7}$ s. The simulations are conducted for a physical time until the spherical flame propagates for a distance approximately 8 times the spark radius. This ensures that the flame remains confined within the internal refinement region which guarantees a correct discretization. It is important to underline that cellular instabilities are not observed, as shown below, since the critical radius [133] is not reached to limit computational efforts because the study of these effects is beyond the scope of this part. Regarding the boundary conditions, the atmospheric pressure is prescribed at the outlet patch. Initially, the domain is filled with a homogeneous hydrogen-air mixture at 298 K characterized by an equivalence ratio of 0.43. Ignition occurs at the center of the sphere using the ED model. The spark has a characteristic radius R_{spark} of 250 µm, a duration t_{spark} of 80 µs and the energy deposited is 0.025 mJ. The Boivin mechanism is employed to describe the system reactivity. A preliminary 1D freely-propagating flame, as described in Sec. 2.1.3.3, is conducted under the same conditions

in terms of time step ($1 \cdot 10^{-7}$ s), grid resolution (20 µm) and boundary conditions (ϕ=0.43, p = p_{atm}, T = 298 K). The results, shown in Fig. 2.23 and represented by the solid line, are compared with those obtained with a freely propagating flame performed in Cantera. An excellent agreement in terms of species concentration, HRR and temperature evolution is retrieved allowing the setup employed to be verified.

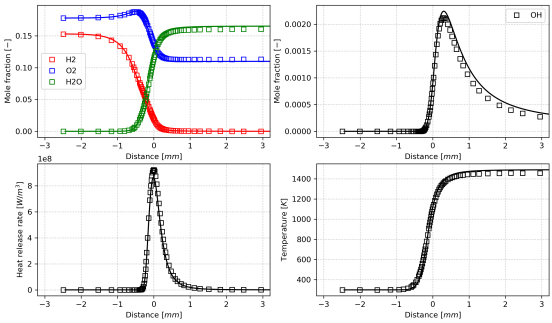

Figure 2.23: Comparison of the results obtained with Fluent and the 1D flame in Cantera in terms of species concentration, HRR and temperature.

Four different simulations (named S1, S2, S3 and S4) are conducted by using the same operating conditions, equivalence ratio, computational grid and time step. However, the transport model is modified in order to investigate the influence of preferential diffusion and Soret effect on the early stages of the ignition dynamic. A summary of the simulations is provided in Table 2.5.

During the simulations, the maximum temperature is monitored in order to verify the correct functioning of the ED model and, as shown in Fig. 2.24a, it does not exceed 3000 K regardless of the transport model employed. However, as previously mentioned, these approaches affect the evolution of the combustion process and this is evidenced by the fact that when the reactions occur, due to different distributions in

	S1	S2	S3	S4
Multicomponent	✓			
Mixture-average		✓		✓
unity-Lewis			✓	
Soret effect				✓

Table 2.5: Summary of the DNS performed with their relative transport models.

species concentration, the flames reach different temperatures and power levels (Fig. 2.24b). To better analyze the differences between the various approaches it is useful to refer to Fig. 2.25 and Fig. 2.26 which provide the contours of the equivalence ratio ϕ and the HRR with the purpose of representing the curved flame front in a straight configuration.

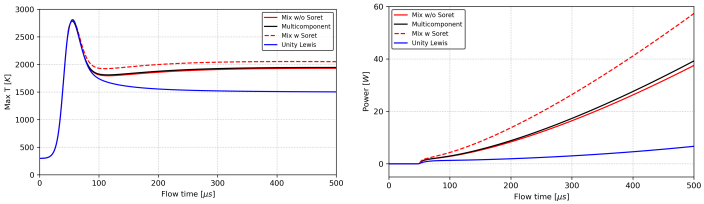

(a) Maximum temperature *(b) Thermal power*

Figure 2.24: Time evolution of maximum temperature (left) and power (right) using different transport models

The plots on the right side show the trend of the mentioned quantities as a function of the propagation distance L normalized with the spark radius R_{spark}. It is important to underline that the equivalence ratio is evaluated using Bilger's formulation [98], which is based on the elemental mass fraction.

With the unity-Lewis assumption, preferential diffusion effects are ignored and the perfectly premixed mixture exhibits a constant equivalence ratio, equal to the nominal one, in the entire domain. Contrarily, with the multicomponent it is possible to observe a decrease in the equivalence ratio on the fresh mixture side due to the high diffusivity of hydrogen.

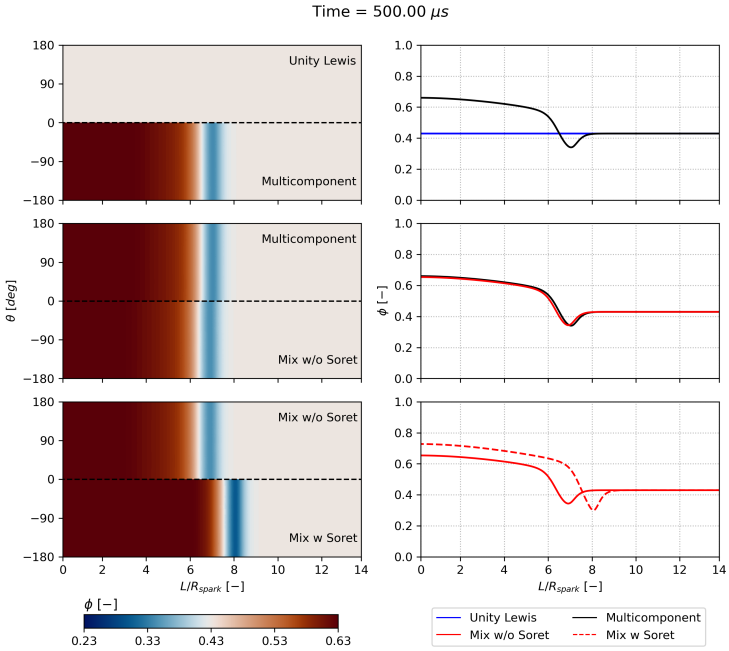

Figure 2.25: Contours of equivalence ratio (left) and its trend over the black dashed line as a function of propagation distance (right) using different transport models.

Furthermore, as a consequence of the positive curvature, a greater amount of reactants at the flame front leads to an increase in HRR. This is related both to the rise in temperature, which affects the propagation speed, and to the effect that stretch has on a mixture with a Lewis number lower than one. The result is that at the same instant, the HRR peak obtained with the multicomponent is shifted towards higher L/R_{spark} compared to the one retrieved with the unity-Lewis assumption, indicating a greater flame propagation speed. The results of the mixture-averaged approach are consistent and comparable with those obtained with the multicomponent and thus it is selected to investigate the role of the Soret effect.

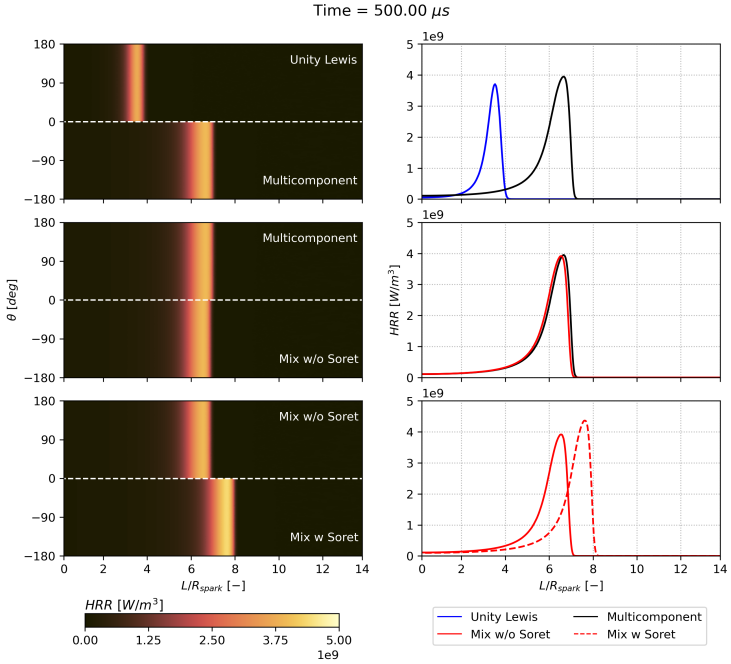

Figure 2.26: Contours of HRR (left) and its trend over the white dashed line as a function of propagation distance (right) using different transport models.

Thermal diffusion amplifies the preferential diffusion and stretch effects as it involves the diffusion of the lighter radicals H_2 and H towards the center of the spark where the temperature is higher. This results in a richer mixture and, therefore, in a further increase in the HRR.

As previously explained, the Soret effect involves a mass diffusion caused by a temperature gradient. The comprehension of this phenomenon can be enhanced by analyzing Fig. 2.27, in which the equivalence ratio, the HRR and the temperature are shown as functions of the L/R_{spark} ratio and τ i.e. the time normalized with the duration of the spark $\tau = t/t_{spark}$.

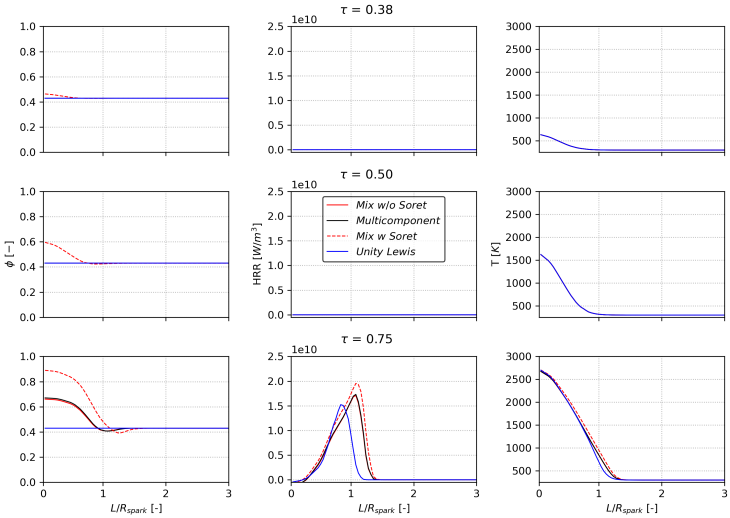

Figure 2.27: Equivalence ratio, heat release rate and temperature as functions of physical space and time using different transport models.

It is possible to notice that for $\tau = 0.38$, the temperature rise induced by the spark involves, when the Soret is enabled, the migration of hydrogen towards the center of the spark, resulting in a rise of ϕ in this region. The reactions are not triggered, as evidenced by the fact that the HRR is zero. At $\tau = 0.5$, the aforementioned effect is amplified due to the further

increase in temperature and ϕ reaches a value of 0.6. This implies that until reactions occur, only the model involving thermal diffusion exhibits a change in ϕ. Conversely, the phenomenon of preferential diffusion is relevant when the combustion begins to progress ($\tau > 0.65$) resulting in a concentration gradient that determines the species diffusion towards the flame front and a significant variation of ϕ.

2.3 Final considerations

This chapter summarises the basic equations underlying computational fluid dynamics in the LES framework, with a brief reminder of the fundamental concepts of turbulent combustion and related modeling.

It is noted how the different properties of hydrogen compared to conventional fuels play a key role in the combustion dynamics. In particular, for lean hydrogen-air mixtures, the inclusion of such effects in CFD modeling is mandatory, and in this context, the primitive variable approach through a Thickened Flame Model is an excellent compromise between accuracy and computational cost. Indeed, due to the 'less complex' chemical kinetics of hydrogen compared to a generic hydrocarbon, it allows the use of accurate reaction mechanisms with a low number of species. At the same time, a mixture-averaged approach to calculate diffusive fluxes is almost equivalent to a more generic and costly multicomponent approach. In this case, it is also observed how Soret effects influence the flame propagation speed, right from the first moments immediately after ignition of the mixture.

Finally, a cost-efficient extension of the original model is presented to account for the effects of stretch and heat loss in a tabulated chemistry framework. It should be underlined that this approach is not intended to resolve preferential diffusion effects directly, but to model their effects through a case-independent parameter that can be calculated a-priori once the operating conditions are defined. This model is first validated by comparing the results obtained in the laminar regime with a reference solution obtained through Cantera software. It can be seen that, compared

to the original model, there is an improvement in the agreement with the reference data.

Chapter 3

TU Berlin combustor model

In this chapter, the numerical campaign carried out on a lean, swirl-stabilized, technically premixed hydrogen flame experimentally investigated at the Technische Universität Berlin (TUB) is presented. The current rig constitutes one of the few burners available in the literature representative of aero engine combustors operating with full hydrogen flame. Indeed, the moderate thermal power at which the rig can operate coupled with the detailed measurements available in both non-reactive and reactive conditions including NO_x make it of great scientific interest.

The main purpose behind this architecture is to investigate the resistance at flashback under different operating conditions. In detail, the key aspect of the rig is a pure axial air injection characterized by a high momentum aiming to change the stabilization position of the flame and consequently avoid the flashback scenario. Moreover, different mass flow rates, air preheating and equivalence ratio are experimentally tested showing a strong impact on the flame dynamic as well.

The test case is previously investigated by other authors using similar methods but considering different operating conditions. In particular, Mira et al. [134, 135] demonstrated the ability of the FGM approach under perfectly premixed conditions to correctly capture the fuel momentum influence on the stabilization mechanism. Recently, Capurso et al. [82]

studied through a conditioned TFM the influence of the wall temperature in NO_x emission introducing a new reaction mechanism that directly includes the NO_x chemistry.

The aim of this first activity is to extensively study the TUB rig with all the numerical models introduced in Sec. 2.1.3 to handle the turbulence chemistry interaction in order to validate the numerical setup through high-fidelity Large Eddy Simulations. Therefore, the first point that is accounted for is the assessment of the current industry-standard models present in the literature, the FGM and the TFM respectively. After that, the extension model of FGM (E-FGM) to include the effects of stretch and heat loss in the reactivity is analyzed. Moreover, the influence of the number of points used to discretize the flame thickness as well as the impact of the thermal boundary conditions are investigated. Finally, in light of the results that emerged, the most accurate numerical setup is defined taking into account the relative computational cost to model a lean hydrogen flame that is later used in the second case study presented in this thesis.

This chapter is organized as follows, in the first part, a detailed description of the investigated test case is provided highlighting the main differences in the considered test point with respect to the previous cited works. Then, the numerical strategy employed in the CFD simulations is presented pointing out the key aspects of the models used. Finally, a detailed comparison with the available experimental data of the results obtained with the three approaches is shown.

It is worth remarking that, to the authors' knowledge, the present study represents the first work on the selected operating conditions in which both FGM and TFM are tested under technically premixed conditions.

3.1 Investigated experimental rig

The rig under investigation is the burner developed during the *Advanced Hybrid Engines for Aircraft Development* (AHEAD) project by TUB [11, 59, 136] shown in Fig. 3.1. The quartz combustion chamber has

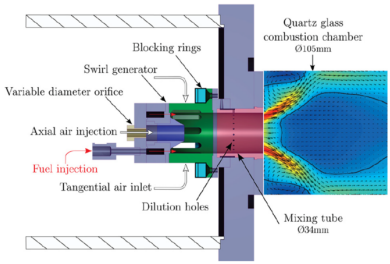

Figure 3.1: Experimental TUB rig under investigation [59].

an internal diameter of 105 mm with an axial extension of 297 mm, and it is fed through a mixing tube in which air and fuel mix together reaching technically premixed conditions. The axial length of the premixing region is a degree of freedom that is experimentally investigated. The fuel is injected through sixteen holes placed at the bottom of the mixing tube which are fed by a dedicated fuel plenum. Instead, the primary air mass flow rate is supplied with two distinct ports. The first one is a modular swirler in which the amount of mass flow and consequently the swirler component imposed at the flow can be adjusted by adding or removing blocking rings. The second port is a pure axial injection characterized by a high momentum aiming to prevent flashback risk. Different axial orifice diameters (d_{ax}) are experimentally tested in order to investigate the impact on the stabilization mechanism. Finally, a small amount of air (less than the 3 % of the total air mass flow rate) is injected through 22 holes placed in the middle of the mixing tube in order to generate a lean mixture near the wall to prevent the flashback risk coming from the wall boundary layer. The flow split between the two main air inlets is designed by introducing the parameter χ, defined as:

$$\chi = \frac{\dot{V}_{ax}}{\dot{V}_{ax} + \dot{V}_{sw}} \tag{3.1}$$

in which $\dot{V}$ represents the volumetric mass flow in the axial (ax) and swirler (sw) port respectively.

In the present work, the long mixing tube (60 mm) configuration with the maximum axial momentum is analyzed. The axial orifice diameter is equal to $d_{ax} = 8.8$ mm and two blocking rings with 7 mm blockage height of the swirling ports are used providing a theoretical swirl number of 0.9. The two rings have a height of 7 and 4 mm respectively. The flow split parameter χ assumes its maximum value $\chi = \chi_{max}$ but, unfortunately, detailed measurements of such value are not available. This feature of the rig distinguishes this configuration from the previous ones already numerically studied. The average bulk velocity in the mixing tube is estimated to be 70 $m.s^{-1}$. The chamber operates under atmospheric conditions with a nominal equivalence ratio of $\phi = 0.6$ which corresponds to a thermal power of 76 kW. The air and fuel are preheated at 623.15 K and 352.15 K respectively. A constant air mass flow rate of 130 $kg.h^{-1}$ is injected through the air plenum. A summary of the operating conditions considered in this work is reported in Tab. 3.1. Under this configuration, according to the stability limits reported in [59], the rig operates in stable conditions far from the flashback limit.

Operating conditions	
Operating pressure	101325 Pa
Thermal power	76 kW
Fuel	100 % H_2
Mixture	Technically premixed
Equivalence ratio	0.6
Inlet air temperature	623.15 K
Air mass flow rate	130 $kg.h^{-1}$
Inlet fuel temperature	352.15 K
Fuel mass flow rate	2.28 $kg.h^{-1}$

Table 3.1: Summary of the operating conditions considered in this work.

Regarding the experimental diagnostic, detailed optical measurements are available for both non-reactive and reactive conditions. In particular, *High-Speed Particle Image Velocimetry* (HS-PIV) is used to measure the velocity under both operating conditions instead, *Planar Laser Induced Fluorescence of OH* (OH-PLIF) is adopted to identify the flame anchoring

point and establish the flame structure in reactive tests. A sketch of the experimental facility is reported in Fig. 3.2. The readers interested in more detailed information about the experimental diagnostic and rig are referred to [11, 59].

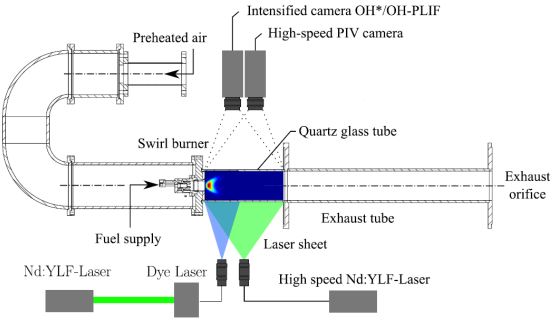

Figure 3.2: Experimental setup for both HS-PIV and OH-PLIF measurements [11].

3.2 Setup of the simulations

Regarding the numerical modeling, the commercial pressure-based software ANSYS Fluent® 2019R3 is used for all the simulations presented in this chapter in the unsteady high-fidelity LES framework. Due to the large number of non-reactive and reactive simulations carried out in this numerical campaign, a summary of the computational cases is reported in Tab. 3.2. A deep explanation of the setup used in each of them is provided in the following part of this chapter.

3.2.1 Computational domain and numerical grids

The computational domain, reported in Fig. 3.3, is discretized starting from the air plenum up to the outlet section including the swirler, the fuel plenum, and all the other features described in the previous section. The black plane shown represents the post-process longitudinal section in

Test matrix					
Name	**Conditions**	**Mesh**	**Thermal BCs**	**Soret**	N^{TFM}
M-A	Non-Reactive	MESH-A	Adiabatic	-	-
M-B	Non-Reactive	MESH-B	Adiabatic	-	-
FGM	Reactive	MESH-B	Adiabatic	-	-
E-FGM	Reactive	MESH-B	Adiabatic	-	-
TFM	Reactive	MESH-B	Adiabatic	×	5
N-TFM	Reactive	MESH-B	Adiabatic	×	10
T-TFM	Reactive	MESH-B	Temperature	✓	5

Table 3.2: Summary of the TUB simulations with the main setup employed.

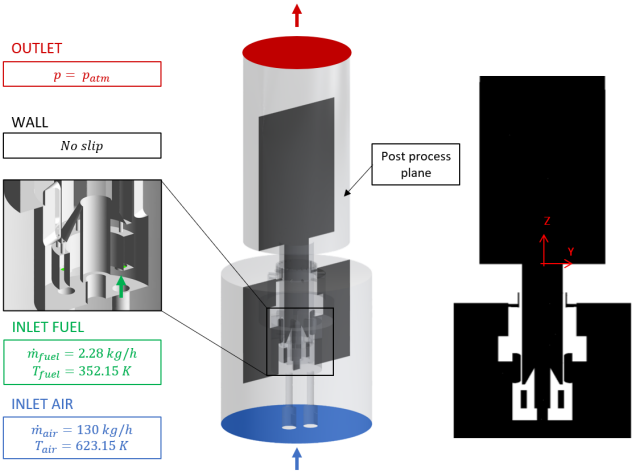

Figure 3.3: Computational domain with the prescribed boundary conditions.

which the contours are reported in the results section. The origin of the reference frame is set at the exit of the mixing tube with the *z-coordinate* aligned with the axis of the burner. For the sake of clarity, a positive value of *z-coordinate* indicates regions inside the combustion chamber, while negative values indicate regions inside the mixing tube.

The complete domain is discretized in two hybrid polyhedral meshes with different levels of refinements in order to assess the impact of the spatial resolution through a mesh sensitivity carried out in the non-reactive conditions, as discussed in the dedicated section. A sketch of the meshes is shown in Fig. 3.4 with their relative size reported in the bottom table. Starting with the coarser mesh (named MESH-A in the following) that counts roughly 16M of elements, several ad-hoc refinements are performed in the domain to obtain the refined one (MESH-B). In particular, due to the high velocity at the exit of the axial jet, a fine grid up to 100 µm is used in this region to better capture its penetration and interaction with the swirling jets. In both cases, the mixing tube and the swirler as well as the reaction zone are kept at a minimum sizing of 450 µm that corresponds to the unstretched flame thermal thickness at the nominal equivalence ratio $\delta_{th}(\phi = 0.6)$.

3.2.2 Boundary conditions

A sketch of the prescribed boundary condition is also reported in Fig. 3.3. For all the simulations, a constant mass flow rate of air is imposed at the air inlet patch, whereas constant atmospheric pressure is set at the outlet. In addition, for the reactive simulations, a constant mass flow rate of hydrogen is set at the fuel plenum inlet according to the selected test point. For the sake of clarity, in the two cold cases, only air is injected into the domain. All the other surfaces are representative of solid walls, so the no-slip condition is imposed. Regarding the thermal boundary, in the first stage of the work, the walls are treated as adiabatic. Then, in the last simulation of this study, in order to investigate the effect of heat loss on the flame dynamic and anchoring process, a constant temperature distribution is prescribed at the combustion chamber, back

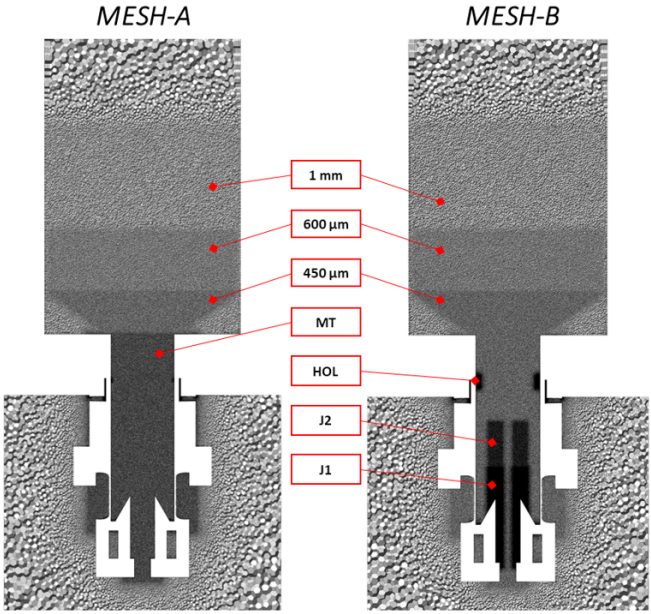

Label	MESH-A (16M)	MESH-B (29M)
Global	5 mm	5 mm
MT	300 µm	450 µm
J2	-	200 µm
J1	-	100 µm
HOL	-	100 µm

Figure 3.4: Computational meshes with relative sizes.

plate and mixing tube walls. Since no experimental data are available on the thermal boundary conditions and due to the high computational cost of a Conjugate Heat Transfer (CHT) analysis, the temperature distributions are estimated from a previous work [82] where a full CHT simulation is carried out. Due to the different operating conditions, the temperature levels are scaled according to the adiabatic flame temperature or the cold mixing temperature in perfectly premixed conditions. In particular, for the combustion chamber walls directly exposed to the flame, the temperatures are scaled according to the following formula:

$$\frac{T_{ad}(\phi_{nom})}{T_{ad}^{[82]}(\phi_{nom})} = \frac{T_{wall}}{T_{wall}^{[82]}} \tag{3.2}$$

in which T_{ad} represents the adiabatic flame temperature at the nominal equivalence ratio. Instead, on the other surfaces that are not directly in contact with the reaction zones, the temperatures are scaled using the perfectly premixed temperature in cold conditions (T_{mix}):

$$\frac{T_{mix}(\phi_{nom})}{T_{mix}^{[82]}(\phi_{nom})} = \frac{T_{wall}}{T_{wall}^{[82]}} \tag{3.3}$$

A sketch of the prescribed temperature distribution is reported in Fig. 3.5. It is important to highlight that, within the mixing tube, from about the middle where fuel and air are not well mixed, the temperature is consistently set to a fixed value T_{air} to approximately assign local adiabatic conditions. Simultaneously, downstream of the zone where the flame fluctuates inside the combustion chamber, the temperature is maintained at a constant value, specifically at the maximum value retrieved. These two axial positions are taken from a previous average solution of the TFM simulation carried out in the adiabatic conditions.

3.2.3 Numerical modelling

In the current study, as previously pointed out in Tab 3.2, seven LES calculations are carried out in order to analyze the impact of the

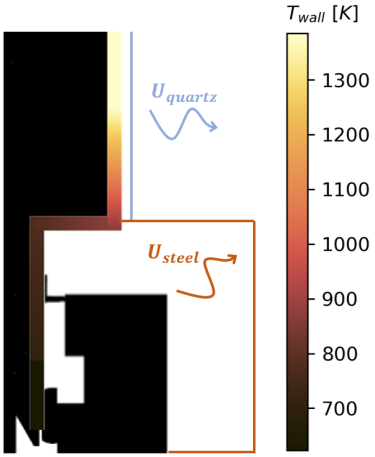

Figure 3.5: Wall temperature profiles for the non-adiabatic simulation (T-TFM).

mesh resolution in non-reactive conditions and the turbulence combustion modeling in the reactive one.

In all of them, the effect of unresolved eddies is modeled using the Dynamic Smogorinsky-Lilly formulation which dynamically evaluates the Smagorinsky constant [89]. For the cold simulations, no further models are required since only air is considered. On the contrary, for the reactive simulations, an additional model is necessary to handle the turbulent combustion.

In the first simulation with the tabulated chemistry approach, the baseline FGM approach introduced in Sec. 2.1.3.2 with two control variables (mixture fraction Z and progress variable c) is used to account for the turbulence-chemistry interaction. The un-normalized progress variable is defined as $Y_c = Y_{H_2O} - Y_{H_2}$. The choice of this definition comes from 1D laminar flame analysis conducted with Cantera v2.4.0 Python libraries [112] on premixed freely propagating flames, as shown in Fig. 3.6 in which a comparison of three progress variable definitions is performed using the

multicomponent transport approach and ELTE mechanism.

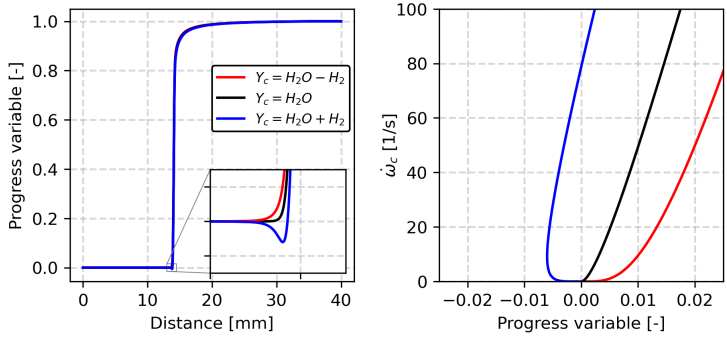

Figure 3.6: Assessment of progress variable definition. Premixed freely propagating flames at $p = p_{atm}$, T=570 K and ϕ = 0.6.

Starting from the black curve, a common definition of the PV based only on the product (H_2O) is used. It is possible to see in the progress variable space (right plot) how the reactivity starts immediately with a small gradient of the PV. Therefore, to better discretize the ignition of the mixture, it is mandatory to include also the hydrogen mass fraction on the PV definition due to the high mass diffusivity of the H_2 molecule which spread upstream of the flame front [81]. Two different formulations are tested in which only the red one met the requirements of an increasing monotic function. This definition ($Y_c = Y_{H_2O} - Y_{H_2}$) allows to properly discretize the first ignition phase providing an approximately zero reactivity for a value close to zero for the PV. At the same time, in the physical space (left plot), a smooth increase can be pointed out with respect to the black curve.

For the laminar look-up table generation, several freely propagating premixed flamelets at various equivalence ratios are calculated using the detailed ELTE reaction mechanism [113] with the full multicomponent approach. The temperature, progress variable source term, OH and H_2O mass fraction extracted from the laminar table are reported in Fig. 3.7. Since no modifications are made to the model, the non-unity Lewis number

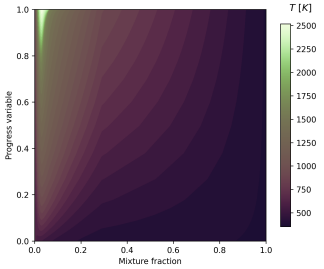

(a) Temperature

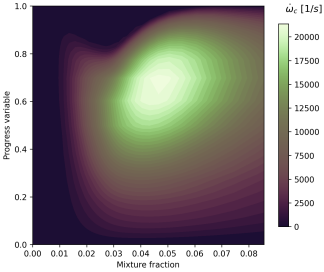

(b) PV source term

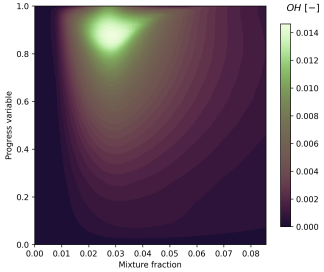

(c) OH mass fraction

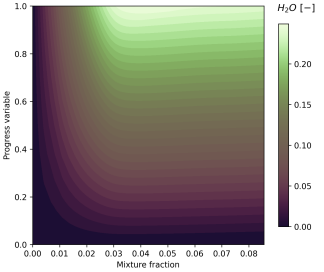

(d) H2O mass fraction

Figure 3.7: Contours of temperature (a), progress variable source term (b), OH mass fraction (c) and H2O mass fraction (d) extracted from the table as a function of the two control variables.

effects are not accounted for within this strategy.

To overcome this deficiency with a tabulated chemistry approach, the E-FGM previously introduced in Sec. 2.1.3.3 is used. In the present work, the Cantera libraries are used to generate the Gamma table by solving several freely propagating ($\kappa = 0$ s^{-1}) and premixed counterflow flames ($\kappa >0$ s^{-1}) employing the same mechanism. The final Γ table is shown in Fig. 3.8 in the mixture fraction-strain rate space for the adiabatic conditions ($\psi = 1$).

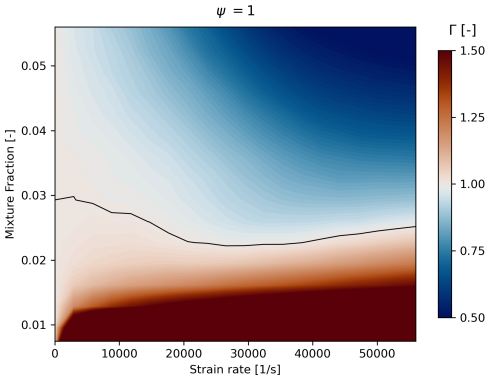

Figure 3.8: Gamma table in mixture fraction and strain rate space for adiabatic conditions ($\psi = 1$). Isoline of $\Gamma = 1$ is also superimposed.

For hydrogen flames, it is mandatory to recall that the maximum of the strained source term ($\dot{\omega}_c(Z, c, \psi, k)$) shows two different behaviors depending on the mixture properties. From one side, lean mixtures are characterized by a Le number which tends to the Le_{H_2} since it represents the deficient species. This causes an increase of the max strained source term when the strain rate increases due to the preferential diffusion effects. On the other side, rich mixtures exhibit the opposite behavior since the Le number tends to the one of oxygen which is slightly higher than one [81]. Therefore, depending on the conditions at which combustion takes place, there can be either an increase or decrease in reactivity, in which the

intensity depends on how far it is from stoichiometric conditions (black isoline in Fig. 3.8) and the strain rate values.

Regarding the last three reactive simulations carried out with the species transport approach, the skeletal mechanism obtained by Boivin [137] (9 species with 12 reactions) is used to describe the system reactivity through the Arrhenius type chemical kinetics modeling. To account for the numerical stiffness shown by the chemical species transport equations, a dedicated stiff chemistry solver is used to decouple the chemical integration time step from the one adopted by the main solver [138]. The turbulence chemistry interaction is handled with the TFM in which the thickening is locally applied only in a narrow band of the flame front thanks to a sensor factor Ω, based on the first reaction, and the sub-scale wrinkling effects are modeled with the Colin [91] efficiency function E (β=0.33). The laminar flame thickness δ_{th} and speed s_l necessary as input of the model are computed in a priori stage with Cantera. Due to the use of a skeletal reaction mechanism, a sensitivity to the points (N^{TFM}) used to discretize the thermal thickness is also performed. Specifically, it is simulated with fewer (5) and higher (10) points than the recommended number for a skeletal mechanism [139] which corresponds to a maximum thickening factor below 10 and 20 respectively. A mixture-average approach is adopted to evaluate the mass and thermal diffusivity according to the kinetic theory [138] while the Soret effect is accounted for only in the simulation with the non-adiabatic boundary conditions (see again Tab. 3.2). In this case indeed, since all the temperature gradients are enhanced by the fixed wall temperature, the Soret effect could play an important role.

Finally, the SIMPLEC algorithm is adopted for the pressure-velocity coupling with a constant time step of $1 \cdot 10^{-06}$ s which ensures a convective Courant number below 10 in the zones of interest. Second-order schemes are used in both space and time using an implicit formulation for this last one.

3.3 Results

In this section, the main outcomes of the numerical investigation carried out on the TUB test case are presented. As anticipated, in the first part a LES mesh sensitivity analysis is discussed for the non-reactive conditions pointing out the main characteristics of the cold flow field. With this approach, an appropriate mesh able to describe the flow field is defined. This grid is subsequently used in the following reactive simulations.

Then, a detailed analysis of reactive results obtained with the FGM and TFM models is presented highlighting the main differences between the two baseline simulations. Starting from that, further analysis performed with the extended version of the FGM to account for the stretch effects as well as the sensitivity at the number of points (N^{TFM}) and thermal boundary conditions are introduced and compared with the previous baseline cases.

The reactive results first focus on the flow field structure considering the main parameters under which the rig operates (pressure drop and flow split). After that, the mixing process that takes place inside the mixing tube is analyzed and finally, the flame shape is compared with the experimental data. Before remarking on the main conclusions of this investigation, an estimation of the computational cost of the two models (FGM and TFM) for the case considered is also provided.

3.3.1 Mesh sensitivity analysis

In this part, a mesh sensitivity is presented for the non-reactive conditions carried out within an LES approach onto the two meshes presented in Fig. 3.4.

A full comparison with the experimental data in terms of time-averaged and root mean square (RMS) of both axial and radial velocities is reported in Fig. 3.9. Black isolines of zero axial velocity are also superimposed in the corresponding plots to clearly identify the recirculation zones. The presence of the Inner (IRZ) and Outer Recirculation Zones (ORZ) is

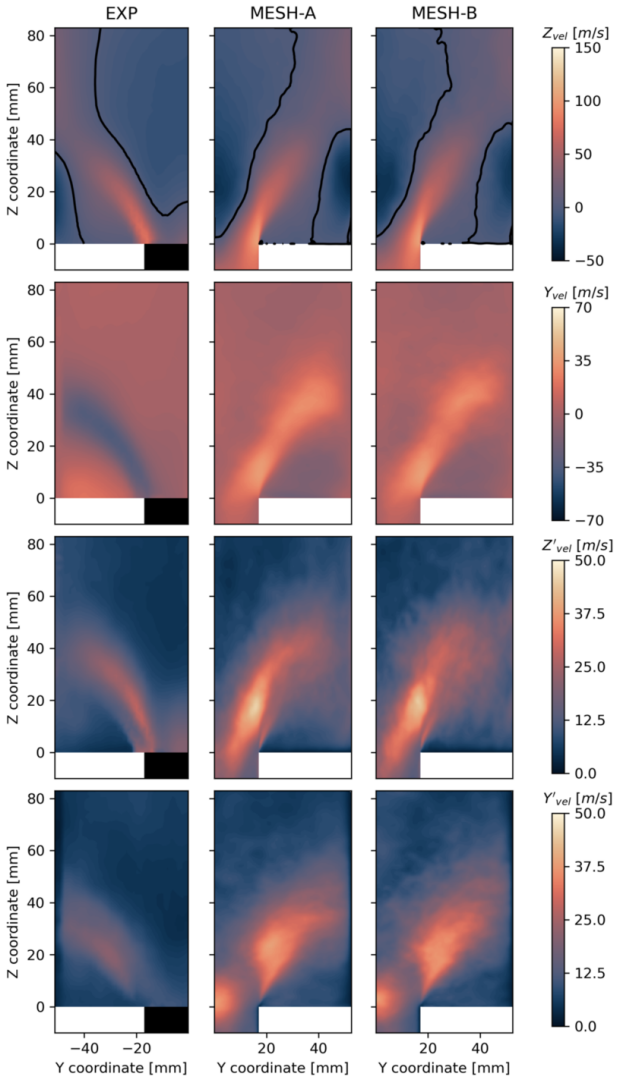

Figure 3.9: Non-reactive flow field comparison in terms of time-averaged and RMS of both velocity components between experiments and the two meshes.

justified by the swirl number larger than 0.6 at the inlet of the combustion chamber according to the selected test point and the typical swirling flow structure is observed. From a first analysis, no significant differences appear between the two meshes for all the quantities due to the fact that the same sizing is used inside the chamber. On the contrary, a slightly different behavior is observed at the exit of the mixing tube compared to the experimental data in terms of the shape of the recirculation zone. This is probably related to the behavior of the axial jet as pointed out in [59]. Indeed, a different penetration inside the mixing tube could explain the slight overestimation of the inner recirculation zone extension.

Therefore, to investigate the trend of the pure axial jet inside the mixing tube where also the two meshes have different spatial discretization, a comparison of the time-averaged axial velocity along the black dotted line reported in Fig. 3.10 is performed.

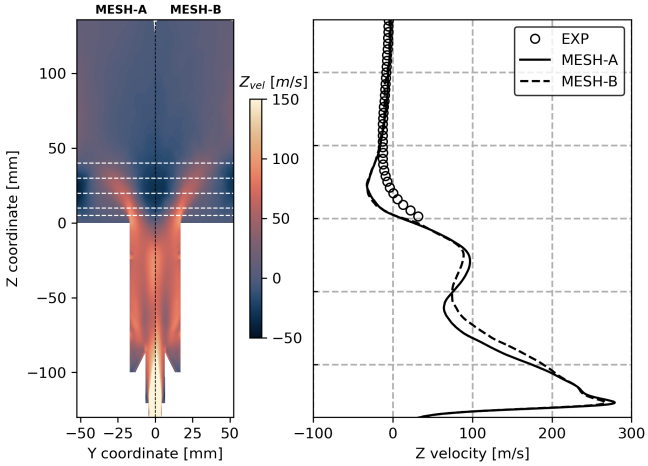

Figure 3.10: Time-average axial velocity contours (left). Comparison of time-averaged axial velocity along the black dotted line (right).

From one side, for MESH-B in which strong refinements are generated at the exit of the axial jet, a higher penetration inside the mixing tube can

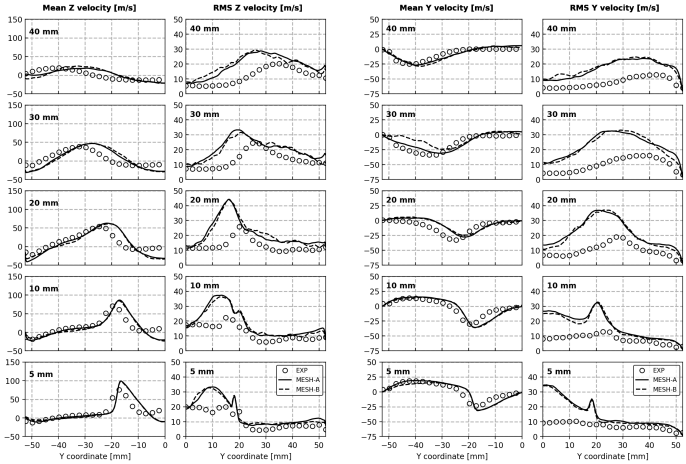

(a) Axial velocity *(b) Radial velocity*

Figure 3.11: Comparison of time-averaged axial (left) and radial (right) velocity profiles with their respective RMS at different heights inside the combustion chamber.

be pointed out with respect to MESH-A. On the other side, both meshes as previously highlighted, fail to reproduce the correct penetration of the IRZ. Since the experimental data are available only inside the combustion chamber, no further considerations can be concluded unfortunately on this aspect. As far as seen from CFD simulations, however, the slight difference between the two jets in the mixing tube has no impact on the overall performance in the combustion chamber.

To validate the cold flow field against experiments, time-averaged velocity profiles are shown in Fig. 3.11 for different *z-coordinates*. The five heights used to draw the lines are highlighted in white in Fig. 3.10 for the sake of clarity.

Due to the same grid resolution inside the chamber, no significant differences can be observed between the two meshes in terms of mean and RMS velocity for both components. At all stages, a fair good agreement with the experimental data can be pointed out even if in the first section,

a higher peak of axial velocity is retrieved in the swirling jets (Fig. 3.11a). This discrepancy tends to decrease moving downstream inside the chamber. At the same time, the swirling jets are closer to the center line with respect to what is observed experimentally. In fact, to confirm this, a slight underestimation of the radial velocity in the first sections inside the combustion chamber can also be observed in Fig. 3.11b. This probably causes the higher intensity and penetration of the inner recirculation zone, as previously mentioned, due to the confinement of the recirculation bubble along the axis of the burner.

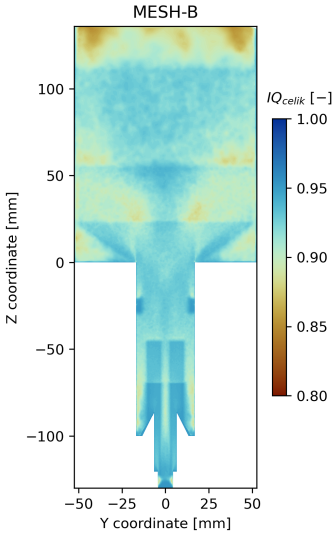

Figure 3.12: Time-average Celik index field for MESH-B.

Regarding the velocity fluctuations instead, a not proper agreement is retrieved for the two components at the first stages along the centerline (*y-coordinate* $\approx$ 0 mm). In particular, at the exit of the mixing tube, it is found from both simulations a clear fluctuation of the axial jet in the tangential direction at 1250 Hz which is not observed experimentally, see again Fig. 3.9. It is mandatory to specify that in both cases, the

Celik [140] criterion is well satisfied in all the domains. In support, the time-averaged field of the Celik index for the refined case (MESH-B) is shown in Fig. 3.12.

In light of the results emerged during the mesh sensitivity analysis, the refined mesh (MESH-B) is selected for the reactive simulations.

3.3.2 Reactive velocity flow field

Moving to the reactive conditions, a first qualitative comparison in terms of time-averaged axial velocity is reported in Fig. 3.13 between the experimental data and all the simulations performed. Black isolines of zero axial velocity are superimposed to identify the recirculation zones. Compared to the cold conditions, an overall acceleration is observed due to the thermal expansion of the burnt gases. The simulations correctly predict the flow field even if some discrepancies can be pointed out like the extension of the IRZ and the velocity peak of the swirling jet. For a better comparison against the experimental data, profiles of mean and root mean square of both axial and radial velocity at the same five heights inside the combustion chamber are reported in Fig. 3.14.

By analyzing the profiles, no significant differences appear between the three TFM solutions even with non-adiabatic thermal boundary conditions (T-TFM). Similarly, the two solutions with FGM show the same trend in both mean and RMS terms. In contrast, comparing these results with those obtained by TFM simulations, a radical improvement in agreement with the experimental data is observed, especially at a high axial distance from the back plate (z-*coordinate* > 20 mm). In fact, the peak of axial velocity as well as the opening of the swirling jet is well reconstructed at all stages for the TFM simulations. It is of paramount importance to keep in mind the slight overestimation of the axial velocity along the centerline (y-*coordinate* ≈ 0 mm) at the exit of the mixing tube (z-*coordinate* < 10 mm) for the FGM simulations with respect to the TFM ones since, as better described in the next section, it plays a key role in the stabilization mechanism to avoid the flashback. To further validate the numerical results, a comparison in terms of mean and root mean square of radial

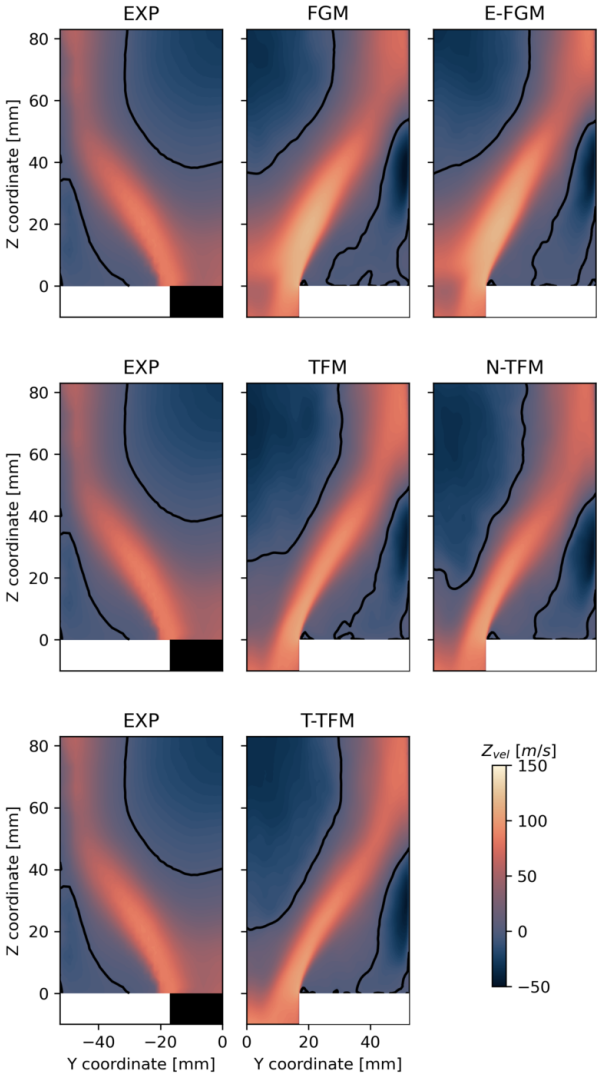

Figure 3.13: Reactive flow field comparison in terms of time-averaged axial velocity between experiments and all the simulations. Black isolines of zero axial velocity are also superimposed.

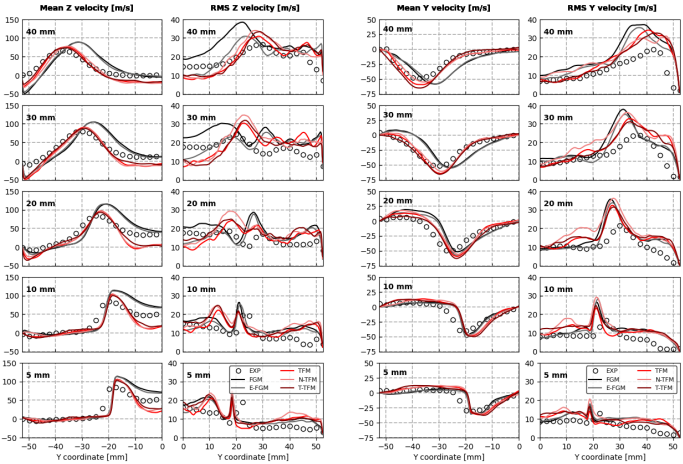

(a) Axial velocity *(b) Radial velocity*

Figure 3.14: Comparison of mean axial (left) and radial (right) velocity profiles with their respective RMS at different heights inside the combustion chamber.

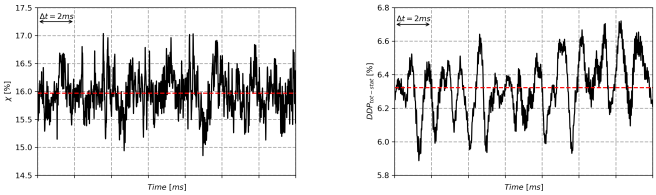

(a) Flow split χ *(b) $DDP_{tot-stat}$*

Figure 3.15: Flow split parameter (left) and pressure drop (right) across the burner for T-TFM simulation.

velocity on the same five axial stages is reported in Fig. 3.14b. Also in this case, the TFM results perfectly retrieve the position and amplitude of the mean radial component with respect to the FGM according to the experimental data. Finally, thanks to the local refinements generated in the reaction zone, both velocity fluctuations in the axial and radial direction are well reconstructed by the simulations even if the FGM cases tend to slightly overestimate the experimental data.

The last part of this section is devoted to analyzing the flow split and pressure drop across the burner in reactive conditions. As said before, unfortunately, no experimental data are available and therefore only numerical results are here reported considering the T-TFM simulation as a reference. The flow split parameter is evaluated at runtime according to Eq. 3.1 instead the pressure drop is computed considering the mass-weighted average of total pressure inside the air plenum and the static one inside the combustion chamber at sufficient distance from the chamber back plate. Results are reported for approximately one flow through time in Fig. 3.15. In detail, the split stabilizes around a value of 16 % instead the pressure drop oscillates around the $\approx 6.3\%$.

3.3.3 Mixing analysis

The mixing process plays a key role in the dynamic of the burner and consequently in the flame stabilization mechanism. Therefore, a good

prediction of the fresh mixing and the conditions at which the combustion takes place is mandatory to capture the flame shape. To better visualize the process that occurs inside the mixing tube, a cross-section of the rig is reported in Fig. 3.16a for the baseline FGM and TFM simulations showing the equivalence ratio distribution. It is important to highlight that the equivalence ratio for the FGM case is calculated starting from the transported mixture fraction Z instead, for the TFM, it is evaluated through species mass fraction using Bilger's definition [98].

By analyzing the maps, it is possible to see how the fuel injected from the bottom of the mixing tube (Y_{H_2}) is pushed along the centerline from the later air jets coming from the swirler channels (Y_{Air}^{sw}). Due to the high velocity of the pure axial jet, the hydrogen is not able to penetrate it and starts to mix with air in these high-turbulence shear layers (-83 mm < *z-coordinate* <≈ -50 mm). After that, a local rich mixture (with respect to the nominal equivalence ratio $\phi_{nom} = 0.6$) is formed along the centerline while a leaner one is present near walls despite some rich pockets of a fresh mixture are still present in such zones (*z-coordinate* < -25 mm). Then, thanks to the small dilution holes (Y_{Air}^{dh}) which inject pure air into the mixing tube, a lean mixture is guaranteed near the wall in order to avoid a boundary layer flashback. After this point, a technically premixed mixture enters the chamber that feeds the flame front. To clearly visualize the fuel distribution and the differences between the two approaches, five profiles of mean equivalence ratio across the burner are reported in Fig. 3.16b. It is important to highlight that no differences appear between the models inside the mixing tube (*z-coordinate* < 0 mm) even if the FGM equations are written with the unity Lewis assumption. This confirms that the preferential diffusion effects affect mainly the zones in which the reactions take place [119], as can be observed at the exit of the mixing tube (*z-coordinate* = 0 mm and *y-coordinate* ≈ ± 17 mm) in which all the TFM simulations retrieve a peak of equivalence ratio. On the contrary, the FGM fails to catch these effects proving a slightly different mean composition inside the combustion chamber. So far, these considerations are made by analyzing time-average fields that

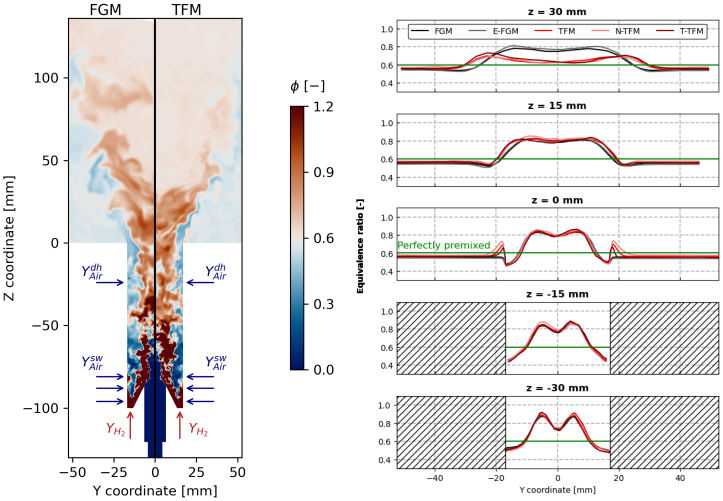

(a) Instantaneous ϕ

(b) Time-avereged ϕ

Figure 3.16: Instantaneous equivalence ratio field for FGM and TFM simulations (left). Time-averaged equivalence ratio profiles at different heights inside the mixing tube and combustion chamber (right).

may not be sufficiently representative to visualize these effects clearly. Therefore, a localized instantaneous distribution is analyzed in detail later to clarify this concept. Finally, a green solid line that represents the perfectly premixed conditions is also superimposed in Fig. 3.16b. Even in the long mixing tube configuration, only at *z-coordinate* $>$ 30 mm the nominal composition is retrieved, showing the technically premixed condition under which the burner operates.

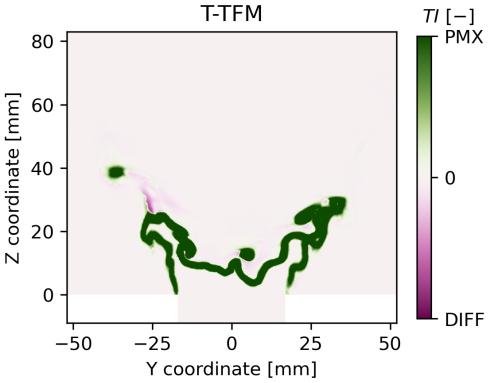

Figure 3.17: Instanteneous normalized Takeno index conditioned by the net H_2 rate for the T-TFM simulation.

Regarding this last point, some considerations must be made in order to clarify the numerical setup employed for the TFM approach. In fact, this method is theoretically correct for premixed flames [91] in which the flame front is artificially thickened and resolved on the current LES grid, as explained in Sec. 2.1.3.1. Recently, to handle this problem and use the TFM approach in multi-regime combustion, some new strategies are introduced. One of them is based on the Takeno Index (TI) [141] used to identify the burning regime. In particular, the Takeno index is defined as the scalar product between the gradient of the fuel and oxidant mass fraction (hydrogen and oxygen respectively for the current study). Values of TI greater (lower) than zero identify a region in which

the combustion takes place in premixed (diffusive) conditions. With this new methodology, the thickening is kept active in the premixed regions while it is automatically turned off in diffusive ones. This methodology is validated in several academic test cases [82, 142, 143] showing good results dispute the high computational cost required since in diffusive zones, which may not be known a priori, the mesh should be fine enough to resolve the flame front.

For the current study, an instantaneous TI distribution conditioned by the local net hydrogen rate is reported in Fig. 3.17 for the T-TFM simulation. Since for the most part the flame front burns under premixed conditions, it is chosen to adopt the baseline TFM without any type of correction for this numerical campaign, limiting the computational cost. Further analysis on this point can be conducted to verify the actual impact of this assumption.

3.3.4 Flame shape

After the assessment of the velocity and mixing fields, to investigate the stable flame, a comparison in terms of normalized OH mass fraction is performed in Fig. 3.18 in which the numerical maps are compared with the normalized OH-PLIF image (cropped above 35 mm to highlight the stabilization zone).

The rig, under these operating conditions, is characterized by an M-shape flame, as it is possible to see from the left column of Fig. 3.18 in which the experimental map is reported. Indeed, the reactions occur in both inner and outer shear layers, with a maximum value of the OH around *z-coordinate* $\approx$ 20 - 30 mm. All the models correctly capture the flame shape even if in both FGM solutions, the flame stabilizes close to the exit of the mixing tube due to the higher reactivity predicted by the numerical approach employed. However, all the TFM simulations correctly predict the flame anchoring position observed experimentally. In fact, to better identify this point, the distribution of OH along the centerline (*y-coordinate* = 0 mm) normalized by the maximum in such line is reported in Fig. 3.19.

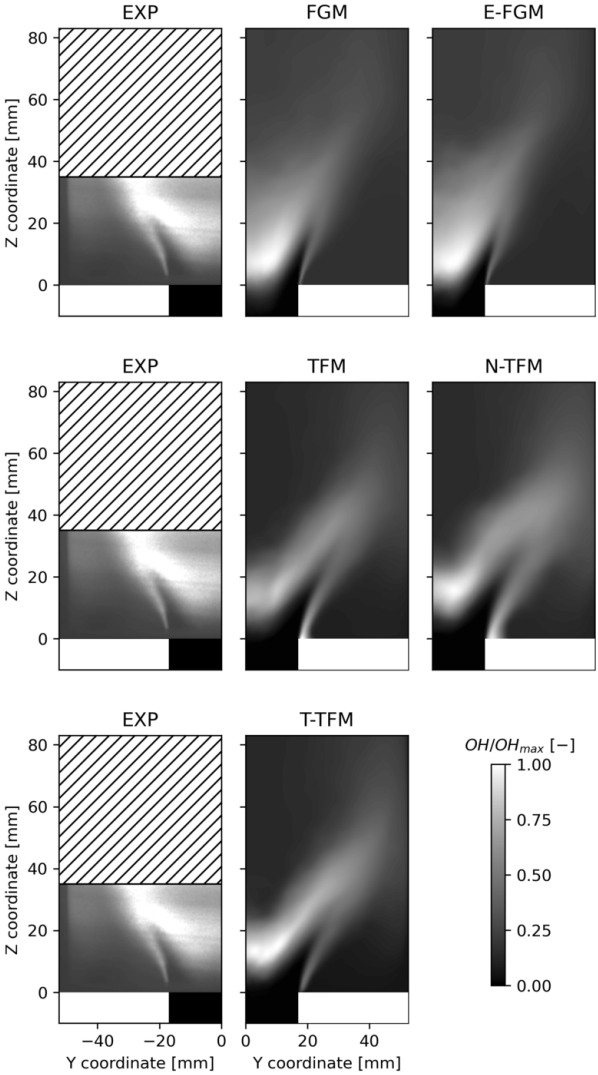

Figure 3.18: Comparison in terms of mean normalized OH mass fraction distribution.

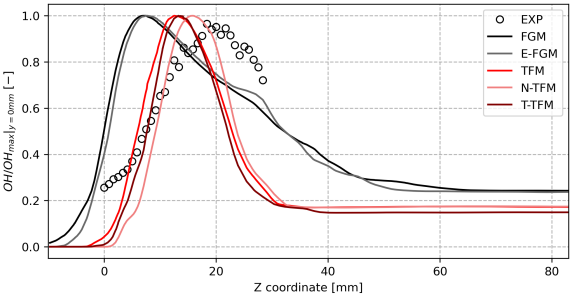

Figure 3.19: Mean normalized OH mass fraction distribution along the centerline.

From an experimental point of view, the maximum is reached at around 20 mm downstream of the back plate while the three TFM simulations provide approximately the same results ($\approx$ 15 mm). These simulations also capture the correct trend in the first region (*z-coordinate* $<\approx$ 15 mm) even if an overestimate of the OH decay is present in the post-flame region (*z-coordinate* $>$ 20 mm) which is probably related to the slight underestimation of axial velocity. On the contrary, even with the higher axial velocity at the exit of the mixing tube with respect to experimental data (see again Fig. 3.14a), the FGM simulations drastically overestimate the position of the maximum due to the high reactivity predicted of such approach.

Coming back to Fig. 3.18, it is also interesting to see how no significant differences appear between the baseline TFM and N-TFM. So, for these operating conditions, even 5 points are enough to correctly describe the flame front and therefore, the last simulation with the thermal boundary condition (T-TFM) is run with 5 points.

By analyzing the experimental map, it is also clear how the flame lips close to the mixing tube exit corners locally lift due to the heat loss present in such zones. On the other hand, the flame is attached to the wall in all the simulations with the exception of the T-TFM in which non-adiabatic conditions are prescribed. In fact, it is possible to see

through the instantaneous and time-averaged temperature fields reported respectively in Fig. 3.20a and Fig. 3.20b the lower temperature in the outer recirculation zone for the T-TFM which locally reduced the reactivity in the outer shear layer where the flame stabilizes.

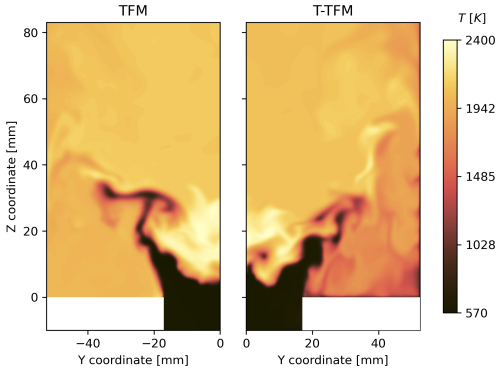

(a) Instantaneous

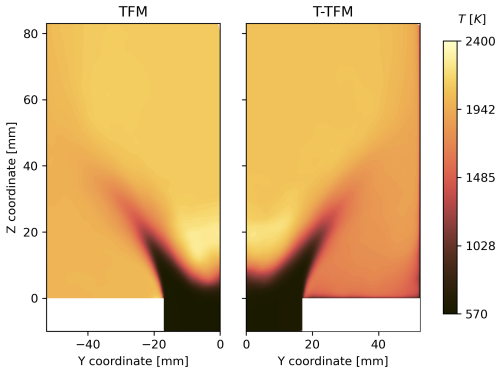

(b) Time-averaged

Figure 3.20: Instantaneous (top) and time-averaged (bottom) temperature field for TFM and T-TFM simulations.

To better visualize the different reactivity predicted by the two approaches and the local behavior in the stabilization zone, the normalized

product formation rate for FGM and heat release rate for TFM simulations is reported in Fig. 3.21. Blue isolines of the 80 % of the normalized quantities (θ/θ_{max}) are also superimposed on the local zoom plots. Although the results look quite similar between the TFM simulations, the T-TFM shows a local lift-off of the flame according to the experimental data with respect to the other simulations in which the flame is completely attached. So, as expected, the local effects of a finite temperature in the stabilization zones play a key role in the anchoring and flame dynamics process. It is also important to highlight how the hydrogen mass fraction is consumed in a lower flame surface area (compact flame) for the FGM simulations with respect to the TFM ones, demonstrating again the higher reactivity retrieved from this approach.

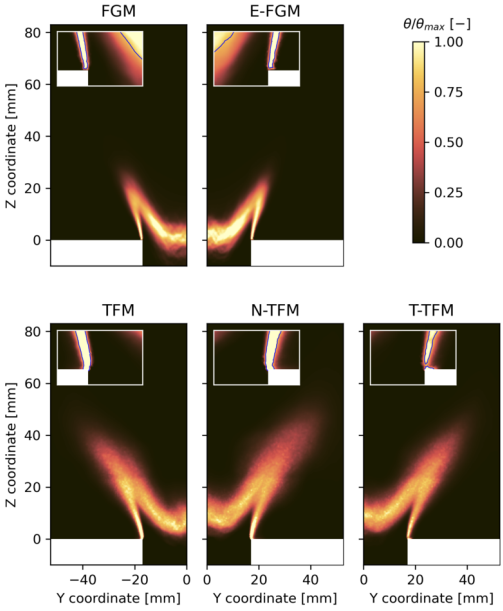

Figure 3.21: Time-averaged normalized product formation rate (FGMs) and heat release rate (TFMs) distribution. Blue isolines at 80% are also superimposed.

3.3.4.1 Stretch effects on FGM

For a detailed analysis of the inclusion of stretch and heat loss effects on the FGM approach, the reader is referred to the two top plots in Fig. 3.21 where the normalized mean product formation rate for FGM and E-FGM simulation are reported. The response of the models is quite similar since the flame shape is the same and only slight differences appear between them. In particular, a higher reactivity can be pointed out along the inner and outer shear layers for the E-FGM case. In these regions, in fact, a higher value of flame stretch (given by the combination of strain and curvature) is present, as shown in Fig. 3.22 in which its trend with the Γ distribution is reported for both instantaneous and time-averaged conditions. Black and red isolines of product formation rate are superimposed in order to identify the zone where the source term retrieved from the table ($\widetilde{\omega_c}$) is not zero. In fact, as explained in Sec. 2.1.3.3, the extended model acts only in the regions where the combustion takes place. So, stretch and Gamma have an impact only in the regions within the isolines.

Due to the adiabatic conditions considered in this case (Tab. 3.2), the Gamma table is queried without considering the heat loss effects ($\Gamma(Z, \psi, k) = \Gamma(Z, \psi = 1, k)$). According to the Gamma table reported in Fig. 3.8, only values greater than one are observed with a maximum in the outer shear layers (where the stretch reaches its maximum) since the reactions occur in lean conditions. To better visualize this behavior, the probability density function of Gamma is calculated for an approximate flow through time and its distribution is reported in the strain rate-mixture fraction space in Fig. 3.23. White isolines extracted from the Gamma table (Fig. 3.8) are superimposed for adiabatic conditions. Two different peaks are clearly visible in the bottom left part of the contour. The first one is located around the mixture fraction of 0.025 and represents the combustion that takes place in the inner shear layers. On the other hand, the second peak is located at a mixture fraction of 0.017 and represents the flame front in the outer shear layers. From this map, it is also clear that the correction acts in a proper way but, due to the operating condition

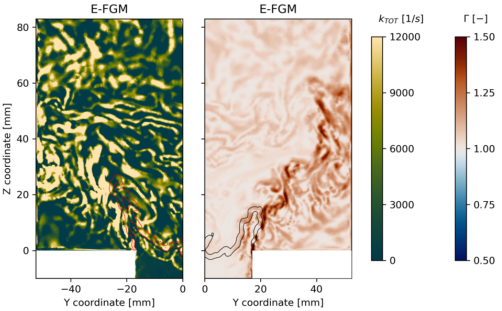

(a) Instantaneous

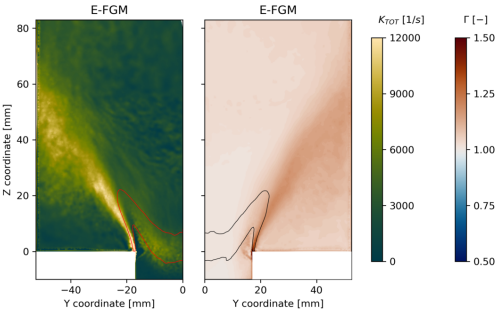

(b) Time-averaged

Figure 3.22: Instantaneous (top) and time-averaged (bottom) stretch (left) and Gamma (right) distribution for E-FGM simulation. Red and black isolines of product formation rate are also superimposed.

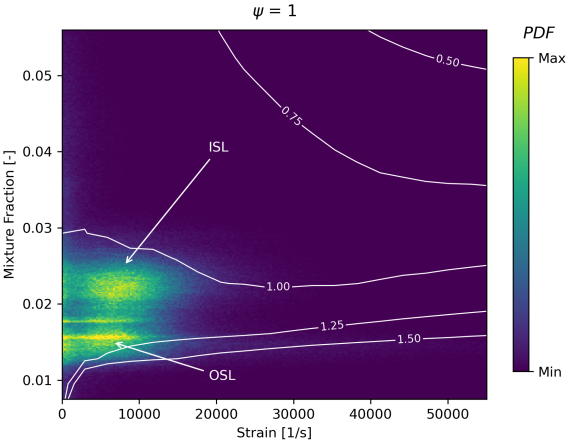

Figure 3.23: Probability Density Function of Γ *in mixture fraction and strain rate space for adiabatic conditions* ($\psi = 1$)*. Isolines of* Γ *are also superimposed.*

under investigation which limits the maximum value of $\Gamma_{max} \approx 1.25$, the differences between FGM and E-FGM model, i.e. the stretch effects on the flame, are only localized and do not alter considerably the global flame shape.

3.3.4.2 Non-unity Lewis number effects

The last point that needs to be discussed is the non-unity Lewis number effects on the flame behavior previously introduced in the mixing process section. To this aim, the baseline FGM and TFM simulations are taken as reference. By considering an instantaneous distribution of equivalence ratio shown in Fig. 3.24 it is possible to point out again the technically premixed conditions reached at the exit of the mixing tube. Black isolines representative of the isovalue of product formation rate or heat of reaction depending on the simulation considered are also superimposed in order to visualize the reaction zones. In these regions, the TFM simulation accounts for the fast diffusion of light species such as

hydrogen where strong temperature and species gradients are present. In fact, it is possible to see a local fuel redistribution across the flame front for this case. On the other hand, for the FGM simulation in which the equations are solved with the unity Lewis number assumption, no local ϕ gradients are observed since such effects are not accounted for.

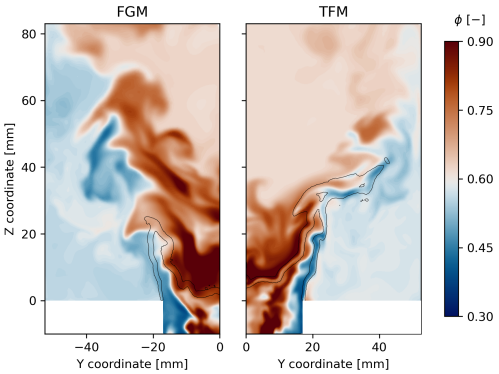

Figure 3.24: Instantaneous equivalence ratio contour for FGM and TFM simulations. Black isolines to identify the flame front are also superimposed.

To further investigate the consequences of this phenomenon, the local temperature probability density functions over the mixture fraction are reported in Fig. 3.25 for the two simulations considering approximately one flow through time of sampling. A black line representative of the equilibrium temperature computed from its relative reaction mechanism (ELTE and Boivin respectively) is superimposed in the plots. Histograms of both quantities are also reported dividing the region between the ISL and OSL to identify the main contribution in which the reaction occurs.

The first observation that can be drawn by analyzing the histogram is the clear presence of a second peak of reactions that occur on the OSL in the TFM case. This is related to the preferential diffusion effects which are enhanced in such zones (OSL) due to the simultaneous presence of a flame front (elevated mass fraction gradients) and high-strain regions

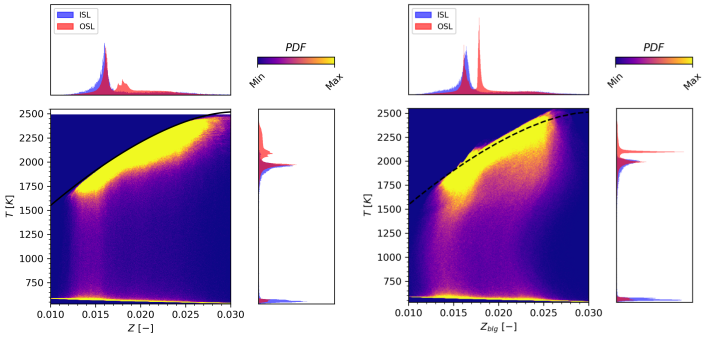

(a) FGM *(b) TFM*

Figure 3.25: 2D PDF on temperature and mixture fraction space for baseline FGM (left) and TFM (right).

[119]. In fact, the hydrogen molecules tend to move across the flame front generating a locally richer mixture (with respect to the nominal value) as previously described in Fig. 3.16b and Fig. 3.24 providing a peak in reactions.

Moreover, it is possible to point out how the maximum temperature reached in the FGM case is always below the equilibrium one according to the construction of the PDF. On the other hand, in the TFM case, some zones of the domain reach a temperature higher than the one at the equilibrium. This phenomenon is referred in the literature as super-equilibrium and is related again to the preferential diffusion effects as explained in [144].

Besides not capturing these effects, the FGM simulation predicts a wider range in which the combustion takes place up to $Z \approx 0.030$ (see again Fig. 3.25) which results in a different flame temperature.

In fact, comparing the time-averaged temperature fields reported in Fig. 3.26 it is evident a high temperature inside the IRZ for the FGM calculation with respect to the TFM one. As a consequence, further analysis like the NO_x estimation could be drastically influenced by this overestimation providing unfeasible results since thermal NO_x production

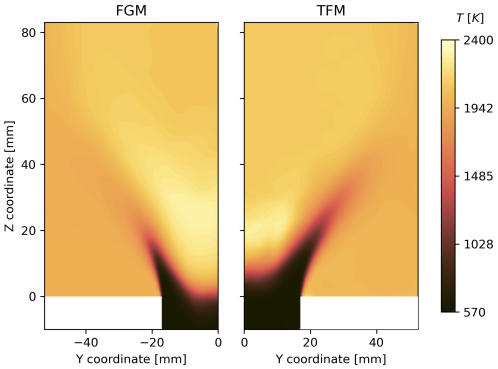

Figure 3.26: Time-averaged temperature field for FGM and TFM simulations.

doubles for every 90 K temperature increase when the flame temperature is above 2200 K [138]. Therefore, the inclusion of these effects in the numerical simulations when studying lean hydrogen flames is mandatory to correctly predict the conditions at which the combustion occurs and consequently the flame shape and the aero-thermal field.

3.4 Computational cost

All the simulations presented in this chapter are carried out on an HPC cluster with 40 Intel® Xeon® Gold 6248 CPUs per node. On this hardware, the computational cost required to simulate an approximate flow through time is estimated to be 24660 and 72000 CPUh for the FGM and TFM respectively. In addition, the query of the external table for the extended FGM model does not affect significantly the computational cost that is demonstrated to be the same as the pure FGM. Although the employment of the skeletal Boivin mechanism for hydrogen combustion allows an accurate description of the chemical kinetics with only 9 species, the number of equations required in the TFM simulations is double with respect to the FGM calculation (7 against 13 eqs.). A summary of the

computational cost is reported in Tab. 3.3. In conclusion, this brings an increase in calculation cost of about $\approx 65\%$.

Computational cost		
Case	**N° eqs.**	**CPUh**
FGM	7	24660
E-FGM	7	≈ 25000
TFM	13	72000

Table 3.3: Summary of the computational cost.

3.5 Final considerations

In the present chapter, a numerical campaign with the commercial pressure-based software ANSYS Fluent® aimed to assess the current industry-standard turbulent combustion models is presented. The two methodologies based on a tabulated chemistry (FGM) and a species transport (TFM) approach are considered. Moreover, a cost-efficient method to account for the stretch and heat loss effects on flame reactivity is introduced within the FGM context. All these strategies are tested through high-fidelity Large Eddy Simulations on a laboratory test case provided by the Technische Universität Berlin that presents the main features of an aero-engine combustor. The rig deals with a technically premixed, swirl-stabilized hydrogen-air flame under atmospheric conditions. The experimental analysis carried out on the burner investigates the impact of a pure axial jet on the stabilization mechanisms of the flame and consequently the resistance to flashback. Detailed measures in both non-reactive and reactive conditions are available.

Before facing the complex reactive simulations, a mesh sensitivity in the LES framework is carried out in the non-reactive conditions to define the appropriate grid sizing. Higher penetration of the axial jet is observed inside the mixing tube for the refined mesh even if the two simulations provided the same results inside the combustion chamber. In both cases, an overestimation of the inner recirculation zone intensity can be observed

in the first regions downstream of the mixing tube exit. In light of the results, the refined grid is adopted for the reactive calculations.

Starting from the validation of the reactive flow field, it is found that the TFM approach better predicts the opening of the swirling jet, and furthermore, the thermal boundary conditions as well as the number of points have a minor impact on the velocity fields. On the contrary, the FGM simulations slightly overestimate the velocity peak of the swirling jet and at the exit of the mixing tube along the centerline. Then, the mixing process which occurs inside the mixing tube is analyzed showing the technically premixed conditions at which the reactions take place. In particular, thanks to the Takeno index, it is established that most part of the hydrogen mass fraction burns in premixed conditions demonstrating the validity of the numerical setup employed. Moreover, it is found that no differences appeared between the two approaches inside the mixing tube despite the FGM equations are solved with the unity Lewis number assumption. On the contrary, when the reactions take place, only the TFM is able to account for the fast hydrogen diffusion.

Regarding the flame analysis, all the simulations correctly retrieve the M-shaped flame observed experimentally even if the FGM drastically overestimates the reactivity and consequently the anchoring point. The inclusion of the stretch effects in the E-FGM predicts a flame stabilized inside the mixing tube as well despite a slight improvement with respect to the baseline model is observed. It is important to recall that, under these lean and high-turbulence operating conditions, the effects of stretch on the flame are not so relevant and only local effects are observed between the models. Regarding the TFM simulations, although some small differences are present, the number of points used in the discretization of the flame thermal thickness has a minor impact on the final flame shape. On the contrary, as expected, the heat loss on the walls plays a key role in the flame dynamics since only the T-TFM simulation is able to predict the local lift-off of the flame at the exit of the mixing tube according to the experimental data. Regarding the computational cost, despite the carbon-free nature of hydrogen and the consequent reduced number of species

and reactions required to describe the chemical kinetics with respect to generic hydrocarbons, a TFM simulation is ≈ 65 % more expensive than one with the FGM.

In conclusion, further investigations under different operating or test cases are required to better understand the accuracy of the extended model (E-FGM) even if in the present days, it represents a valid cost-efficient case-independent strategy to include stretch and heat loss effects on hydrogen flames with an LES approach. In any case, when dealing with hydrogen, the direct inclusion of preferential diffusion effects is mandatory to predict the correct flame shape and in this optic, the Thickened Flame Model provides a valid alternative.

Chapter 4

Bluff body test case

In this chapter, the numerical campaign carried out within the European project *HydrogEn combuSTion In Aereo engines* (HESTIA) is presented. This activity studies the ignition dynamics of a lean, perfectly premixed hydrogen flame, stabilized on a conical bluff body, installed at the Norwegian University of Science and Technology (NTNU). In particular, the numerical setup derived from the previous analysis on TUB is employed throughout this second work. The experimental campaign carried out on the test rig [30, 64], despite the simple configuration and operating conditions not representative of an aero engine combustor, systematically analyzed the ignition process transition from pure methane to pure hydrogen, providing key information on the actual behavior. Furthermore, comprehensive measurements of the complete dynamic process are obtainable through velocity field, flame visualization, and pressure signals, which enable the identification of statistical trends. The set of all these measurements therefore constitutes a crucial dataset for the CFD modeling.

The hydrogen ignition process from spark release to full flame development, up to proper stabilization or permanent flashback, is investigated with a LES-based numerical methodology. From the three phases detailed in Ch. 1, only the second one is examined avoiding the modeling of the

plasma phase. To the best of the author's knowledge, no previous work addresses the investigation of the complete ignition sequence of a lean hydrogen flame in different scenarios. The objective is to identify the key aspects involved during the ignition dynamic, considering and evaluating the different characteristics of hydrogen. Particular attention is paid to the transport models and, therefore, to the impact of the Lewis number on the flame evolution, highlighting the effects of preferential and thermal diffusion.

This chapter is organized as follows, in the first part, a description of the test rig, the experimental setup and the measurement techniques used to collect the experimental data is provided. Then, the computational domain and the mesh grids used for the simulations are detailed. The numerical setup employed is subsequently presented, highlighting the sensitivity performed in the reactive conditions. Finally, starting from the validation of the cold flow field, the ignition simulations are presented. The soft ignition case is first analyzed to assess the influence of the spatial resolution and the validation of the employed setup. Then, the permanent flashback simulation is introduced analyzing the influence of the plate at the outlet section and the dynamics that occur inside the injector. Some of the results presented in this chapter are also part of a master thesis carried out by Giada Senatori [145] under the supervision of the author.

4.1 Investigated experimental test rig

The rig under investigation is the atmospheric single burner installed at the Norwegian University of Science and Technology (NTNU) shown in Fig. 4.1.

The cylindrical combustion chamber has an internal diameter of 60 mm, a length of 150 mm and it is realized with quartz providing an optical access for diagnostics. The mixture is supplied by two opposite inlets at the bottom of the rig. A grid with appropriate spacing is placed downstream of the jets in order to uniform the turbulence intensity and length scales. The plenum ends with a converging section connected to a

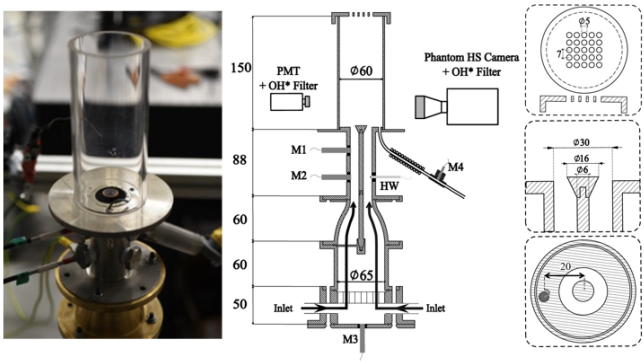

Figure 4.1: (Left) Picture of the bluff body test rig. (Right) Schematic representation of the test rig and experimental setup (adapted from [30, 64]). Detail of Plate25 and spark is reported.

duct with an internal diameter of 30 mm. Along the center of the duct, a rod holds the conical bluff body, used to stabilize the flame. A schematic representation of the test rig is provided by Fig. 4.1. As reported in [30], during the experiments, the bluff body is preheated and maintained at a constant temperature of 470 K, measured with a pyrometer. This allows to achieve similar conditions in terms of heat losses during each experimental test and to prevent any potential impact of the wall temperature effects on the ignition dynamics. When the chamber is filled, after a sufficient time to produce a homogeneous mixture, the ignition is obtained using an electrical spark plug located above the chamber back plate at $\approx$ 20 mm from the chamber axis. The energy delivered by the ignition device is equal to 36 mJ with a frequency of 50 Hz even if the first spark is sufficient to ignite the mixture. Due to the stochasticity of the process, the experiments are repeated at least 10 times under the same operating conditions to provide statistical results.

Several configurations are experimentally investigated varying the combustion chamber back pressure by adding a perforated back plate, the mixture properties ranging all the blends from pure methane (PH0) to pure hydrogen (PH100) and the bulk velocity U_b of the flow (2-5 m.s^{-1}),

as schematically illustrated in Fig. 4.2. In particular, three different outlet restrictions are tested (W/o Plate, Plate 25 and Plate 16) in order to modify the chamber back pressure. For instance, by considering the cases with $U_b = 5$ m.s^{-1}, the pressure drop ΔP during cold-flow stationary conditions moves from 30 Pa to 100 Pa and 140 Pa by adding the plates respectively. The combination of such conditions allows to achieve different scenarios [30]:

- Soft ignition (green): after the spark the flame propagates and stabilizes on the burner.
- Transient flashback (orange): after the kernel formation, the flame propagates rapidly inside the injector upstream the bluff body before being expelled and then stabilizes on the burner.
- Permanent flashback (red): after the ignition, the flame propagates upstream the bluff body and stabilizes inside the injector.

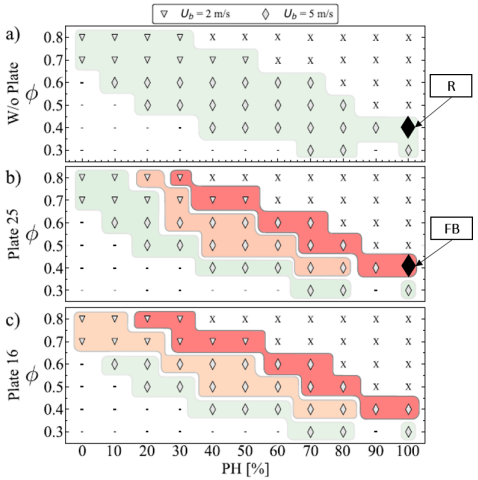

Figure 4.2: Experimental test matrix adapted from [30]. Black diamonds highlight the selected operating conditions for the numerical simulations.

Detailed measurements are collected during the entire ignition sequence, as schematically reported in Fig. 4.3. The pressure signals inside

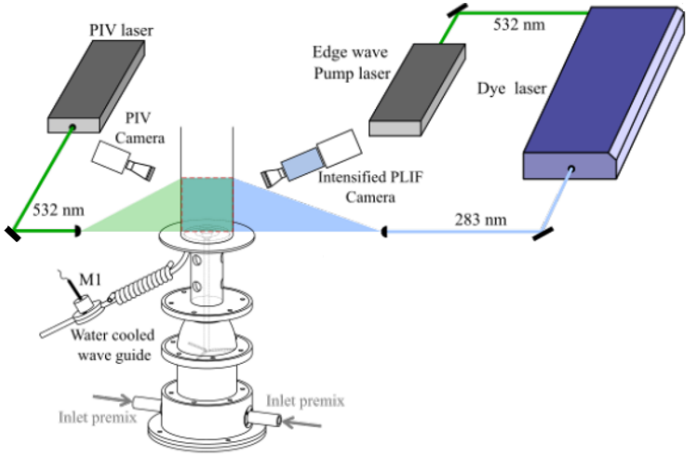

Figure 4.3: Schematic representation of the PIV/OH-PLIF diagnostic system [64].

the chamber and the duct are measured with three pressure probes, labeled M1-M2 and M4 in Fig. 4.1. The HS-PIV technique is used to acquire the velocity flow field in non-reactive conditions and it is time-synchronized with the high-speed OH-PLIF during the ignition tests to record simultaneously also the flame evolution until the complete stabilization. The OH* chemiluminescence is adopted in reactive conditions to provide further information about the reaction zones. Hot wire (HW) velocity measurements through a probe placed 70 mm upstream of the bluff body are collected to characterize the inlet velocity U_b. It is important to highlight that HW measurements are not carried out during pure hydrogen tests due to the risk of mixture pre-ignition in the duct forced by a potential catalytic activation caused by the HW probe.

4.2 Setup of the simulations

The bluff body test case is analyzed using the commercial software ANSYS Fluent® 2022$R1$, with the main purpose of investigating the ignition dynamic. A non-reactive LES simulation with only air (named NR) is initially performed to validate the cold flow field. Subsequently, starting from a cold hydrogen-air LES simulation, the spark is released and the reactive simulations are conducted until the achievement of stable conditions in terms of pressure, velocity and thermal power. Finally, the solutions are averaged in order to obtain the reactive time-statistic results to compare with the available experimental data. It is important to underline that only the second phase of the ignition process, concerning the flame growth, is examined. In fact, as reported in Ch. 1, the initial stages of kernel formation involve plasma-thermodynamics and phenomena characterized by significantly small spatial and temporal scales, resulting in complex and time-consuming modelling [146]. Furthermore, since the investigation is focused on a single injector, the light-round phase is not detailed.

Table 4.1 provides a summary of the simulations performed, pointing out their main characteristics.

Case	Mixture	Mesh	Plate	Time-step	Soret
NR	Air	Coarse	W/o Plate	$1 \cdot 10^{-5} s$	×
R2	H_2-air	Coarse	W/o Plate	$5 \cdot 10^{-6} s$	×
R3S	H_2-air	Coarse	W/o Plate	$5 \cdot 10^{-6} s$	✓
R6Sr	H_2-air	Refined	W/o Plate	$5 \cdot 10^{-6} s$	✓
FB1Sr	H_2-air	Refined	Plate25	$5 \cdot 10^{-6} s$	✓

Table 4.1: Description of the main characteristics of the performed simulations.

The two points highlighted in Fig. 4.2 are numerically investigated. When no restrictions at the outlet are considered (**R**), the soft ignition case is achieved and the flame properly stabilizes on the burner. On the contrary, with the additional pressure drop promoted by Plate25, the permanent flashback scenario is encountered (**FB**). These two operating

configurations are identical in terms of fuel composition, bulk velocity and equivalence ratio resulting in the same burning velocity and thermal power. A summary of the operating conditions under investigation is reported in Tab. 4.2.

Operating conditions	
Mixture	Perfectly premixed
Fuel	100% H_2
Equivalence ratio	0.43
Operating pressure	101325 Pa
Inlet temperature	298 K
Hot-wire velocity	5 $m.s^{-1}$
Thermal power	5.7 kW
Laminar flame speed	0.25 $m.s^{-1}$
Laminar flame thickness	591 µm

Table 4.2: Summary of the operating conditions considered in this work.

4.2.1 Computational domain and numerical grids

The entire rig composed of the plenum with the turbulence grid, the two opposite inlets, the bluff body holders and the combustion chamber is included in the computational domain, as reported in Fig. 4.4, for all the simulations listed in Tab. 4.1. Furthermore, an external hemisphere is introduced at the outlet of the chamber to mimic the discharge into the atmosphere and to prevent acoustic waves reflection. The proposed modeling permits to avoid any modifications of the acoustic of the system, ensuring consistency with the experimental test rig. The decision to consider the full domain is also related to the necessity to model and resolve the turbulence naturally developed by the flow and consequently, geometric simplifications are reduced as possible. As regards the reference system, the z-axis is aligned with the axial direction of the combustion chamber and the xy-planes represent the transverse planes. The origin of the reference system is placed at the axial coordinate of the back plate, 2 mm upstream from the upper surface of the bluff body.

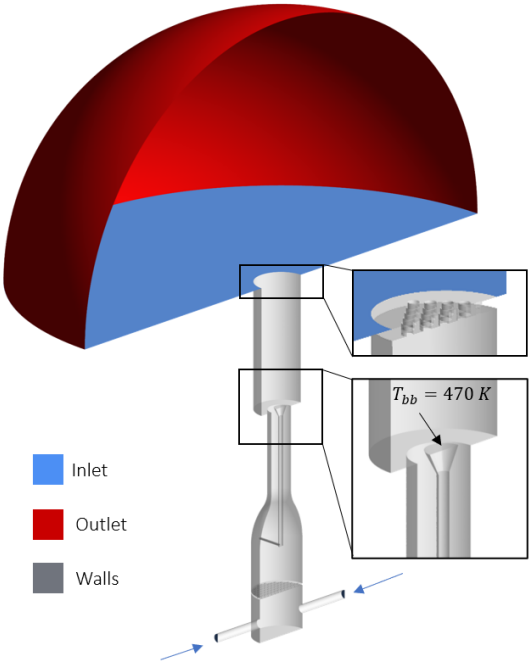

Figure 4.4: Computational domain and boundary conditions.

4.2.2 Mesh

Three different unstructured grids are adopted, all based on polyhedral elements, as shown in Fig. 4.5. For the W/o Plate case, two mesh strategies are tested in order to investigate the impact of the spatial resolution. In both cases, the dimension of the elements within the stabilization zone is maintained below 300 µm with an additional spherical refinement in the spark position in order to properly capture the kernel evolution during the initial steps after the spark. Towards the outlet section, the sizing gradually increases to 1 mm and 400 µm for, respectively, the coarse and the refined mesh. The different discretization of the flame front along the combustion chamber represents the main difference between the two computational grids. To prevent excessive numerical dissipation of the turbulence generated by the opposite jets, the grid cell size between the upstream plenum and burner exit is kept at 400 µm in both cases.

The refined strategy is also adopted in the case of Plate25 in which two further refinements at 300 µm are generated. In particular, the first one which covers the chamber outlet region aims to retrieve the correct flow blockage whereas the second one, generated before entering the chamber, aims to gradually smooth the mesh transition and prevent nonphysical quenching during a flashback event. In conclusion, the two strategies count about 21 and 34 M elements respectively for the W/o Plate case and 37 M for the Plate25 case.

4.2.3 Boundary conditions

A schematic representation of the main boundary conditions is reported in Fig. 4.4. A constant mass flow rate of hydrogen-air perfectly premixed, equal to $\dot{m} = 1.716$ g.s^{-1}, is imposed at the inlet patches. The flow enters with a temperature T = 298 K and in the ignition simulations has an equivalence ratio $\phi = 0.43$. The atmospheric pressure is set at the outlet boundary condition, whereas a low-speed air co-flow is prescribed at the hemisphere inlet to prevent flow reversal. All the other surfaces are representative of solid walls, thus the no-slip condition is applied.

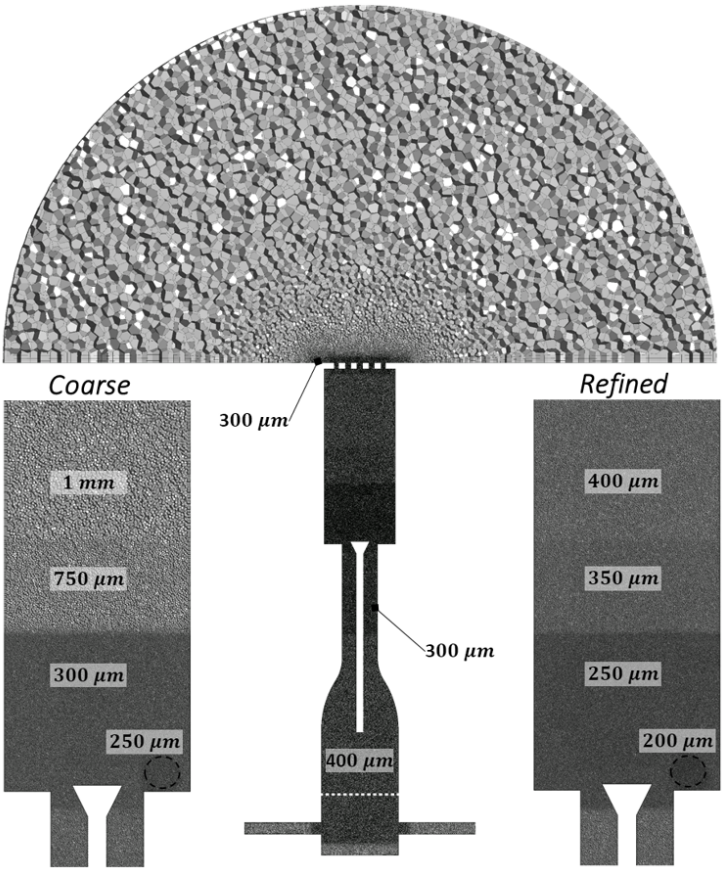

Figure 4.5: Computational grids and refinement zones.

The walls are treated as adiabatic, with the exception of the bluff body, maintained at T=470 K according to the experimental procedure.

4.2.4 Numerical modeling

Regarding the numerical modeling, in all the simulations the effect of the unresolved eddies is modeled with the Dynamic Smagorinsky-Lilly subgrid-scale model [89]. The turbulence chemistry interaction is handled with the Thickened Flame Model in which the thickening is locally applied only in a narrow band of the flame front thanks to a sensor factor Ω, based on the first reaction, and the sub-scale wrinkling effects are retrieved with the Colin [91] efficiency function E (β=0.33). A thickening factor F equal to 4 and a thermal thickness δ_{th} are set constant due to the perfectly premixed conditions considered. This strategy allows to avoid discontinuities in the heat release rate related to the different grid sizes along to chamber. Although the flame propagation after the ignition process involves the entire axial extension of the combustion chamber, the refinement zones are necessary to limit the computational cost. In the refined mesh, δ_{th} is properly discretized in all regions where the reaction occurs, as suggested in [139]. With the coarse grid instead, toward the outlet region the number of points inside the thermal thickness decreases below the suggested value although the code architecture permits its resolution. It is important to recall that in order to avoid ignition failure, the thickening is initiated only when a specific condition, in terms of product mass fraction, is respected, as described in Sec. 2.1.4.

The skeletal mechanism obtained by Boivin [137] (9 species and 12 reactions) is used to describe the system reactivity through the Arrhenius kinetics modeling adopting a stiff chemistry solver to decouple the chemical to the simulation time step [75]. The mixture-average approach is chosen to account for the diffusive problem with the inclusion of the Soret effect according to the summary reported in Tab 4.1.

The ignition of the mixture is performed with the Energy Deposition model proposed by Lacaze [36] implemented in the software via UDF. The deposited energy is equal to 10.8 mJ and corresponds to 30% of the

energy supplied experimentally. In order to maintain the temperature at the spark center below 3000 K, a characteristic spark size of 5.5 mm and a duration of 100 µs are selected. This strategy allows to neglect the first phase that plays a second role in the overall ignition process [23]. In accordance with the experimental setup, the spark is placed at a distance of 20 mm from the chamber axis and 3 mm from the back plate.

The simulations are carried out with a pressure-based solver and the SIMPLEC algorithm is used for the pressure-velocity coupling. Second-order upwind schemes are employed for the spatial discretization and the temporal formulation is realized with a bounded second-order implicit scheme. A constant time step of $1 \cdot 10^{-5}\,s$ is used in the non-reactive case, whereas in the reactive simulations, it is reduced to $5 \cdot 10^{-6}\,s$ in order to ensure a proper resolution of the chemistry. This allows to obtain a Courant number Co<5 in regions of interest.

4.3 Results

In this section, the results of the simulations performed are examined. Initially, the validation of the cold flow field is accomplished through a qualitative and quantitative comparison with the experimental results. Subsequently, the soft ignition simulations are analyzed, comparing the numerical results obtained with different setups and using the experimental data to investigate the ignition dynamic. The analysis investigates the impact of the Soret effect as well as the influence of the spatial resolution. Then, the stable flame condition is evaluated by comparing the flow field and the flame structure with the available data. Finally, the permanent flashback scenario is introduced pointing out the driving mechanisms that promote the occurrence with respect the previous case without outlet restriction.

4.3.1 Non-reactive flow field

This paragraph provides the results of the NR simulation in which the main conditions are summarized in Tab. 4.3. As previously mentioned,

since the non-reactive flow field has a fundamental influence on the ignition dynamic and consequently on the flame stabilization process, its validation is mandatory before addressing the complex reactive case.

NR Operating conditions	
Mixture	Air
Equivalence ratio	0
Inlet mass flow rate	2.01 $g.s^{-1}$
Inlet temperature	298 K
Bluff body temperature	Adiabatic
HW velocity	5 $m.s^{-1}$
Mesh	Coarse

Table 4.3: Main conditions of NR simulation.

In accordance with the geometry and the absence of any significant sources of tangential or radial components, the axial velocity is predominant. To examine the flow field structure, it is useful to analyze Fig. 4.6, which provides the time-averaged contour of the axial velocity component for both experiments (left) and NR simulation (right). The range and the colormap of the contours are chosen in order to highlight the recirculation zones in blue and regions characterized by positive velocities in red. In addition, black velocity streamlines are superimposed on the contours, allowing for the identification of the different flow structures:

- The Outer Recirculation Zone is caused by the presence of the back plate and the chamber walls. Since this zone is characterized by a very low velocity, it is an ideal region for containing the ignition device in these operating conditions.

- The Annular Jet (AJ) is the region characterized by the highest axial velocities. Its interaction with the recirculation zones results in the generation of two Shear Layers (SL). During the combustion process, the SL promotes the stabilization of the flame, as it is characterized by high velocity gradients and turbulence levels.

- The Inner Recirculation Zone is created by flow separation due

to the presence of the bluff body. It is composed of two counter-rotating recirculation zones, enclosed within the annular jet, with an axial extension of approximately 25 mm. In reactive conditions this area enhances the mixing between combustion products and the reactant mixture, facilitating the maintenance of the combustion process.

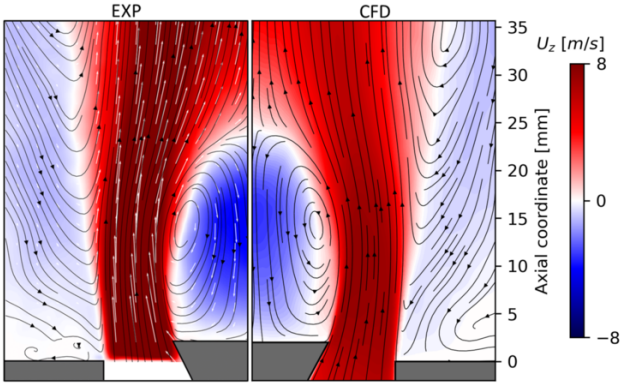

Figure 4.6: Experimental (left) and numerical (right) time-averaged axial velocity flow field.

A preliminary qualitative comparison between the experimental and numerical results can be obtained by examining Fig. 4.6 and the mean strain rate κ contours presented in Fig. 4.7. Starting from Fig. 4.6, the numerical prediction of the axial velocity exhibits an overall remarkable agreement with the experimental results. The streamwise extension of the IRZ is accurately reproduced and both the ORZ and the AJ are consistent with what is observed experimentally, in terms of configuration and intensity.

The strain rate is calculated as the derivative of the axial velocity with respect to the radial coordinate of the combustion chamber (Eq. 4.1) and it plays an important role in the ignition dynamic, as explained in [64]. In particular, as illustrated in the next section, elevated strain rate regions can cause local flame extinctions and consequently the impossibility of

the flame to penetrate the SL.

$$\kappa = \frac{\partial U_z}{\partial r} \tag{4.1}$$

With regards to the strain rate results (Fig. 4.7), it is possible to observe a satisfactory agreement although a slight underestimation can be noted at higher axial coordinates. As expected, higher values are detected at the inner and outer shear layers, in which the velocity gradients are predominant.

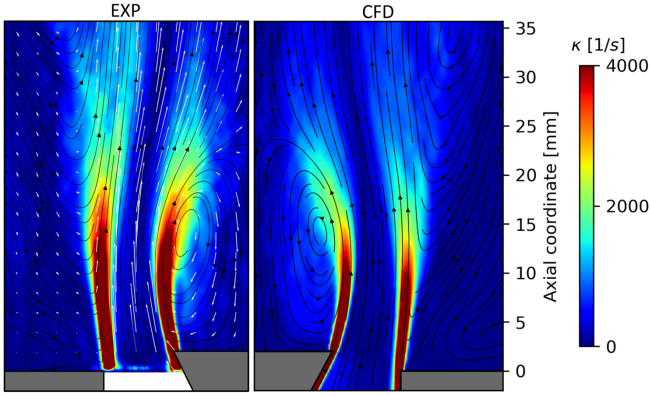

Figure 4.7: Experimental (left) and numerical (right) time-averaged strain rate field.

In order to achieve a more accurate evaluation, it is opportune to compare the time-averaged and RMS of the axial velocity profiles with those obtained experimentally by employing the PIV technique. The available profiles are measured at different locations above the chamber back plate. The comparison in terms of time-averaged axial velocity profiles (Fig. 4.8a) confirms the correct prediction of the mean flow field, particularly at low axial coordinates (5 and 11 mm) where the results are almost perfectly matched. The peak of the velocity in the AJ is well captured, even if the jet opening and the intensity of the IRZ are slightly overestimated.

The RMS profiles of the axial velocity (Fig. 4.8b) reveal an underestimation at all locations, although the trend is comparable and in line with the experimental results.

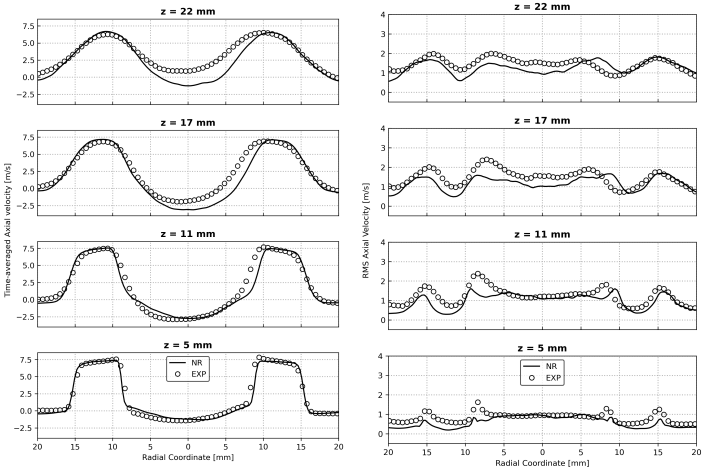

(a) Time-averaged *(b) RMS*

Figure 4.8: Comparison between numerical and experimental data at different streamwise locations in terms of time-averaged (left) and RMS (right) of axial velocity.

As explained in section 4.2.2, the entire domain, including the two opposite inlet ducts, is considered in the computational grid. This approach does not introduce any artificial turbulence into the domain, allowing it to naturally generate in the plenum upstream of the grid. Therefore, the underestimation of the turbulence level inside the combustion chamber is probably related to the numerical dissipation. In fact, although the grid size is kept constant at 400 µm for the entire axial extension of this zone (approximately 250 mm), it may not be sufficient to retrieve the proper value inside the chamber. Fig. 4.9 illustrates a contour of the instantaneous axial velocity (left) and velocity magnitude (right) in the region where the turbulence develops due to the opposite jets. During

the passage through the domain, the downstream turbulence grid and the converging duct contribute to uniform the flow field and thus, to reduce the turbulence intensity. In this context, several LES simulations are performed to investigate the impact of different levels of mesh refinement or injection strategies. However, the aforementioned approach is selected as it provides satisfactory values of turbulent fluctuations while maintaining a reasonable computational cost.

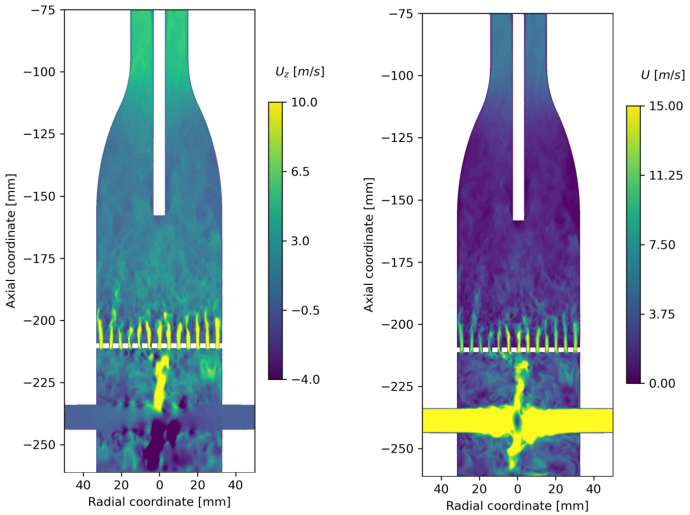

(a) Axial velocity *(b) Velocity magnitude*

Figure 4.9: Instantaneous contours of axial velocity (left) and velocity magnitude (right) on the midplane.

In conclusion, in order to evaluate the mesh quality, the index proposed by Celik [140] is reported in Fig. 4.10. Inside the combustion chamber, it is possible to easily identify the change in the mesh size and the consequent decrease in the Celik index. However, it assumes values greater than 0.9 in the entire domain, demonstrating that the dimension of the computational grid is sufficient to resolve at least 80% of the turbulent kinetic energy.

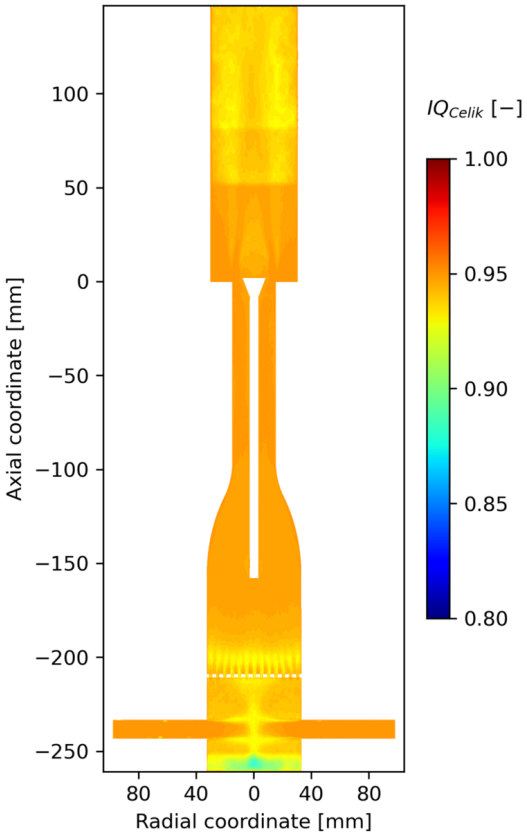

Figure 4.10: Contour of time-averaged Celik index on the midplane.

4.3.2 Ignition dynamics

In this section, the results of the soft ignition simulations with the primary objective of analyzing the ignition process and validating the numerical setup by comparing the solutions with the available experimental data, are presented. A summary of the main conditions of the simulations performed is reported in Tab. 4.4.

	R2	**R3S**	**R6Sr**
Mixture	H_2-Air	H_2-Air	H_2-Air
Equivalence ratio	0.43	0.43	0.43
Inlet mass flow rate	1.716 g.s^{-1}	1.716 g.s^{-1}	1.716 g.s^{-1}
Inlet temperature	298 K	298 K	298 K
Bluff body temperature	470 K	470 K	470 K
HW velocity	5 m.s^{-1}	5 m.s^{-1}	5 m.s^{-1}
Soret effect	×	✓	✓
Mesh	Coarse	Coarse	Refined

Table 4.4: Main conditions of the soft ignition simulations.

4.3.2.1 Flow dynamics at spark time

Prior to introducing the ignition dynamic and the comparison with the experimental data, it is important to examine the cold flow fields at the instant of the spark release (t = 0 ms), before the triggering of reactions, in order to isolate the effect of thermal diffusion. In fact, when the combustion process takes place, the Soret effect is enhanced by greater temperature gradients and the occurrence of preferential diffusion effects leads to a challenging identification. To clearly visualize the impact of the Soret effect, it is useful to refer to Fig. 4.11, which provides the instantaneous temperature and equivalence ratio fields for R2 (top row) and R3S (bottom row). Although both simulations show a temperature gradient in the IRZ due to the preheating of the bluff body, de-mixing effects are only observed in R3S with the formation of rich and lean spots with respect to the nominal value of 0.43. However, the impact of this effect is limited, as evidenced by the narrow range of the ϕ contours,

because the magnitude of the temperature gradients is small. Finally, it is important to note that these effects mainly occur in the IRZ, while the outer recirculation zone remains almost unaffected. On the contrary, in R2 a uniform equivalence ratio field is present in the entire domain.

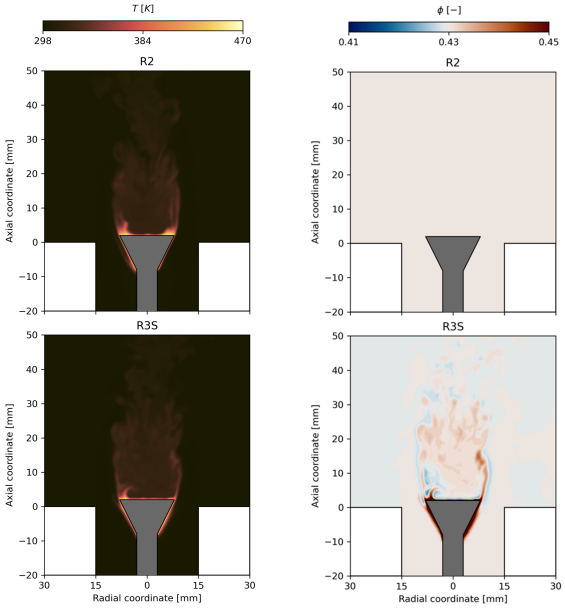

Figure 4.11: Instantaneous contours at $t = 0$ ms of temperature and equivalence ratio for R2 (top row) and R3S (bottom row).

It is also necessary to consider the conditions under which the spark occurs have a crucial impact on the development of the solution. In this context, the instantaneous contour of the axial velocity, reported on the left side Fig. 4.12, allows to visualize the overall conditions of the flow field at the spark time for R2 and R3S. The spark location is indicated by a dashed black circle.

The local state near the spark position can be analyzed by referring to the right side of Fig. 4.12, in which the PDFs of the axial and radial velocity

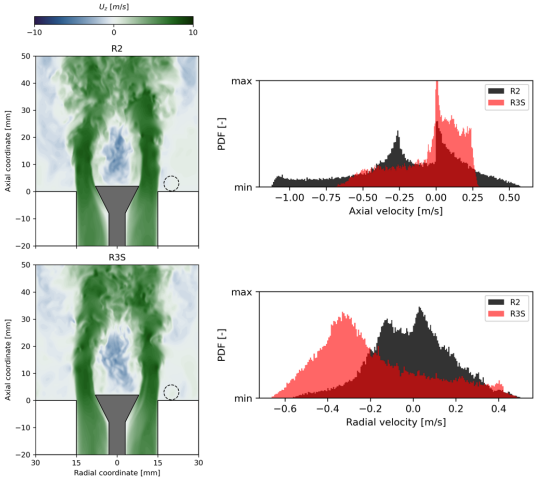

Figure 4.12: Instantaneous contours of axial velocity for R2 and R3S (left). PDF of axial (top) and radial (bottom) velocity component (right).

components are represented. The plots are obtained by considering the values of the velocity components on a sphere with a radius of 3 mm, centered at the spark position and sampled for approximately 4 ms before the ignition time. As expected, the two cases exhibit different PDF distributions both in terms of axial and radial velocity even if the variations are limited due to the low Reynolds number of the rig (Re ≈ 7000).

4.3.2.2 From kernel to flame stabilization

The complete ignition sequence is visualized through a 3D flame visualization in a top ad isometric view of an isosurface of HRR (10^8 W.m^{-3}) colored by temperature for R2 case in Fig. 4.13. In order to examine the ignition sequence, the instantaneous contours of the OH mass fraction normalized with the maximum value are reported on a longitudinal xz-plane and on a transversal xy-plane at a height of 9 mm from the chamber back plate, respectively in Fig. 4.14 and Fig. 4.15. This

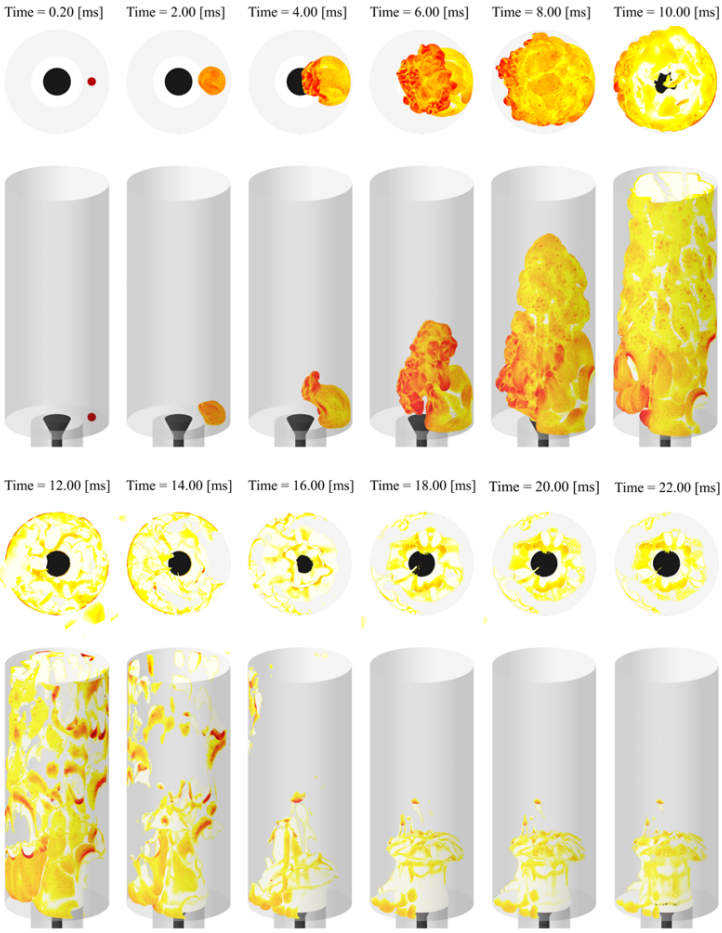

Figure 4.13: 3D flame visualization using an isosurface of HRR (10^8 $W.m^{-3}$) colored by temperature for R2.

allows the visualization of the ignition sequence from the spark time (t = 0 ms) until the chamber is completely ignited (t ≈ 22 ms). It is important to underline that only the contours relative to R2 are presented. In fact, R3S is used for a direct comparison with the experimental data since it considers the thermal diffusion effect and, therefore, is more representative of the physical phenomena, as highlighted in the next section.

At t = 0 ms, the energy deposited and the favorable conditions in terms of composition and flow field result in the formation of the kernel that tends to grow and propagate in the ORZ. The preliminary spherical growth is distorted due to the effects of the non-stationary flow field and the interaction with the turbulent structures (t = 2 ms). In this initial phase, the flame propagates mainly upward and in the tangential direction inside the ORZ, as highlighted in both contours at t = 4 ms. This behavior is attributed to the interaction with the highest strain region, which occurs at the edge of the back plate, forcing the flame to cross the annular jet and approach the IRZ from a further downstream location (t = 6 ms). Therefore, once the flame penetrates the shear layers, it tends to propagate and ignite the IRZ (t = 6-8 ms). This effect is more important at smaller streamwise distances from the back plate since downstream the annular jet tends to lose coherence and, as a result of the reduction of strain levels, the flame can propagate in all directions. At the same time, the flame continues to propagate in a symmetric circumferential direction as there is no major tangential velocity component (e.g. a swirled component), as can be observed from 8 to 12 ms in the transversal planes. Finally, when a large part of the mixture in the chamber is ignited, the complete anchorage to the back plate results in the stabilization of the combustion process (from t = 12 to 22 ms).

4.3.2.3 Impact of Soret effects

In order to assess the impact of the Soret effects, the ignition dynamics of R2 and R3S are compared. The time-series signal of the thermal power of the rig, calculated in the numerical simulations as the volume integral of the HRR per unit volume, is reported in Fig. 4.16 in which it is

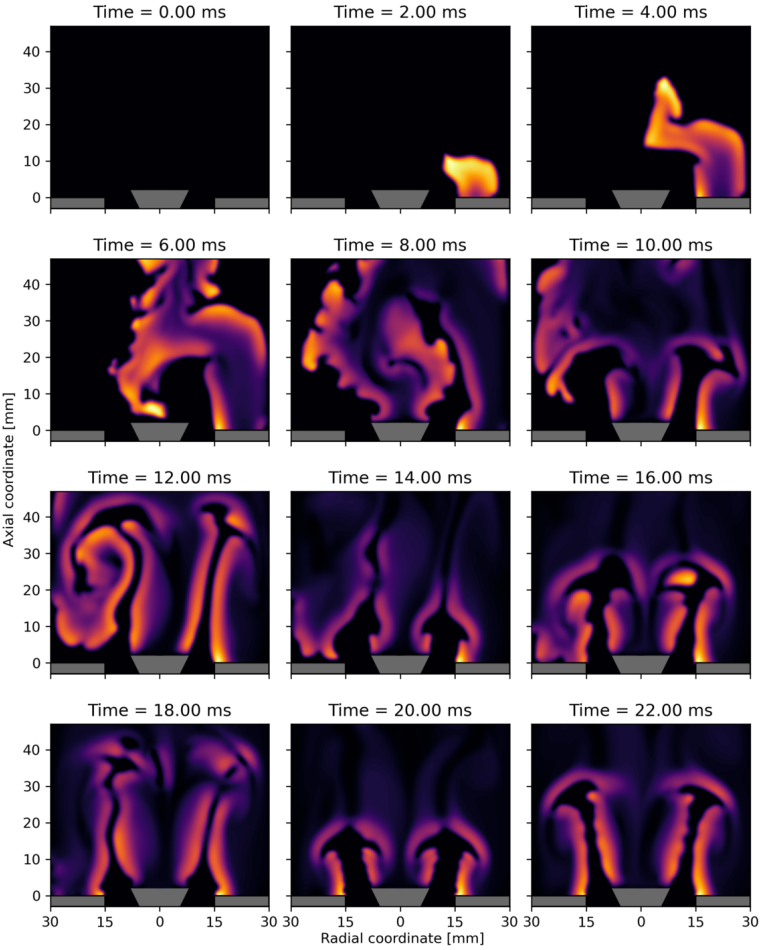

Figure 4.14: Instantaneous contours of the normalized OH mass fraction on the midplane for different instants of time (R2).

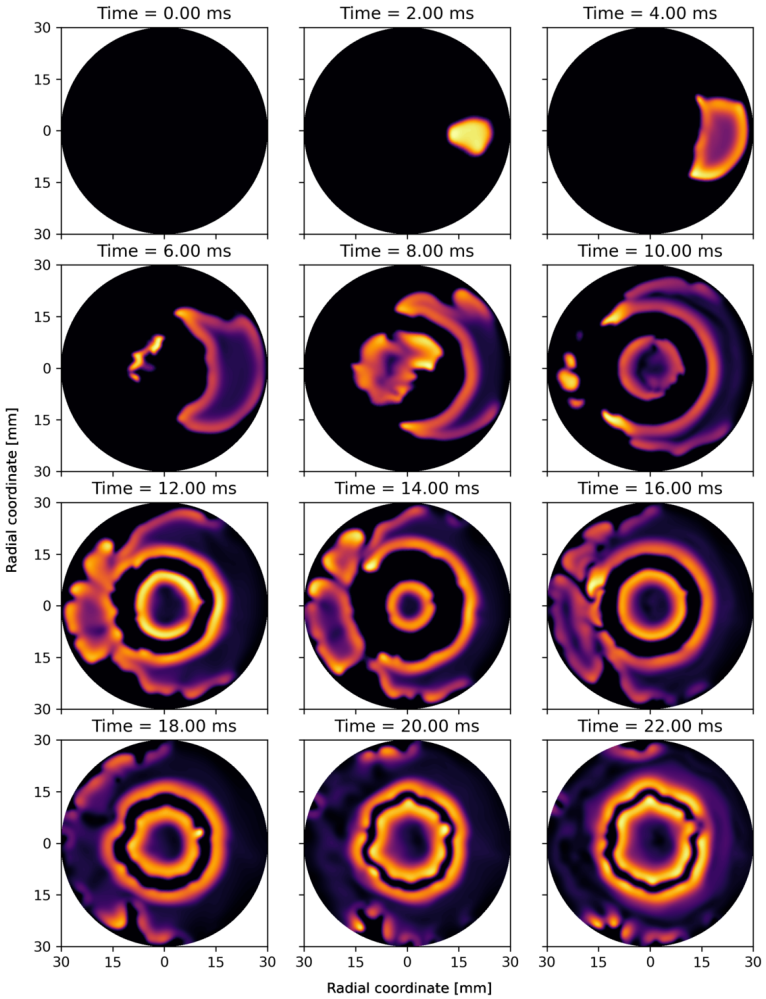

Figure 4.15: Instantaneous contours of the normalized OH mass fraction on a transversal plane at an axial coordinate of 9 mm from the chamber back plate, for different instants of time (R2).

possible to observe that the complete ignition of the chamber is achieved in approximately 22 ms. In fact, when the stable conditions are reached, the power oscillates around the nominal value ($\approx$ 5.7 kW), determined by the product of the fuel mass flow rate and the lower heating value of hydrogen. The time signal for R6Sr simulation, which is introduced in the next section, is also included in the plot with the purpose of providing an additional signal given the stochastic nature of the phenomenon. It is possible to notice a slightly faster ignition, underlined by the shift of the curves towards lower times and a higher maximum power when thermal diffusion is included. These effects are attributed to the local increase in fuel mass fraction at the flame front, which enhances the flame speed, as explained in Sec. 2.2.3.

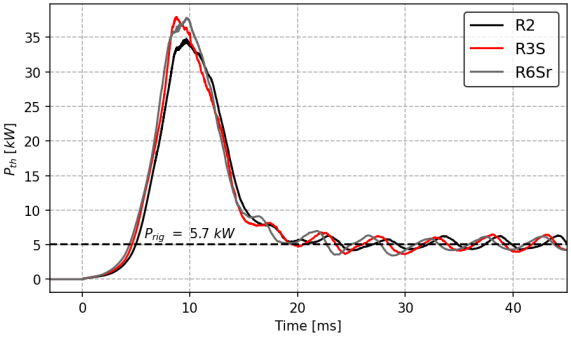

Figure 4.16: Thermal power as a function of time for R2, R3S and R6Sr with the nominal thermal power represented by the black dashed line.

In order to provide a more comprehensive understanding of the aforementioned considerations, it is useful to refer to Fig. 4.17, which illustrates the instantaneous contours of the equivalence ratio for R2 (top row) and R3S (bottom row). The selected instants of time are representative of the ignition dynamic that is discussed in detail in the next section. In reference to R2, the redistribution of the equivalence ratio due to the preferential diffusion is evident. In particular, it is possible to observe the mixture leaning upstream of the flame front, while a local enrichment is

present on the burnt mixture side. Considering R3S, an increase in the local equivalence ratio gradient is retrieved which is caused by thermal diffusion, since the lighter species as hydrogen tend to diffuse towards higher temperature zones.

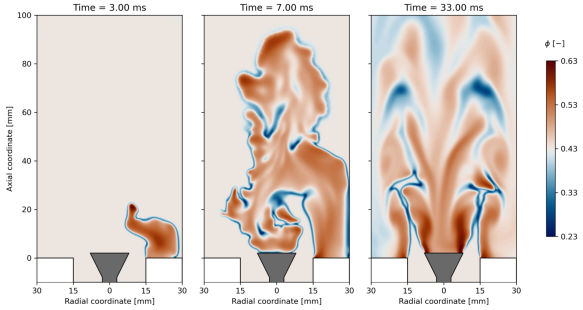

(a) R2

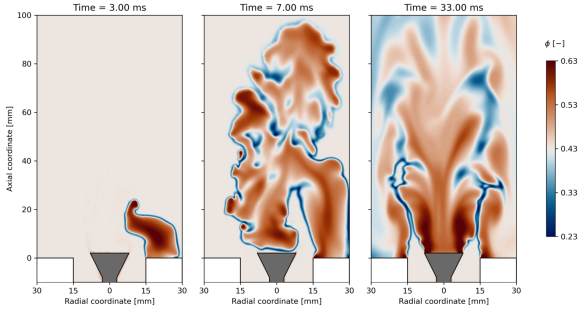

(b) R3S

Figure 4.17: Instantaneous contours of equivalence ratio for R2 (top row) and R3S (bottom row) at different instant of time.

As mentioned several times, the consequences of these phenomena lead to temperature variations associated with the change in stoichiometry, as shown in Fig. 4.18. Furthermore, the higher burning rate in the R3S case can be observed at 7 ms. In fact, at the same instant of time, the combustion process involves a larger part of the chamber and this is related to the enhanced flame propagation speeds caused by the Soret

effect.

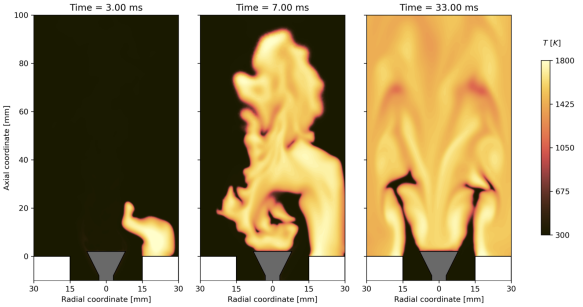

(a) R2

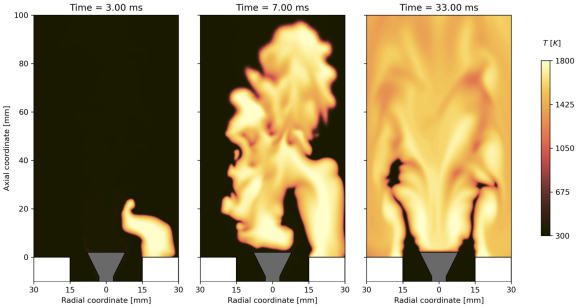

(b) R3S

Figure 4.18: Instantaneous contours of temperature for R2 (top row) and R3S (bottom row) at different instant of time.

4.3.2.4 Comparison with experimental data

In the previous section, a general description of the ignition dynamics is provided, highlighting the main steps of the process. In this section, a comparison with the experimental results is conducted by employing the images achieved with the PIV technique coupled to the OH-PLIF, during the ignition process. This approach enables the simultaneous acquisition of information regarding the flame and the velocity flow field. The availability of detailed experimental data allows for a comprehensive

analysis of the four phases in which the ignition sequence for this case can be mainly divided:

- Kernel growth in the ORZ
- Flame-jet interaction
- Flame development in the IRZ
- Flame-anchoring process.

As previously mentioned, the comparison with the experimental data is conducted by referring to the results of the R3S simulation and in the following, only this setup is considered. It is mandatory to recall that the ignition process is a stochastic event and, in this study, only a single run is analyzed for both CFD and experimental data. Therefore, the comparison aims only to provide a qualitative assessment of the main stages observed during the ignition.

Kernel growth in the ORZ

The kernel growth within the ORZ is described by referring to Fig. 4.19, where the numerical and experimental results are reported in the first and second rows, respectively. The flow field is identified by the vector plots, which are coloured by the planar velocity magnitude ranging from 0 to 8 $m.s^{-1}$, according to the experimental maps. In addition, white isolines of zero axial velocity are superimposed to facilitate the identification of the recirculation zones. The flame is identified by normalizing the OH mass fraction with its maximum value. It is important to note that the experimental data are not accessible in proximity to the back plate wall, as a result of laser reflections that compromise the measurement. Moreover, although the laser sheet is aligned with the spark plug in the combustion chamber, the kernel may arise in a different tangential position. For these reasons, the kernel is not fully represented in the experimental maps. The spark occurs at t = 0 ms, leading to the formation of a spherical kernel that can grow in the ORZ due to the low velocity and turbulence levels. After approximately 1 ms from the spark, the kernel starts to interact

with the SL of the annular jet.

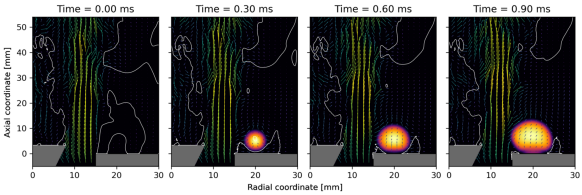

(a) R3S

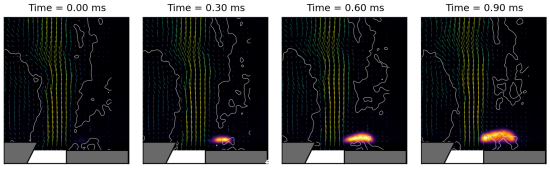

(b) EXP

Figure 4.19: Instantaneous contours of normalized OH mass fraction with overlapped velocity vectors and white isolines of zero axial velocity. Numerical results of R3S (top row) and experimental PIV/OH-PLIF data (bottom row).

Flame-jet interaction

After the kernel growth, the flame-jet interaction dynamic is presented. This phase occurs approximately between 1 and 4 ms, as reported in Fig. 4.20, and it determines the duration of the entire process. In fact, as evidenced in [147], one of the major distinctions between hydrogen and methane dynamics is the different penetration length of the flame in the annular jet. By comparing the numerical and the experimental maps, it is possible to observe the lack of penetration near the edge of the back plate. This is related to the presence of elevated velocity and strain rate values in this region, causing the local flame propagation in the axial and tangential direction. When the flame reaches downstream regions characterized by lower strain rate values, it can penetrate the annular jet. Despite the slight underestimation of turbulence and strain

rate levels observed with respect to the cold flow, the consistency with the experimental results is evident, both in terms of penetration depth (approximately 20 mm) and flame shape.

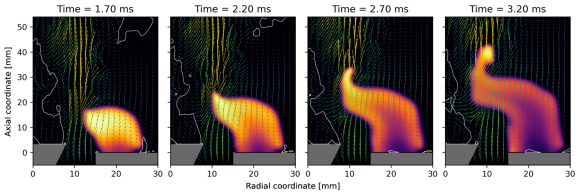

(a) R3S

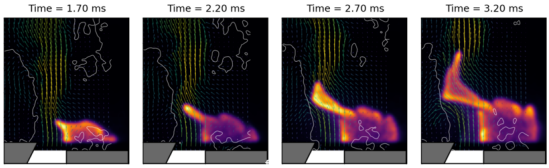

(b) EXP

Figure 4.20: Instantaneous contours of normalized OH mass fraction with overlapped velocity vectors and white isolines of zero axial velocity. Numerical results of R3S (top row) and experimental PIV/OH-PLIF data (bottom row).

Flame development in the IRZ

As a consequence of the annular jet crossing, the flame approaches the IRZ. With reference to Fig. 4.21, it is possible to observe that the penetration heights obtained with the numerical and experimental procedure are almost equal, suggesting that the strain rate levels are comparable. In fact, in this plane, the flame exhibits a predominantly longitudinal development at the outer shear layer, for an axial distance of approximately 20 mm. The reduction in the axial extension of the IRZ, evidenced by the white isoline of zero axial velocity, is well retrieved from the simulation. The combustion process in the IRZ occurs at around 5.4 ms and a slight delay can be observed in the numerical simulation. Indeed, at 6.4 ms the flame

is not still anchored to the bluff body, differently from the experimental scenario. This time delay is probably related to the non-stationary phenomena that contribute to the stochasticity of the ignition process.

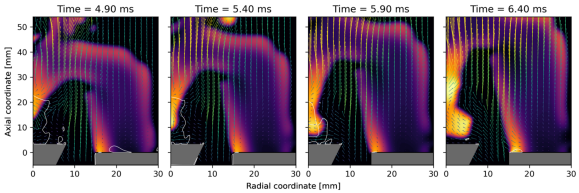

(a) R3S

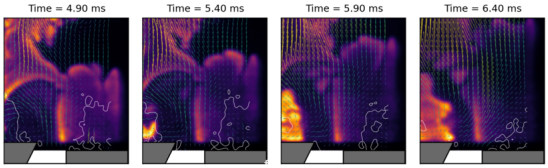

(b) EXP

Figure 4.21: Instantaneous contours of normalized OH mass fraction with overlapped velocity vectors and white isolines of zero axial velocity. Numerical results of R3S (top row) and experimental PIV/OH-PLIF data (bottom row).

Flame-anchoring process

The last phase is the flame-anchoring process. In order to achieve the stabilization condition, the flame must propagate and anchor on the entire ORZ, as described in the previous section (Fig. 4.15 from 10 to 22 ms). Unfortunately, since the experimental data on the specular plane are not available, a direct comparison is not feasible in terms of PIV/OH-PLIF. Therefore, in Fig. 4.22, the flame evolution from 8.5 to 10 ms is provided in order to analyze the flame dynamic during the last part of the ignition sequence. The numerical flame tip behavior is probably related to the different directions of the velocity vectors in this region, compared to the experimental ones. The agreement is confirmed in terms of length and

shape of the flame. Both numerical and experimental cases reveal an OH peak at the inner and outer shear layers, where the velocity gradients and the strain rate are elevated. Furthermore, the intensity of OH in this area is comparable, although the normalization procedure is performed in relation to a different maximum value. It is also important to recall that the adiabatic condition is applied to all solid walls, except for the bluff body. In reality, the heat loss effects could locally quench the flame at the back plate tip, where the maximum concentration of OH is instead detected. To conclude, it is also interesting to note that both IRZ and ORZ begin to increase in axial extension after the flame passes.

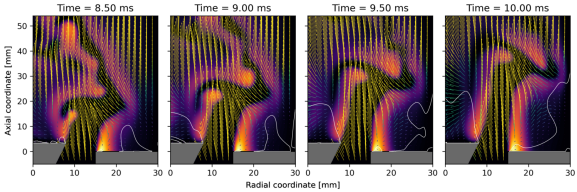

(a) R3S

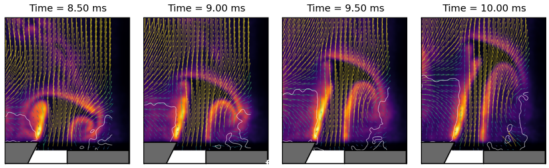

(b) EXP

Figure 4.22: Instantaneous contours of normalized OH mass fraction with overlapped velocity vectors and white isolines of zero axial velocity. Numerical results of R3S (top row) and experimental PIV/OH-PLIF data (bottom row).

4.3.2.5 Impact of spatial resolution

In the previous sections, in order to validate the numerical results with the experimental data, a qualitative comparison is performed since the

time snapshots of a single run are analyzed. Therefore, to demonstrate the reliability of the numerical results, the pressure signals recorded in the combustion chamber (M4) and in the duct (M1 and M2) are presented in the top part of Fig. 4.23. The experimental data are obtained by averaging a minimum of 10 tests, with the aim of verifying the repeatability of the procedure, and are low-pass filtered at 200 Hz. For a proper comparison, the same filtering processing is applied to the numerical results, which conversely are representative of a single run each. At this stage, only the R3S and R6Sr simulations are reported since both of them are carried out with the inclusion Soret effect but on different mesh grids, which is the last point to be evaluated. To clearly visualize the pressure behavior, the filtered contours of the pressure at 200 Hz for R3S are reported in the bottom part of Fig. 4.23.

Regarding the M4 signal, it can be noted that when the spark is released (t = 0 ms), the pressure is almost constant. The increase in temperature and the thermal expansion of the burnt mixture cause a rise in the chamber pressure, inducing the gases to accelerate towards the outlet. This results in a rapid drop in pressure until the negative peak is reached (t $\approx$ 11 ms). Then, a stable condition is achieved and the pressure oscillates around the initial value with a frequency of 170-180 Hz, as better explained in the next section. With the R3S simulation the over pressure is accurately replicated in terms of magnitude and time shift with respect to the spark time. In fact, the rate of pressure increase/decrease is in good agreement with the experimental data until approximately 10 ms. Then, the negative pressure peak exhibits a lower intensity and a time delay compared to the experimental results. Moreover, the same conclusions can be drawn for M1 and M2 signals, in which a slight overestimation of the pressure peaks is observed. For these reasons, the simulation R6Sr is carried out where the grid refinements allow to better discretize the exhaust gas acceleration, resulting in a major agreement with the time signals at all locations. In any case, it is important to underline that both grids can accurately predict the overall behavior of the flame. However, for a more accurate reconstruction of pressure signals, the refined grid is

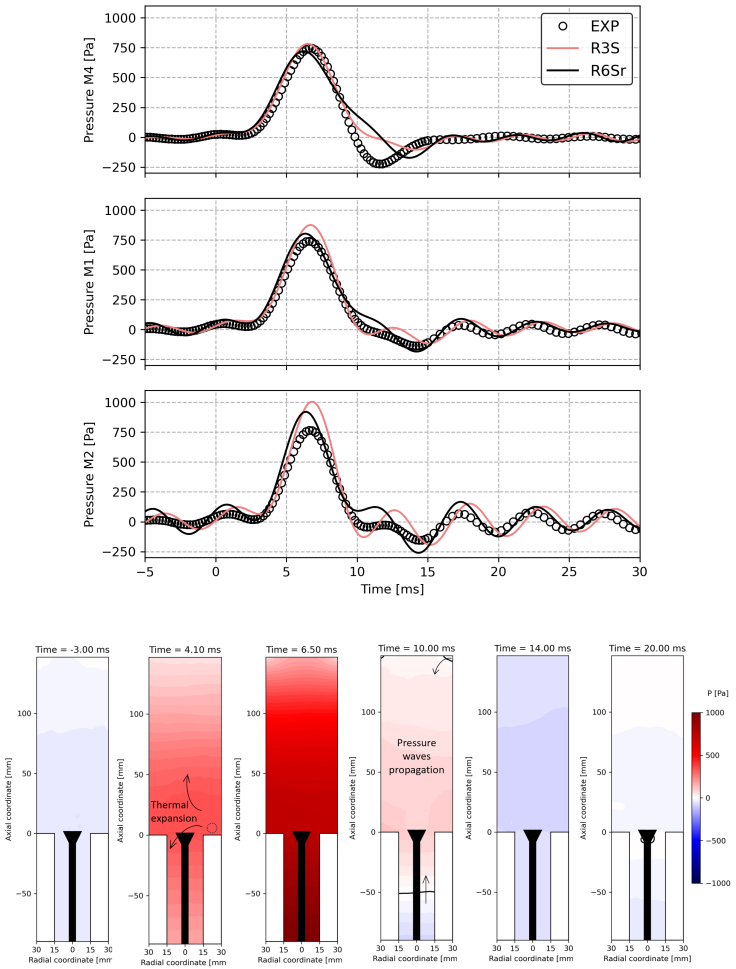

Figure 4.23: (Top) Pressure signal measured at the chamber back plate (M4) and with the two probes inside the duct (M1 and M2). Both numerical (R3S and R6Sr) and experimental results are filtered at 200 Hz. (Bottom) Contours of filtered pressure at the same frequency on the midplane for R3S.

necessary. Therefore, subsequent analyses are referred to the refined grid.

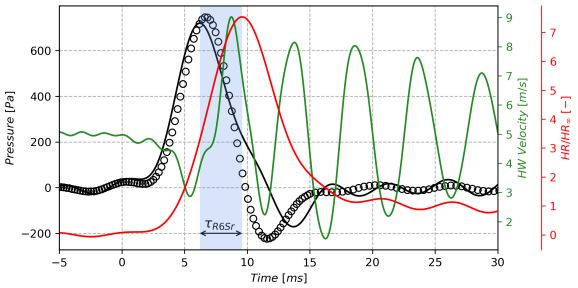

Figure 4.24: Pressure signal measured at the chamber back plate (M4), normalized thermal power and velocity at HW location for R6Sr. Pressure and thermal power are filtered at 200 Hz. Velocity signal is filtered at 600 Hz.

To conclude the investigation of the soft ignition case, the pressure signal measured at the chamber back plate, the normalized thermal power and the velocity and the HW location are reported in Fig. 4.24 for R6Sr. A key aspect observed experimentally is the time lag between the pressure and heat release rate peaks. In particular, as highlighted in [30], when the time lag is greater than a critical value τ_c of approximately 1 ms, the flashback scenario may not occur. This experimental evaluation is numerically confirmed, as the time delay is $\tau_{\mathrm{R6Sr}} \approx 4$ ms. Furthermore, to bridge the experimental gap due to the lack of HW measurements for fully hydrogen flames, the velocity time signal is also presented. Despite its reduction after the spark, the velocity remains always positive reaching a minimum value of 2.8 $\mathrm{m.s^{-1}}$ at approximately t = 5 ms. According to the pressure signal, when stable conditions are reached the velocity starts to oscillate around the nominal value with the same frequency.

4.3.3 Stable flame results

In this section, the stable flame condition is analyzed. Starting from the previous ignition simulations, when stable conditions in terms of pressure, velocity and heat release rate are reached, an averaging procedure is operated in order to obtain a statistical convergence solution, necessary for the comparison with the experimental data. Initially, the flow field is investigated. Subsequently, comparisons between the simulations are presented and finally, the flame structure is examined by referring to the experimental results.

4.3.3.1 Reactive flow field

The numerical time-averaged axial flow field for R6Sr is reported in Fig. 4.25 (right) where it is compared with the experimental results (left) obtained through the PIV technique. As expected, the decrease in density caused by the combustion process leads to higher values than those observed in the cold flow field (Sec. 4.3.1). However, the prediction of the ORZ and the IRZ is consistent in terms of extension and velocity magnitude and the overall agreement is remarkable.

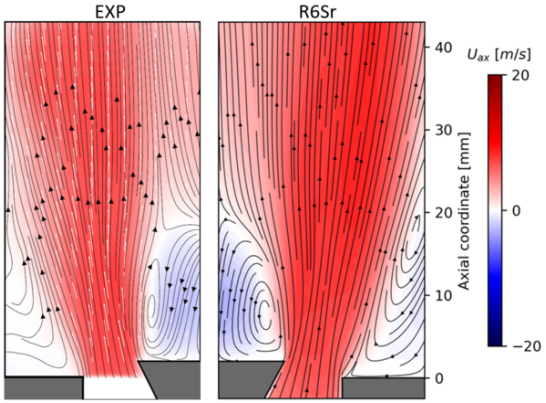

Figure 4.25: Experimental (left) and numerical time-averaged axial flow field for R6Sr (right).

4.3.3.2 Flame structure

Experimental images of stable flame are obtained by the time-averaged OH^* chemiluminescence and OH-PLIF techniques. Starting with the OH-PLIF, a comparison between numerical and experimental results is presented in Fig. 4.26, since the OH species is included in the employed reaction mechanism. The experimental contour shows horizontal bands with different light intensities, related to the laser intensity distribution. Since experimental and numerical images are normalized with respect to their relative maximum values, only a qualitative comparison in terms of mean flame shape is carried out. As previously mentioned, laser technology prevents the acquisition of data in proximity to solid walls, explaining the black band present in the experimental flame. The numerical prediction of R6Sr exhibits OH peaks at the inner and outer shear layers, according to the higher levels of stretch in these regions, where the flame is attached at the back plate due to the adiabatic treatment imposed. However, the heat losses generated by the finite wall temperature of the bluff body cause a local quenching and the consequent lift-off of the flame on the inner shear layer according to the experimental map. Furthermore, the inclusion of the Soret effect determines a local peak of reactivity also in these regions, confirming its local impact.

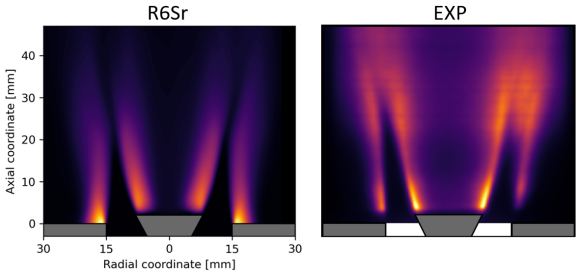

Figure 4.26: Time-averaged contours of OH mass fraction for R6Sr (left) and mean flame images obtained with the OH-PLIF technique (right) normalized with the relative maximum value.

A more accurate visualization of the flame structure can be achieved

using the chemiluminescence technique since the OH^* allows for a reliable identification of the position of the flame front. Since the OH^* species is not included in the reaction mechanism used in the simulations, the comparison is achieved in terms of Line-Of-Sight (LOS) of heat release rate. This allows to obtain comparable results with the OH^* distribution, particularly in a perfectly premixed configuration, as explained in [64]. Even in this case, maps are normalized with the relative maximum. The M-shaped flame is correctly predicted by the numerical simulation, also in terms of length, suggesting that the turbulence levels entering the chamber exhibit good agreement.

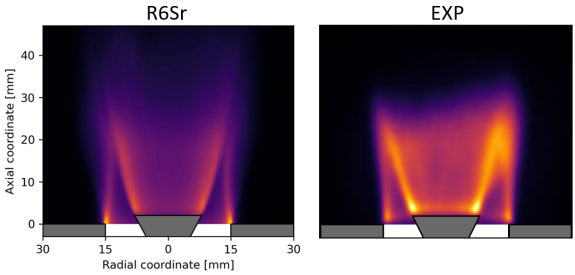

Figure 4.27: LOS of heat release rate for R6Sr (left) and mean flame images obtained with the OH^* chemiluminescence technique (right) normalized with the relative maximum value.

As previously mentioned, during stable conditions the flame oscillates in the axial direction due to the acoustic response of the test rig at a frequency of 170-180 Hz. To further investigate this behavior the flame images obtained in the experimental context through the OH-PLIF technique (right) and the numerical contours of the normalized OH mass fraction on a longitudinal plane for R6Sr (left) are reported in Fig. 4.28 for a complete oscillation period. It is possible to observe that at t = 20 ms the flame has a shorter length resulting in a reduction in the flame front surface and therefore in the thermal power, in accordance with the results shown in Fig. 4.16. Conversely, the flame surface and the thermal power increase at approximately 23 ms, where the flame length is greater.

The oscillations are accurately predicted in terms of shape and length of the flame and in terms of frequency, confirming the reliability of the numerical models employed.

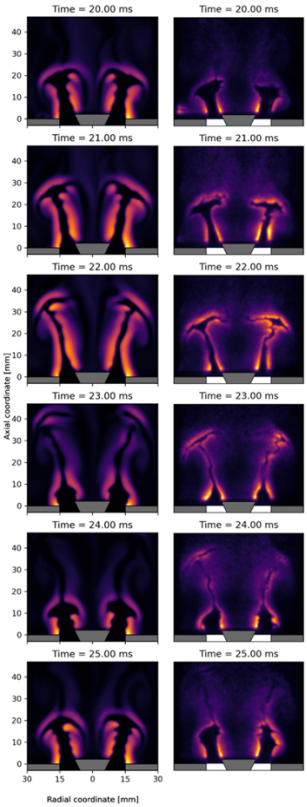

Figure 4.28: Instantaneous contours of the normalized OH mass fraction on the midplane for R6Sr (left) and instantaneous flame images obtained with the OH-PLIF technique (right) for different instants of time.

Figure 4.29: 3D flame visualization using an isosurface of HRR (10^8 $W.m^{-3}$) colored by temperature for FB1Sr.

4.3.4 Flashback dynamics

The second case with the Plate25 operating under the same conditions ($U_b = 5$ m.s^{-1} and $\phi = 0.43$) is here considered. Confirming the experimental observations, a permanent flashback scenario is obtained from the FB1Sr simulation, as reported in Fig. 4.29. To better investigate the flashback dynamics, Fig. 4.30 shows contours of instantaneous heat release rate at five relevant time snapshots. In fact, despite the small back pressure introduced by the Plate25 (≈ 70 Pa), the ignition dynamics change drastically [30]. In the first 2.2 ms the kernel grows as in the soft ignition case. However, after this point, due to the local flow conditions, the flame interacts with the boundary layer (t = 5.0 ms) as detailed in the next section. Then, the flame propagates upstream inside the injector until the pressure fluctuations, generated after the ignition, partially expel it from the confined duct (t = 9.4 ÷ 14.6 ms). Finally, the flame reaches a stable configuration anchored inside the injector as illustrated in the last contour map at t = 31.3 ms.

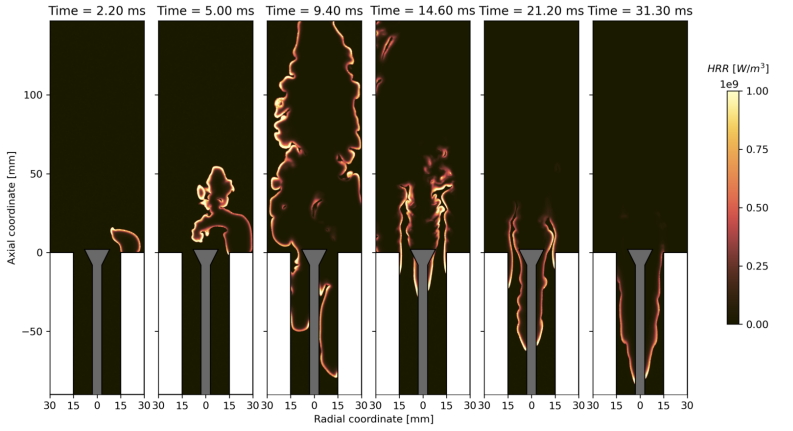

Figure 4.30: Instantaneous contours of heat release rate for different significant instants for FB1Sr.

To first validate the results, the velocity at the HW location, nor-

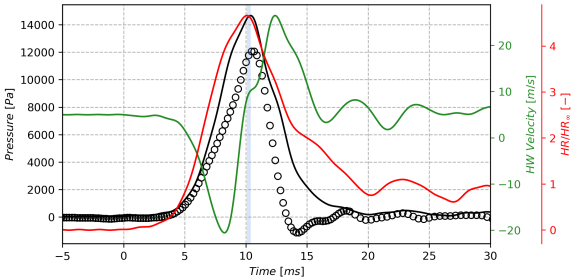

Figure 4.31: Pressure signal measured at the chamber back plate (M4), normalized thermal power and velocity at the HW location for FB1Sr filtered at 600 Hz.

malized thermal power and chamber pressure (M4) with the relative experimental data filtered at 600 Hz are shown in Fig. 4.31 for FB1Sr. With respect to the previous case without the outlet restriction, the pressure peak increases of an order of magnitude moving from 800 Pa to 12000 Pa. Positive and negative peaks are respectively overestimated and underestimated by the simulation although the timing is perfectly captured. Indeed, the time lag $\tau_{\mathrm{FB1Sr}} = 0.3$ ms is below the critical value τ_c, confirming the flashback occurrence. Contrarily, a different behavior in terms of velocity at the HW location is observed with respect to R6Sr. In particular, when the pressure inside the chamber increases, the velocity becomes negative with a minimum of -20 m.s^{-1}. Then, the partial blockage of the duct due to the flame presence leads to a mass accumulation in the upstream plenum. The mass flow rate is consequently discharged resulting in an increase of the velocity to a maximum value of 30 m.s^{-1}. Finally, the dynamics of the system is restored and the velocity stabilizes around the nominal value of $U_b = 5$ m.s^{-1}.

4.3.4.1 Trigger of the flashback

In this section, the transient behavior that leads to flashback compared to the soft ignition is investigated. During the first instants after the

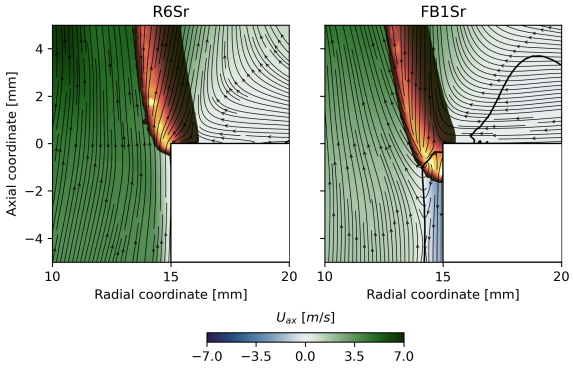

Figure 4.32: Instantaneous contours of velocity flow field for R6Sr and FB1Sr at t = 5 ms. Black isolines of zero axial velocity and heat release rate contours are superimposed.

release of the spark, the introduction of Plate25 at the outlet section generates a strong adverse pressure gradient. In fact, the pressure drop between the plenum and the combustion chamber increases from -60 Pa to approximately -1250 Pa due to the outlet restriction.

To analyze the effect of the different adverse pressure gradient on the ignition dynamics inside the injector, R6Sr and FB1Sr are compared at t = 5 ms in Fig. 4.32.

Black isolines of zero axial velocity and heat release rate contours are superimposed to instantaneous velocity contours and flow field streamlines, permitting to highlight both recirculation and reaction zones. In the R6Sr case, the pressure gradient generates only a slight reduction of the velocity magnitude without inducing a boundary layer separation. Furthermore, this implies higher radial velocity gradients at the inlet of the combustion chamber with respect to FB1Sr resulting in elevated strain rate values. Conversely, the stronger pressure gradient due to Plate25 causes a boundary layer separation in the injector regions up to the chamber inlet (right side of Fig. 4.32). The interaction between the flame front and the recirculation zone at the wall promotes upstream flame

propagation through the boundary layer. This phenomenon, coupled with the response of the system, generates a reverse flow inside the injector enabling the rise back of the flame approximately 70 mm upstream of the burner.

4.3.4.2 Flashback dynamics inside the injector

In a second phase, despite its previously mentioned partial ejection, the flame is unable to stabilize on the upper surface of the bluff body since the two branches remain confined and anchored in the inner and outer surfaces of the duct inside the injector, as shown in Fig. 4.33 at $t = 14.6$ ms. Moreover, the presence of burnt gas pockets in the regions upstream of the bluff body, which are convected inside the chamber by the flow field, and the heat losses caused by a finite wall temperature, further prevent the proper anchoring of the flame downstream the burner. The reduction in the velocity occurring between t = 14.6 ms to t = 21.2 ms creates the conditions that indeed facilitate the propagation through the injector.

It is interesting to highlight how only the inner branch of the flame is able to propagate back into the duct. As briefly explained, this behavior is related to the fact that the inner branch of the flame remains anchored in a more upstream position with respect to the outer one. The upstream propagation after t = 21.2 ms is in fact not caused by a bulk adverse pressure gradient (almost negligible at t = 21.2 ms), instead, it can be explained by referring to the boundary layer flashback mechanism proposed by Eichler and Sattelmayer in [57].

In this process, observed on the inner surface of the duct, the thermal expansion of burnt gases occurring at the flame front tip, determines a deflection of the streamlines inducing the local flow separation further promoting flame propagation. The mandatory requirement for the occurrence of this phenomenon is that the flame front curvature is convex towards the incoming fresh mixture, as highlighted in the zoomed contour in Fig. 4.33. This flashback mechanism does not conversely occur on the outer surface of the confined duct. In fact, the displacement of the streamlines caused

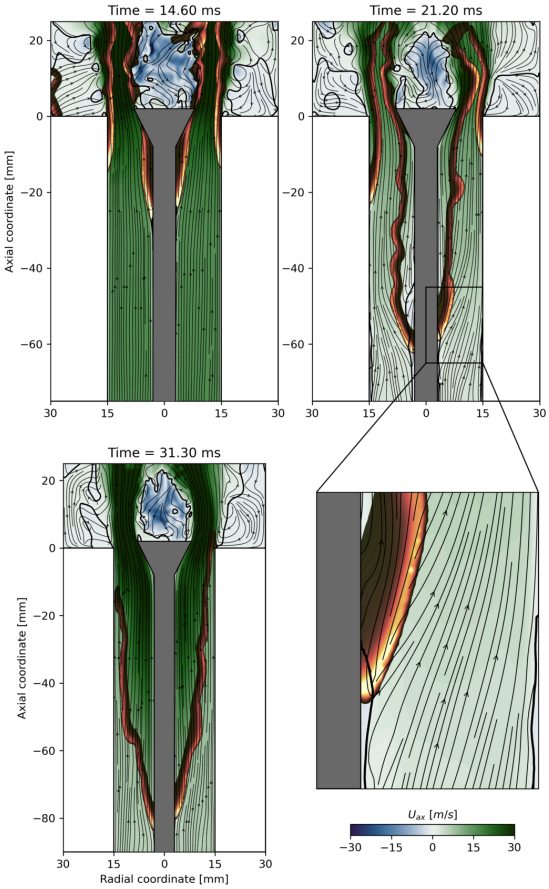

Figure 4.33: Contours of velocity flow field for FB1Sr at different instants of time. Black isolines of zero axial velocity and heat release rate contours are superimposed.

by the flame front anchored on the inner surface (located more upstream) determines also a flow acceleration that promotes the reattachment of the separated boundary layer on the outer surface preventing an effective local flashback. This phenomenon is clearly shown in Fig. 4.33 at t = 21.2 ms. In the subsequent phases, the wrinkling of the flame surface induces the connection of the two branches on a single flame front characterized by a trailing edge convex towards the burnt mixture. Once this condition is reached (t = 31.3 ms), a single V-shaped flame front is achieved which is no longer attached and anchored on the outer surface. This stable configuration allows all of the incoming fresh mixtures to be burned.

4.4 Final considerations

In this chapter, the full-ignition sequence from spark release to full flame development, up to proper stabilization or permanent flashback, is investigated with an LES-based numerical methodology. In this context, the atmospheric test rig installed at the Norwegian University of Science and Technology (NTNU) operating with a lean, perfectly premixed, hydrogen-air flame that stabilizes on a conical bluff body is considered. The experimental analysis carried out on the burner assesses the impact of the chamber back pressure as well as the effects of the hydrogen content in the ignition dynamics.

Initially, a non-reactive case with a pure air mixture is simulated with the purpose of analyzing and validating the flow field structure. The results are qualitatively and quantitatively compared with experimental data obtained using the PIV technique. Despite slight underestimations, the numerical results exhibit a remarkable agreement in terms of axial velocity, RMS and strain rate levels.

Then, three ignition simulations, named R2, R3S and R6Sr, are conducted under identical conditions, with the exception of the Soret effect and the grid resolution. A detailed description of the ignition sequence is provided by a comparison with the flame images obtained through the coupled PIV/OH-PLIF techniques. According to the analysis,

the inclusion of thermal diffusion (R3S) results in a more pronounced redistribution of the equivalence ratio. This leads to the formation of regions that are richer or leaner than those predicted by R2. Furthermore, despite the overall behavior is consistent with the experimental data for all the calculations, the local pressure signals are accurately predicted only if refined sizing is maintained up to the combustion chamber exit (R6Sr).

The numerical setup employed is further validated by considering stable flame conditions. Time-averaged axial velocity component is evaluated and a marginal overestimation is observed when compared to the experimental PIV data. The structure of the flame is investigated by a comparative analysis with the images obtained through the time-averaged OH-PLIF and OH^* chemiluminescence. Based on the evaluation conducted, it can be concluded that the flame is correctly reproduced, both in terms of shape and length. Additionally, an analysis of the self-sustained fluctuations characterizing the flame reveals a frequency of 170-180 Hz, comparable to the experimental one.

Finally, by introducing a perforated plate at the outlet, a permanent flashback scenario is investigated and two different phases are identified. First, the initial adverse pressure gradient leads to a boundary layer separation that promotes the upstream propagation of the flame. Subsequently, when the nominal pressure gradient is restored, a boundary layer flashback mechanism is observed on the inner surface of the duct. The consequent deflection of the streamlines inside the confined duct induces the reattachment of the separated flow and prevents the propagation of the flame on the outer surface.

In conclusion, a methodology to explore the entire hydrogen ignition sequence is validated and the observation inside the injector permits to extend the experimental work and explain the underlying physical mechanisms.

Conclusions

The present research work investigates the hydrogen combustion dynamics paying particular attention to the ignition process from spark release to complete flame development through numerical high-fidelity Large Eddy Simulation approaches. The high reactivity and the fast diffusivity of hydrogen requires the assessment of numerical models, commonly used and tested for hydrocarbon fuels, to ensure a reliable and accurate prediction of the combustion process.

Particularly, when dealing with lean hydrogen-air mixtures, the inclusion of these effects in CFD modeling becomes imperative. In this context, the primitive variable approach employing a Thickened Flame Model serves as a commendable compromise between accuracy and computational efficiency. In fact, due to the relatively straightforward chemical kinetics of hydrogen compared to generic hydrocarbons, this approach allows for the utilization of accurate reaction mechanisms with a reduced number of species. Simultaneously, using a mixture-averaged approach for calculating diffusive fluxes proves to be nearly as effective as a more general and resource-expensive multicomponent approach. Furthermore, it is noteworthy that Soret effects influence flame propagation speed. These aspects are supported by a DNS investigation of laminar spherical expanding flames.

Since all previous considerations refer to analyses conducted under laminar conditions or through one-dimensional tools such as Cantera, the turbulent combustion models presented in Chapter 2, including the extended version of the FGM model, are tested on the burner experimen-

tally investigated at the Technische Universität Berlin. The main features of the examined flow field such as axial jet penetration and interaction with recirculation zones are more faithfully reconstructed with the experimental data if the grid used has localized refinement zones at the jet outlet. Therefore, in reactive analyses, the refined grid is used. Due to the technically premixed conditions under which the combustor operates, correct prediction of the mixing between air and fuel is critical for a proper flame prediction. The tabulated chemistry approach (FGM), in which the equations are solved under the unity-Lewis assumption, predicts a mixing field perfectly consistent with the primitive variable model (TFM) only within the mixing tube, where reactive processes do not take place. In fact, once the intensity of species and temperature gradients increases as a result of chemical reactions within the combustion chamber, the inclusion of preferential and thermal diffusion effects is critical under these operating conditions. However, although the time-averaged field of equivalence ratio between FGM and TFM is slightly different, locally there is a drastic effect on the conditions under which the reactions occur. In fact, although all models reconstruct the correct M-shape of the experimentally observed flame under these operating conditions, only the TFM approach succeeds in predicting the anchor point and the axial extension of the flame, resulting in a proper estimation of the reactive velocity field. Conversely, both the basic FGM approach and the extended version to account for stretch and heat loss effects E-FGM predict an extremely higher reactivity, resulting in a more compact flame and a significantly different thermal field. Therefore, in order to correctly predict the aerothermal field of a lean hydrogen flame, the primitive variable approach with a Thickened Flame Model is necessary although the computational cost is about 65% higher than an FGM approach (for the conditions tested).

Once the different modeling strategies for turbulent combustion are assessed and analyzed, the second test case is investigated to study the complete ignition transient of a lean hydrogen flame. The test rig investigated operates under ambient conditions in terms of pressure and temperature. Firstly, the validation of the cold flow field is conducted

using pure air. In this context, several sensitivities are performed to identify optimal elements grid size and computational domain strategy as a compromise between the accuracy of the results and the computational effort. When the spark is released, the ignition process is analyzed until the flame stabilization on the bluff body. The ignition sequence is accurately predicted in terms of timing and flame evolution as confirmed by the comparison with experimental data averaged over several tests, underlining the reliability of the numerical simulations. Although the dynamics of ignition and flame development do not show significant differences between the simulations, this allows to conclude some points. The inclusion of the Soret effect, which also causes slight de-mixing in the cold field as a result of the bluff body thermostat, has a minor impact on ignition dynamics and global behavior, whereas it plays an important role concerning local flame phenomena and characteristics. However, to correctly capture the dynamic response of the rig in terms of pressure behavior, it is necessary to use a fine grid for the entire length of the combustion chamber.

Then, by introducing a perforated plate at the outlet, a permanent flashback scenario is investigated. The simulation enables the study of the dynamics inside the injector by reconstructing the pressure signal, first identifying a separation at the injector outlet and then the boundary layer flashback that occurs on the inner surface of the channel. Visualization of the dynamics inside the injector, which is often inaccessible experimentally, provides important design inputs.

The presented analysis focuses on the ignition dynamics up to the complete stabilization of the flame on the burner. A numerical methodology is provided to capture the key mechanisms. Further analysis can be conducted to verify if the numerical approach can capture the correct experimentally observed trend for the same exhaust backpressure condition and different operating conditions in terms of equivalence ratio. Finally, it might be of interest to extend the analysis to more representative conditions in terms of the pressure and temperature at which the ignition phase occurs and ultimately investigate the light-round phase on a multisector burner.

List of Figures

List of Tables

Bibliography

[1] Mertens, Mariano, Jöckel, Patrick, Matthes, Sigrun, Nützel, Matthias, Grewe, Volker, and Sausen, Robert. "Covid-19 induced lower-tropospheric ozone changes." *Environmental Research Letters*, 16(6):064005, 2021.

[2] Grewe, Volker, Gangoli Rao, Arvind, Grönstedt, Tomas, Xisto, Carlos, Linke, Florian, Melkert, Joris, Middel, Jan, Ohlenforst, Barbara, Blakey, Simon, Christie, Simon, et al. "Evaluating the climate impact of aviation emission scenarios towards the paris agreement including covid-19 effects." *Nature Communications*, 12(1):1–10, 2021.

[3] Klöwer, Milan, Allen, MR, Lee, DS, Proud, SR, Gallagher, Leo, and Skowron, Agnieszka. "Quantifying aviation's contribution to global warming." *Environmental Research Letters*, 16(10):104027, 2021.

[4] Flightpath, ACARE. "2050-europe's vision for aviation." *Advisory Council for Aeronautics Research in Europe*, 2011.

[5] Nojoumi, H, Dincer, I, and Naterer, GF. "Greenhouse gas emissions assessment of hydrogen and kerosene-fueled aircraft propulsion." *International journal of hydrogen energy*, 34(3):1363–1369, 2009.

[6] Öberg, Simon, Odenberger, Mikael, and Johnsson, Filip. "Exploring the competitiveness of hydrogen-fueled gas turbines in future energy

systems." *International Journal of Hydrogen Energy*, 47(1):624–644, 2022.

[7] Yilmaz, Nadir and Atmanli, Alpaslan. "Sustainable alternative fuels in aviation." *Energy*, 140:1378–1386, 2017.

[8] Vouros, Stavros, Kavvalos, Mavroudis, Sahoo, Smruti, and Kyprianidis, Konstantinos. "Enabling the potential of hybrid electric propulsion through lean-burn-combustion turbofans." *Journal of the Global Power and Propulsion Society*, 5:164–176, 2021.

[9] Li, Jianzhong, Chen, Jian, Yuan, Li, Hu, Ge, and Feng, Jianhan. "Flow characteristics of a rich-quench-lean combustor-combined low-emission and high-temperature rise combustion." *International Journal of Aerospace Engineering*, 2019:1–22, 2019.

[10] Gazzani, Matteo, Chiesa, Paolo, Martelli, Emanuele, Sigali, Stefano, and Brunetti, Iarno. "Using hydrogen as gas turbine fuel: premixed versus diffusive flame combustors." *Journal of engineering for gas turbines and power*, 136(5):051504, 2014.

[11] Reichel, Thoralf G. and Paschereit, Christian Oliver. "Interaction mechanisms of fuel momentum with flashback limits in lean-premixed combustion of hydrogen." *International Journal of Hydrogen Energy*, 42(7):4518–4529, 2017.

[12] McGuirk, JJ. "The aerodynamic challenges of aeroengine gas-turbine combustion systems." *The Aeronautical Journal*, 118(1204): 557–599, 2014.

[13] Hydea project,https://cordis.europa.eu/project/id/101102019, 2023.

[14] Hestia project, https://cordis.europa.eu/project/id/101056865, 2022.

[15] Fflecs project, https://cordis.europa.eu/project/id/101096436, 2023.

[16] Mastorakos, Epaminondas. "Ignition of turbulent non-premixed flames." *Progress in energy and combustion science*, 35(1):57–97, 2009.

[17] Mastorakos, Epaminondas. "Forced ignition of turbulent spray flames." *Proceedings of the Combustion Institute*, 36(2):2367–2383, 2017.

[18] Mastorakos, E, Baritaud, TA, and Poinsot, TJ. "Numerical simulations of autoignition in turbulent mixing flows." *Combustion and Flame*, 109(1-2):198–223, 1997.

[19] Halstead, MP, Kirsch, LJ, and Quinn, CP. "The autoignition of hydrocarbon fuels at high temperatures and pressures—fitting of a mathematical model." *Combustion and flame*, 30:45–60, 1977.

[20] Gutheil, E. "Numerical analysis of the autoignition of methanol, ethanol, n-heptane and n-octane sprays with detailed chemistry." *Combustion science and technology*, 105(4-6):265–278, 1995.

[21] Lefebvre, Arthur H and Ballal, Dilip R. *Gas turbine combustion: alternative fuels and emissions*. CRC press, 2010.

[22] Jones, WP and Navarro-Martinez, S. "Study of hydrogen autoignition in a turbulent air co-flow using a large eddy simulation approach." *Computers & fluids*, 37(7):802–808, 2008.

[23] Collin, F. *Modeling and Large Eddy Simulation of Two-Phase Ignition in Gas Turbines*. Ph.D. Thesis, Université de Toulouse, 2019.

[24] Dale, JD, Smy, PR, and Clements, RM. "Laser ignited internal combustion engine—an experimental study." *SAE Transactions*, pages 1539–1548, 1978.

[25] Maly, Rudolf and Vogel, Manfred. Initiation and propagation of flame fronts in lean ch4-air mixtures by the three modes of the igni-

tion spark. In *Symposium (international) on combustion*, volume 17, pages 821–831. Elsevier, 1979.

[26] Collin-Bastiani, F, Marrero-Santiago, J, Riber, E, Cabot, Gilles, Renou, B, and Cuenot, B. "A joint experimental and numerical study of ignition in a spray burner." *Proceedings of the Combustion Institute*, 37(4):5047–5055, 2019.

[27] Marrero-Santiago, Javier, Collin-Bastiani, Felix, Riber, Eleonore, Cabot, Gilles, Cuenot, Benedicte, and Renou, Bruno. "On the mechanisms of flame kernel extinction or survival during aeronautical ignition sequences: experimental and numerical analysis." *Combustion and Flame*, 222:70–84, 2020.

[28] Jo, Seunghyun and Gore, Jay P. "Laser ignition energy for turbulent premixed hydrogen air jets." *Combustion and Flame*, 236:111767, 2022.

[29] Ahmed, Samer F. "The probabilistic nature of ignition of turbulent highly-strained lean premixed methane-air flames for low-emission engines." *Fuel*, 134:97–106, 2014.

[30] Yahou, T., Dawson, J. R., and Schuller, T. "Impact of chamber back pressure on the ignition dynamics of hydrogen enriched premixed flames." *Proceedings of the Combustion Institute*, 39:4641–4650, 1 2023.

[31] Palanti, L. *On the modelling of liquid fuel ignition and atomization in aero-engine combustors*. Ph.D. Thesis, Università degli Studi di Firenze, 2020.

[32] Sloane, Thompson M and Ronney, Paul D. "A comparison of ignition phenomena modelled with detailed and simplified kinetics." *Combustion science and technology*, 88(1-2):1–13, 1993.

[33] Thiele, Maren, Selle, Stefan, Riedel, Uwe, Warnatz, Jürgen, and Maas, Ulrich. "Numerical simulation of spark ignition including

ionization." *Proceedings of the combustion institute*, 28(1):1177–1185, 2000.

[34] Miki, Kenji, Schulz, Joey, and Menon, Suresh. "Large-eddy simulation of equilibrium plasma-assisted combustion in supersonic flow." *Proceedings Of The Combustion Institute*, 32(2):2413–2420, 2009.

[35] Collin-Bastiani, F, Vermorel, O, Lacour, C, Lecordier, B, and Cuenot, B. "Dns of spark ignition using analytically reduced chemistry including plasma kinetics." *Proc. Combust. Inst.*, 37 (4):5057–5064, 2019.

[36] Lacaze, G., Richardson, E., and Poinsot, T. "Large eddy simulation of spark ignition in a turbulent methane jet." *Combustion and Flame*, 156:1993–2009, 10 2009.

[37] Falkenstein, Tobias, Kang, Seongwon, Cai, Liming, Bode, Mathis, and Pitsch, Heinz. "Dns study of the global heat release rate during early flame kernel development under engine conditions." *Combustion and Flame*, 213:455–466, 2020.

[38] Pouech, Paul, Duchaine, Florent, and Poinsot, Thierry. "Premixed flame ignition in high-speed flows over a backward facing step." *Combustion and Flame*, 229:111398, 2021.

[39] Andreini, A, Amerighi, M, Palanti, L, and Facchini, B. "Large eddy simulation based computational fluid dynamics investigation of the ignition process in lean spray burner." *Journal of Engineering for Gas Turbines and Power*, 144(6):061016, 2022.

[40] Garzon, Ernesto Sandoval, Mehl, Cédric, and Colin, Olivier. "Modeling of spark ignition in gaseous mixtures using adaptive mesh refinement coupled to the thickened flame model." *Combustion and Flame*, 248:112507, 2023.

[41] Böttler, H, Chen, X, Xie, S, Scholtissek, A, Chen, Z, and Hasse, C. "Flamelet modeling of forced ignition and flame propagation in hydrogen-air mixtures." *Combustion and Flame*, 243:112125, 2022.

[42] Ahmed, Samer F, Balachandran, Ramanarayan, Marchione, Teresa, and Mastorakos, Epaminondas. "Spark ignition of turbulent non-premixed bluff-body flames." *Combustion and Flame*, 151(1-2): 366–385, 2007.

[43] Eyssartier, Alexandre, Cuenot, Benedicte, Gicquel, Laurent YM, and Poinsot, Thierry. "Using les to predict ignition sequences and ignition probability of turbulent two-phase flames." *Combustion and Flame*, 160(7):1191–1207, 2013.

[44] Verdier, Antoine, Santiago, Javier Marrero, Vandel, Alexis, Godard, Gilles, Cabot, Gilles, and Renou, Bruno. "Local extinction mechanisms analysis of spray jet flame using high speed diagnostics." *Combustion and Flame*, 193:440–452, 2018.

[45] Klein, M, Chakraborty, N, and Cant, RS. "Effects of turbulence on self-sustained combustion in premixed flame kernels: a direct numerical simulation (dns) study." *Flow, turbulence and combustion*, 81:583–607, 2008.

[46] Wu, Fujia, Saha, Abhishek, Chaudhuri, Swetaprovo, and Law, Chung K. "Facilitated ignition in turbulence through differential diffusion." *Physical review letters*, 113(2):024503, 2014.

[47] Shy, Shenqyang Steven, Nguyen, Minh Tien, Huang, Shih-Yao, and Liu, Chien-Chia. "Is turbulent facilitated ignition through differential diffusion independent of spark gap?" *Combustion and Flame*, 185:1–3, 2017.

[48] Shy, SS, Nguyen, Minh Tien, and Huang, Shih Yao. "Effects of electrode spark gap, differential diffusion, and turbulent dissipation on two distinct phenomena: Turbulent facilitated ignition versus minimum ignition energy transition." *Combustion and Flame*, 205: 371–377, 2019.

[49] Chen, Xinyi, Xie, Shumeng, Böttler, Hannes, Scholtissek, Arne, Han, Wang, Yu, Dehai, Hasse, Christian, and Chen, Zheng. "Effects

of electrodes and imposed flow on forced ignition in laminar premixed hydrogen/air mixtures with large lewis number." *Proceedings of the Combustion Institute*, 39(2):1967–1976, 2023.

[50] Chen, Xinyi, Böttler, Hannes, Xie, Shumeng, Scholtissek, Arne, Han, Wang, Hasse, Christian, and Chen, Zheng. "On the flow-facilitated ignition in a mixture with low lewis number." *Combustion and Flame*, 258:113091, 2023.

[51] Chu, Hongchao, Berger, Lukas, Grenga, Temistocle, Wu, Zhao, and Pitsch, Heinz. "Effects of differential diffusion on hydrogen flame kernel development under engine conditions." *Proc. Combust. Inst.*, 39:2129–2138, 2023.

[52] Liu, Chong, Tang, Kechen, Huang, Chuyuan, Liu, Jiajia, and Liu, Lijuan. "Effect of initial pressure on the critical characteristics and overpressure of hydrogen-air premixed gas combustion and explosion." *International Journal of Hydrogen Energy*, 49:311–322, 2024.

[53] Beita, J., Talibi, M., Sadasivuni, S., and Balachandran, R. "Thermoacoustic instability considerations for high hydrogen combustion in lean premixed gas turbine combustors: A review." *Hydrogen*, 2: 33–57, 1 2021.

[54] Tartsch, Simon, Flebbe, Saskia, Marques de Sousa Ponte, Joao Germano, and Sattelmayer, Thomas. "Effect of Fuel Reactivity and Operating Conditions On Flame Anchoring in the Premixing Zone of a Swirl Stabilized Gas Turbine Combustor." *J. Eng. Gas Turb. Pow.*, 86953:1–24, 2023.

[55] Weinrotter, M., Kopecek, H., Tesch, M., Wintner, E., Lackner, Ma., and Winter, F. "Laser ignition of ultra-lean methane/hydrogen/air mixtures at high temperature and pressure." *Experimental Thermal and Fluid Science*, 29:569–577, 6 2005.

[56] Fritz, Jassin, Kro¨ ner, Martin, and Sattelmayer, Thomas. "Flashback in a swirl burner with cylindrical premixing zone." *J. Eng. Gas Turbines Power*, 126(2):276–283, 2004.

[57] Eichler, Christian and Sattelmayer, Thomas. "Premixed flame flashback in wall boundary layers studied by long-distance micro-piv." *Experiments in fluids*, 52(2):347–360, 2012.

[58] Utschick, M. *Sicherheitskriterien für die vorgemischte Verbrennung wasserstoffhaltige Brennstoffe in Gasturbinen.* Ph.D. Thesis, Technische Universität München, 2016.

[59] Reichel, Thoralf G., Terhaar, Steffen, and Paschereit, Oliver. "Increasing Flashback Resistance in Lean Premixed Swirl-Stabilized Hydrogen Combustion by Axial Air Injection." *Journal of Engineering for Gas Turbines and Power*, 137(7):1–9, 2015.

[60] Duan, Zhixuan, Shaffer, Brendan, McDonell, Vincent, Baumgartner, Georg, and Sattelmayer, Thomas. "Influence of burner material, tip temperature, and geometrical flame configuration on flashback propensity of h2-air jet flames." *Journal of engineering for gas turbines and power*, 136(2):021502, 2014.

[61] Ebi, D, Bombach, R, and Jansohn, P. "Swirl flame boundary layer flashback at elevated pressure: Modes of propagation and effect of hydrogen addition." *Proceedings of the Combustion Institute*, 38(4): 6345–6353, 2021.

[62] Zhang, Shiming, Lu, Zhen, and Yang, Yue. "Modeling the boundary-layer flashback of premixed hydrogen-enriched swirling flames at high pressures." *Combust. Flame*, 255:112900, 2023.

[63] Ranjan, Rakesh and Clemens, Noel T. "Insights into flashback-to-flameholding transition of hydrogen-rich stratified swirl flames." *Proceedings of the Combustion Institute*, 38(4):6289–6297, 2021.

[64] Yahou, Tarik, Schuller, Thierry, and Dawson, James R. The effect of ignition procedure on flashback of hydrogen-enriched flames. In *Turbo Expo: Power for Land, Sea, and Air*, volume 86953, page V03AT04A039. American Society of Mechanical Engineers, 2023.

[65] Marchione, Teresa, Ahmed, Samer F, and Mastorakos, Epaminondas. "Ignition of turbulent swirling n-heptane spray flames using single and multiple sparks." *Combustion and Flame*, 156(1):166–180, 2009.

[66] Boileau, M, Staffelbach, G, Cuenot, B, Poinsot, T, and Berat, C. "LES of an ignition sequence in a gas turbine engine." *Combustion and Flame*, 154(1-2):2–22, 2008.

[67] Lancien, Théa, Prieur, Kevin, Durox, Daniel, Candel, Sébastien, and Vicquelin, Ronan. "Leading point behavior during the ignition of an annular combustor with liquid n-heptane injectors." *Proceedings of the Combustion Institute*, 37(4):5021–5029, 2019.

[68] Marrero-Santiago, Javier, Verdier, Antoine, Vandel, Alexis, Cabot, Gilles, Boukhalfa, Abdelkrim Mourad, and Renou, Bruno. "Effect of injector spacing in the light-around ignition efficiency and mechanisms in a linear swirled spray burner." *Heat and Mass Transfer*, 55:1871–1885, 2019.

[69] Prieur, Kevin, Durox, Daniel, Beaunier, Jerome, Schuller, Thierry, and Candel, Sebastien. "Ignition dynamics in an annular combustor for liquid spray and premixed gaseous injection." *Proceedings of the Combustion Institute*, 36(3):3717–3724, 2017.

[70] Prieur, Kevin, Vignat, Guillaume, Durox, Daniel, Schuller, Thierry, and Candel, Sébastien. "Flame and spray dynamics during the light-round process in an annular system equipped with multiple swirl spray injectors." *Journal of Engineering for Gas Turbines and Power*, 141(6):061007, 2019.

[71] Zhao, Dongmei, Xia, Yifan, Ge, Haiwen, Lin, Qizhao, and Wang, Gaofeng. "Large eddy simulation of flame propagation dur-

ing the ignition process in an annular multiple-injector combustor." *Fuel*, 263:116402, 2020.

[72] Philip, M, Boileau, M, Vicquelin, R, Riber, E, Schmitt, T, Cuenot, B, Durox, D, and Candel, S. "Large eddy simulations of the ignition sequence of an annular multiple-injector combustor." *Proceedings of the Combustion Institute*, 35(3):3159–3166, 2015.

[73] Lancien, Théa, Prieur, Kevin, Durox, Daniel, Candel, Sébastien, and Vicquelin, Ronan. "Large Eddy Simulation of Light-Round in an Annular Combustor With Liquid Spray Injection and Comparison With Experiments." *Journal of Engineering for Gas Turbines and Power*, 140(2), 2018.

[74] Töpperwien, Karl, Collin-Bastiani, Félix, Riber, Eleonore, Cuenot, Bénédicte, Vignat, Guillaume, Prieur, Kevin, Durox, Daniel, Candel, Sébastien, and Vicquelin, Ronan. "Large-eddy simulation of flame dynamics during the ignition of a swirling injector unit and comparison with experiments." *Journal of Engineering for Gas Turbines and Power*, 143(2):021015, 2021.

[75] ANSYS. *Fluent 22.1 Theory Guide*, 2022.

[76] Hilbert, R., Tap, F., El-Rabii, H., and Thévenin, D. "Impact of detailed chemistry and transport models on turbulent combustion simulations." *Progress in Energy and Combustion Science*, 30:61–117, 2004.

[77] Yang, F., Law, C. K., Sung, C. J., and Zhang, H. Q. "A mechanistic study of soret diffusion in hydrogen-air flames." *Combustion and Flame*, 157:192–200, 1 2010.

[78] Poinsot, T. and Veynante, D. *Theoretical and numerical combustion.* RT Edwards, Inc., 2005.

[79] Swart, J. A. M. De, Bastiaans, R. J. M., Oijen, J. A. Van, Goey, L. P. H. De, and Cant, R. S. "Inclusion of preferential diffusion in simulations of premixed combustion of hydrogen/methane mixtures with

flamelet generated manifolds." *Flow, Turbulence and Combustion*, 85:473–511, 12 2010.

[80] Dinesh, K. K. J. Ranga, Shalaby, H., Luo, K. H., van Oijen, J. A., and Thévenin, D. "High hydrogen content syngas fuel burning in lean premixed spherical flames at elevated pressures: Effects of preferential diffusion." *International Journal of Hydrogen Energy*, 41:18231–18249, 10 2016.

[81] Van Oijen, J. A., Donini, A., Bastiaans, R. J.M., ten Thije Boonkkamp, J. H.M., and de Goey, L. P.H. "State-of-the-art in premixed combustion modeling using flamelet generated manifolds." *Progress in Energy and Combustion Science*, 57(2016):30–74, 2016.

[82] Capurso, T., Laera, D., Riber, E., and Cuenot, B. "NOx pathways in lean partially premixed swirling H2-air turbulent flame." *Combustion and Flame*, 248(x):112581, 2023.

[83] Smagorinsky, Joseph. "General circulation experiments with the primitive equations: I. the basic experiment." *Monthly weather review*, 91(3):99–164, 1963.

[84] Nicoud, Franck and Ducros, Frédéric. "Subgrid-scale stress modelling based on the square of the velocity gradient tensor." *Flow, turbulence and Combustion*, 62(3):183–200, 1999.

[85] Nicoud, Franck, Toda, Hubert Baya, Cabrit, Olivier, Bose, Sanjeeb, and Lee, Jungil. "Using singular values to build a subgrid-scale model for large eddy simulations." *Physics of fluids*, 23(8), 2011.

[86] da Silva, C. B. and Pereira, J. C.F. "On the local equilibrium of the subgrid scales: The velocity and scalar fields." *Physics of Fluids*, 17, 2005.

[87] Orszag, S. and Yakhot, V. "Renormalization group analysis of turbulence." *Journal of Scientific Computing*, 1, 1986.

[88] Germano, M., Piomelli, U., and et al. "A dynamic subgrid-scale eddy viscosity model." *American Institute of Physics*, pages 1760–1764, 1991.

[89] Lilly, Douglas K. "A proposed modification of the germano subgrid-scale closure method." *Physics of Fluids A: Fluid Dynamics*, 4(3): 633–635, 1992.

[90] Peters, Norbert. "Turbulent combustion." *Measurement Science and Technology*, 12(11):2022–2022, 2001.

[91] Colin, O, Ducros, Frédéric, Veynante, D, and Poinsot, Thierry. "A thickened flame model for large eddy simulations of turbulent premixed combustion." *Physics of fluids*, 12(7):1843–1863, 2000.

[92] Legier, Jean-Philippe, Poinsot, Thierry, and Veynante, Denis. Dynamically thickened flame les model for premixed and non-premixed turbulent combustion. In *Proceedings of the summer program*, volume 12, pages 157–168. Citeseer, 2000.

[93] Williams, F.A. *Combustion Theory: The Fundamental Theory of Chemically Reacting Flow Systems*. Addison-Wesley series in engineering science. Addison-Wesley Publishing Company, 1965.

[94] Durand, L. and Polifke, W. "Implementation of the thickened flame model for large eddy simulation of turbulent premixed combustion in a commercial solver." *ASME Turbo Expo*, 2007.

[95] Van Oijen, J A and De Goey, L P H. "Combustion Science and Technology Modelling of Premixed Laminar Flames using Flamelet-Generated Manifolds." *Combustion Science and Technology*, 161(1): 113–137, 2000.

[96] Andreini, A, Bertini, D, Facchini, B, and Puggelli, S. "Large-eddy simulation of a turbulent spray flame using the flamelet generated manifold approach." *Energy Procedia*, 82:395–401, 2015.

[97] Paccati, Simone, Bertini, Davide, Mazzei, Lorenzo, Puggelli, Stefano, and Andreini, Antonio. "Large-eddy simulation of a model aero-engine sooting flame with a multiphysics approach." *Flow, Turbulence and Combustion*, 106:1329–1354, 2021.

[98] Bilger, RW. "The structure of turbulent nonpremixed flames." *Symposium (International) on Combustion*, 22(1):475–488, 1989.

[99] Peters, Norbert. "Turbulent combustion." *Measurement Science and Technology*, 12(11):2022–2022, 2001.

[100] Pitsch, H and Peters, N. "A consistent flamelet formulation for non-premixed combustion considering differential diffusion effects." *Combustion and flame*, 114(1-2):26–40, 1998.

[101] Ramaekers, WJS, Albrecht, BA, Van Oijen, JA, De Goey, LPH, and Eggels, RGLM. "The application of flamelet generated manifolds in modelling of turbulent partially-premixed flames." *RGLM Eggels*, 2005.

[102] Donini, A., Bastiaans, R.J.M., van Oijen, J.A., and de Goey, L.P.H. "Differential diffusion effects inclusion with flamelet generated manifold for the modeling of stratified premixed cooled flames." *Proceedings of the Combustion Institute*, 35(1):831–837, 2015.

[103] Mukundakumar, Nithin, Efimov, Denis, Beishuizen, Nijso, and van Oijen, Jeroen. "A new preferential diffusion model applied to FGM simulations of hydrogen flames." *Combustion Theory and Modelling*, 25(7):1245–1267, 2021.

[104] Kai, Reo, Tokuoka, Taiki, Nagao, Jun, Pillai, Abhishek Lakshman, and Kurose, Ryoichi. "Les flamelet modeling of hydrogen combustion considering preferential diffusion effect." *International Journal of Hydrogen Energy*, 48(29):11086–11101, 2023.

[105] Kutkan, Halit, Amato, Alberto, Campa, Giovanni, Ghirardo, Giulio, Tay Wo Chong, Luis, and Æsøy, Eirik. "Modelling of turbulent

premixed ch4/h2/air flames including the influence of stretch and heat losses." *American Society of Mechanical Engineers*, 84942: V03AT04A034, 2021.

[106] Kutkan, Halit, Amato, Alberto, Campa, Giovanni, Tay-Wo-Chong, Luis, and Æsøy, Eirik. "Les of turbulent premixed ch4/h2/air flames with stretch and heat loss for flame characteristics and dynamics." *American Society of Mechanical Engineers*, 86007: V03BT04A021, 2022.

[107] Zimont, V., Polifke, W., Bettelini, M., and Weisenstein, W. "An Efficient Computational Model for Premixed Turbulent Combustion at High Reynolds Numbers Based on a Turbulent Flame Speed Closure." *Journal of Engineering for Gas Turbines and Power*, 120 (3):526–532, 1998.

[108] Klarmann, Noah, Sattelmayer, Thomas, Geng, Weiqun, and Magni, Fulvio. "Flamelet Generated Manifolds for Partially Premixed, Highly Stretched and Non-Adiabatic Combustion in Gas Turbines." *54th AIAA Aerospace Sciences Meeting*, 0(January), 2016.

[109] Langone, Leonardo, Sedlmaier, Julia, Nassini, Pier Carlo, Mazzei, Lorenzo, Harth, Stefan, and Andreini, Antonio. "Numerical modeling of gaseous partially premixed low-swirl lifted flame at elevated pressure." *Proceedings of the ASME Turbo Expo*, 4B-2020: 1–14, 2020.

[110] Tay-Wo-Chong, Luis, Zellhuber, Mathieu, Komarek, Thomas, Im, Hong G, and Polifke, Wolfgang. "Combined influence of strain and heat loss on turbulent premixed flame stabilization." *Flow, Turbulence and Combustion*, 97:263–294, 2016.

[111] Nassini, Pier Carlo, Pampaloni, Daniele, Meloni, Roberto, and Andreini, Antonio. "Lean blow-out prediction in an industrial gas

turbine combustor through a LES-based CFD analysis." *Combustion and Flame*, 229:111391, 2021.

[112] Goodwin, David G, Moffat, Harry K, and Speth, Raymond L. "Cantera: An object-oriented software toolkit for chemical kinetics, thermodynamics, and transport processes." *Caltech, Pasadena, CA*, 124, 2009.

[113] Varga, Tamás, Nagy, Tibor, Olm, C, Zsély, I Gy, Pálvölgyi, R, Valkó, É, Vincze, G, Cserháti, M, Curran, Henry J, and Turányi, T. "Optimization of a hydrogen combustion mechanism using both direct and indirect measurements." *Proceedings of the Combustion Institute*, 35(1):589–596, 2015.

[114] Barre, David. *Simulation Numerique De L'Allumage Dans Les Chambres De Combustion Aeronautiques*. Phd thesis, Université de Toulouse, 2014.

[115] Vogel, M. and Maly, R. "Initiation and propagation of flame fronts in lean ch4-air mixtures by the three modes of the ignition spark." *Proc. of the 17th Symp. (Int.) on Combustion, The Combustion Institute*, pages 821–831, 1978.

[116] Barré, David, Esclapez, Lucas, Cordier, Matthieu, Riber, Eleonore, Cuenot, Bénédicte, Staffelbach, Gabriel, Renou, Bruno, Vandel, Alexis, Gicquel, Laurent Y.M., and Cabot, Gilles. "Flame propagation in aeronautical swirled multi-burners: Experimental and numerical investigation." *Combustion and Flame*, 161(9):2387–2405, sep 2014.

[117] Boivin, Pierre, Jiménez, Carmen, Sánchez, Antonio L, and Williams, Forman A. "An explicit reduced mechanism for h2–air combustion." *Proceedings of the Combustion Institute*, 33(1): 517–523, 2011.

[118] Kéromnès, Alan, Metcalfe, Wayne K, Heufer, Karl A, Donohoe, Nicola, Das, Apurba K, Sung, Chih-Jen, Herzler, Jürgen,

Naumann, Clemens, Griebel, Peter, Mathieu, Olivier, et al. "An experimental and detailed chemical kinetic modeling study of hydrogen and syngas mixture oxidation at elevated pressures." *Combustion and Flame*, 160(6):995–1011, 2013.

[119] Sánchez, Antonio L. and Williams, Forman A. "Recent advances in understanding of flammability characteristics of hydrogen." *Progress in Energy and Combustion Science*, 41(1):1–55, 2014.

[120] Egolfopoulos, F. N. and Law, C. K. "An experimental and computational study of the burning rates of ultra-lean to moderately-rich h2/o2/n2 laminar flames with pressure variations." *The Combustion Istitute*, pages 333–340, 1990.

[121] Kwon, O. C. and Faeth, G. M. "Flame/stretch interactions of premixed hydrogen-fueled flames: Measurements and predictions." *Combustion and Flame*, 124:590–610, 2001.

[122] Zhukov, Victor P. "Verification, validation, and testing of kinetic mechanisms of hydrogen combustion in fluid-dynamic computations." *ISRN Mechanical Engineering*, 2012:1–11, 8 2012.

[123] Schultz, E and Shepherd, J. "Validation of detailed reaction mechanisms for detonation simulation." 2000.

[124] Herzler, J. and Naumann, C. "Shock tube study of the ignition of lean co/h2 fuel blends at intermediate temperatures and high pressure." *Combustion Science and Technology*, 180:2015–2028, 2008.

[125] Herzler, Jürgen and Naumann, Clemens. "Shock-tube study of the ignition of methane/ethane/hydrogen mixtures with hydrogen contents from 0% to 100% at different pressures." *Proceedings of the combustion institute*, 32(1):213–220, 2009.

[126] Cirrone, D., Makarov, D., Proust, C., and Molkov, V. "Minimum ignition energy of hydrogen-air mixtures at ambient and cryogenic

temperatures." *International Journal of Hydrogen Energy*, 48:16530–16544, 2023.

[127] Ono, R., Nifuku, M., Fujiwara, S., Horiguchi, S., and Oda, T. "Minimum ignition energy of hydrogen-air mixture: Effects of humidity and spark duration." *Journal of Electrostatics*, 65:87–93, 2007.

[128] Matalon, M., Cui, C., and Bechtold, J. K. "Hydrodynamic theory of premixed flames: Effects of stoichiometry, variable transport coefficients and arbitrary reaction orders." *Journal of Fluid Mechanics*, 487:179–210, 7 2003.

[129] Giannakopoulos, G. K., Matalon, M., Frouzakis, C. E., and Tomboulides, A. G. "The curvature markstein length and the definition of flame displacement speed for stationary spherical flames." *Proceedings of the Combustion Institute*, 35:737–743, 2015.

[130] Yokomori, Takeshi, Chen, Zheng, and Ju, Yiguang. Studies on the flame curvature effect on burning velocity. In *44th AIAA Aerospace Sciences Meeting and Exhibit*, page 161, 2006.

[131] Berger, Lukas, Attili, Antonio, and Pitsch, Heinz. "Intrinsic instabilities in premixed hydrogen flames: Parametric variation of pressure, equivalence ratio, and temperature. part 1-dispersion relations in the linear regime." *Combustion and Flame*, 240:111935, 2022.

[132] Berger, Lukas, Attili, Antonio, and Pitsch, Heinz. "Intrinsic instabilities in premixed hydrogen flames: parametric variation of pressure, equivalence ratio, and temperature. part 2–non-linear regime and flame speed enhancement." *Combustion and Flame*, 240:111936, 2022.

[133] Beeckmann, Joachim, Hesse, Raik, Kruse, Stephan, Berens, André, Peters, Norbert, Pitsch, Heinz, and Matalon, Moshe. "Propagation speed and stability of spherically expanding hydrogen/air flames: Experimental study and asymptotics." *Proceedings of the Combustion Institute*, 36:1531–1538, 2017.

[134] Mira, D., Lehmkuhl, O., Stathopoulos, P., Tanneberger, T., Reichel, T. G., Paschereit, C. O., Vázquez, M., and Houzeaux, G. Numerical Investigation of a Lean Premixed Swirl-Stabilized Hydrogen Combustor and Operational Conditions Close to Flashback. In *Volume 4B: Combustion, Fuels, and Emissions*, pages 1–13. American Society of Mechanical Engineers, 2018.

[135] Mira, D., Lehmkuhl, O., Both, A., Stathopoulos, P., Tanneberger, T., Reichel, T. G., Paschereit, C. O., Vázquez, M., and Houzeaux, G. "Numerical Characterization of a Premixed Hydrogen Flame Under Conditions Close to Flashback." *Flow, Turbulence and Combustion*, 104(2-3):479–507, 2020.

[136] Reichel, Thoralf G., Goeckeler, Katharina, and Paschereit, Oliver. "Investigation of lean premixed swirl-stabilized hydrogen burner with axial air injection using OH-PLIF imaging." *Journal of Engineering for Gas Turbines and Power*, 137(11):1–10, 2015.

[137] Boivin, Pierre, Sánchez, Antonio L, and Williams, Forman A. "Four-step and three-step systematically reduced chemistry for wide-range H2–air combustion problems." *Combustion and Flame*, 160(1): 76–82, 2013.

[138] ANSYS. *Fluent 19.3 Theory Guide*, 2020.

[139] Rochette, Bastien, Collin-Bastiani, Félix, Gicquel, Laurent, Vermorel, Olivier, Veynante, Denis, and Poinsot, Thierry. "Influence of chemical schemes, numerical method and dynamic turbulent combustion modeling on les of premixed turbulent flames." *Combustion and Flame*, 191:417–430, 2018.

[140] Celik, I. B., Cehreli, Z. N., and Yavuz, I. "Index of Resolution Quality for Large Eddy Simulations." *Journal of Fluids Engineering*, 127(5):949–958, sep 2005.

[141] Yamashita, H, Shimada, M, and Takeno, T. A numerical study on flame stability at the transition point of jet diffusion flames. In

Symposium (international) on combustion, volume 26, pages 27–34. Elsevier, 1996.

[142] Castellani, Simone, Meloni, Roberto, Orsino, Stefano, Ansari, Naseem, Yadav, Rakesh, Bessette, Didier, Boxx, Isaac, and Andreini, Antonio. "High-fidelity h2–ch4 jet in crossflow modelling with a flame index-controlled artificially thickened flame model." *International Journal of Hydrogen Energy*, 2023.

[143] Aniello, Andrea, Laera, Davide, Marragou, Sylvain, Magnes, Hervé, Selle, Laurent, Schuller, Thierry, and Poinsot, Thierry. "Experimental and numerical investigation of two flame stabilization regimes observed in a dual swirl h2-air coaxial injector." *Combustion and Flame*, 249:112595, 2023.

[144] Gicquel, Olivier, Hilbert, Renan, Thévenin, Dominique, and Darabiha, Nasser. Influence of differential diffusion on local equilibrium and super-equilibrium combustion in turbulent non-premixed flames. In *IUTAM Symposium on Turbulent Mixing and Combustion: Proceedings of the IUTAM Symposium held in Kingston, Ontario, Canada, 3–6 June 2001*, pages 149–159. Springer, 2002.

[145] Senatori, G. *Large Eddy Simulation of the ignition process of a lean premixed hydrogen-air flame.* Master thesis, Università degli Studi di Firenze, 2023.

[146] Jones, W. P. and Tyliszczak, A. "Large eddy simulation of spark ignition in a gas turbine combustor." *Flow, Turbulence and Combustion*, 85:711–734, 12 2010.

[147] Yahou, T., Schuller, T., and Dawson, J. R. "Analysis of the ignition dynamics of h2-enriched premixed flames using high speed piv/ohplif." *Proceedings of the European Combustion Meeting*, 2023.